Final Report Submitted to
The California Department of Transportation
Under Contract No. 59A0689

Utilization of Strong Motion Data for Toll Bridge Damage Assessment

By

Maria Q. Feng, Professor

Reza Baghaei, Post-doctoral Researcher

and

Andrea Zampieri, Graduate Student Researcher

Civil and Environmental Engineering Department
University of California, Irvine

October 2011

STATE OF CALIFORNIA DEPARTMENT OF TRANSPORTATION

TECHNICAL REPORT DOCUMENTATION PAGE

TR0003 (REV. 10/98)

1. REPORT NUMBER	2. GOVERNMENT ASSOCIATION NUMBER	3. RECIPIENT'S CATALOG NUMBER
CA11-2253		

Utilization of Strong Motion Data for Toll Bridge Damage Assessment	5. REPORT DATE October 2011
	6. PERFORMING ORGANIZATION CODE UC Irvine
7. AUTHOR(S) Maria Q. Feng, Reza Baghaei, and Andrea Zampieri	8. PERFORMING ORGANIZATION REPORT NO. UCI-CEEMF006
9. PERFORMING ORGANIZATION NAME AND ADDRESS Civil and Environmental Engineering E4120 Engineering Gateway University of California, Irvine Irvine, CA 92696-2175	10. WORK UNIT NUMBER
	11. CONTRACT OR GRANT NUMBER 59A0689
12. SPONSORING AGENCY AND ADDRESS California Department of Transportation Engineering Service Center 1801 30th Street, M.S. 9-2/5i Sacramento CA 95816 California Department of Transportation Division of Research and Innovation, MS-83 1227 O Street Sacramento CA 95814	13. TYPE OF REPORT AND PERIOD COVERED Final Report 5/1/2009 – 10/31/2011
	14. SPONSORING AGENCY CODE 913

15. SUPPLEMENTAL NOTES

16. ABSTRACT

Post-event damage assessment in structures typically requires a detailed and time-consuming visual inspection and evaluation. This project explores the utilization of the strong motion data for automated, remote, real-time damage assessment of bridges immediately after a destructive event. Various vibration-based damage assessment methods are investigated for post-event damage assessment from noisy and incomplete measurements. Output-only and input-output system identification techniques are respectively applied for identification of modal properties of the bridge from ambient vibrations and responses to high amplitude earthquake excitations. An optimization-based finite element model updating methodology is applied for identification of damage characteristics by monitoring the variations in stiffness properties of critical elements of the bridge. A hybrid optimization procedure based on genetic algorithm and quasi-Newton optimization techniques is implemented to identify the best set of FE model parameters that minimizes the objective functions. Two objective functions are defined expressing the discrepancy between the measured and analytical response characteristics in time and modal domains. The meaningful agreement between analytical and experimental FE model parameters demonstrates the efficacy of the proposed damage identification procedure. Furthermore, two vibration-based procedures are proposed for investigation of the consequences of damage in collapse capacity and functionality status of the bridge. The first procedure applies a double-integration and filtering routine to estimate the maximum drift ratios experienced by the lateral force resisting elements of the bridge from acceleration measurements. The estimated drift ratios along with pushover curves of the corresponding elements are used to calculate the ductility-based residual capacity of the elements and the bridge. The second procedure utilizes the incremental dynamic analysis curves for estimating the collapse capacity of the bridge. A new approach is proposed for generating FE model realizations of the seismically damaged structures, which are used to estimate the ultimate capacity of the structure. The amount of loss in capacity along with seismic hazard characteristics at the bridge site and a set of tagging criteria are proposed for tagging and assessing the functionality status of the damaged bridge. The proposed damage assessment and residual capacity estimation methods are evaluated and validated by the results of seismic shake table experiments on a large-scale reinforced concrete bridge model.

17. KEY WORDS	18. DISTRIBUTION STATEMENT	
	No restrictions. This document is available to the public through the National Technical Information Service, Springfield, VA 22161	
19. SECURITY CLASSIFICATION (of this report)	20. NUMBER OF PAGES	21. PRICE
Unclassified	159	

Reproduction of completed page authorized

DISCLAIMER STATEMENT

This document is disseminated in the interest of information exchange. The contents of this report reflect the views of the authors who are responsible for the facts and accuracy of the data presented herein. The contents do not necessarily reflect the official views or policies of the State of California or the Federal Highway Administration. This publication does not constitute a standard, specification or regulation. This report does not constitute an endorsement by the Department of any product described herein.

For individuals with sensory disabilities, this document is available in Braille, large print, audiocassette, or compact disk. To obtain a copy of this document in one of these alternate formats, please contact: the Division of Research and Innovation, MS-83, California Department of Transportation, P.O. Box 942873, Sacramento, CA 94273-0001.

SUMMARY

Post-event damage assessment in structures typically requires a detailed and time-consuming visual inspection and evaluation. Lack of information about damage in highway bridges, particularly the important toll bridges, can cause safety hazards, halt mobility of the tranportation network and disrupt emergency response. On the other hand, Caltrans, with the assistance of the California Geological Survey (CGS), has instrumented 68 bridge structures throught California with strong motion sensors for the purposese of advancing understanding of how bridge structures react to seismic imput and validating dynamic modeling techniques.

This project explores the usage of the strong motion data for automated, remote, real-time damage assessment of bridges immediatly after a destructive event. Various vibration-based damage assessment methods are investigated for post-event damage assessment from noisy and incomplete measurements. The first part of this report is devoted to experimental modal analysis. Output-only and input-output system identification techniques are respectively applied for identification of modal properties of the bridge from the measured ambient vibration data and responses to earthquake excitations. The second part of the report deals with identification of structural damage characteristics in critical structural elements using an optimization-based finite element (FE) model updating methodology. A hybrid optimization procedure based on Genetic Algorithm (GA) and quasi-Newton optimization techniques is implemented for finding the best set of FE model parameters that minimizes the objective functions. Two objective functions are defined expressing the discrepancy between the measured and analytical response characteristics in time and modal domains. The meaningful agreement between the analytical and experimental

demonstrates the efficiency and accuracy of the proposed damage identification procedure. In the final part of the report, two vibration-based procedures are presented and applied for investigation of the consequences of damage in collapse capacity and functionality status of a damaged bridge. The first procedure applies the double-integration and filtering routine to estimate the maximum drift ratios experienced by the lateral force resisting elements of the bridge from acceleration measurements. The estimated drift ratios along with pushover curves of the corresponding elements are used to calculate the ductility-based residual capacity of the elements and the bridge. The second procedure utilizes the incremental dynamic analysis (IDA) curves for estimation of collapse capacity of the bridge. A new approach for generation of FE model realizations of the seismically damaged structures is proposed and applied. Generated FE realizations of the damaged bridge are employed to estimate the collapse capacity of the structure. The amount of loss in the ultimate capacity of the bridge, along with seismic hazard characteristics at the bridge site and a set of tagging criteria, are proposed for tagging and assessing the functionality status of the damaged bridge. The proposed damage assessment and residual capacity estimation methods are evaluated and verified by the results of seismic shake table tests of a large-scale concrete bridge model.

TABLE OF CONTENTS

SUMMARY ..... **II**

LIST OF FIGURES ..... **VI**

LIST OF TABLES ..... **IX**

1 INTRODUCTION **1**

1.1 Literature Review 2

1.2 Scope of the Report and Organization of Material 9

2 EXPERIMENTAL SETUP, TEST SPECIMEN AND INSTRUMENTATION **11**

2.1 Background 11

2.2 Bridge Specimen 12

2.3 Instrumentation and Sensor Layout 14

2.4 Test Procedure 15

2.5 Material Properties 18

2.6 Observed Shake Table Experiment Results 19

3 STRUCTURAL HEALTH MONITORING THROUGH EXPERIMENTAL MODAL ANALYSIS **22**

3.1 Background 22

3.2 Modal Identification from White Noise Excitations 23

3.2.1 Frequency Domain Decomposition Technique 24

3.2.2 Application of FDD Technique to Bridge Response Measurements 27

3.3 Modal Identification From High-Amplitude Earthquake Excitations 33

3.3.1 System Identification Approach 33

3.3.1.1 State Space Model Parameters Estimation Methods 34

3.3.1.3 Extraction of Modal Data from System Matrices 47

3.3.2 Modal Identification Methodology 48

3.3.2.1 Step-1: Time-Frequency Analysis 48

3.3.2.2 Step-2: Identification of Stable Segment of Response 50

3.3.2.3 Step-3: Modal Identification from Stable Segments 58

3.4 Summary of Modal Identification Results 71

4 DAMAGE ASSESSMENT THROUGH FINITE ELEMENT MODEL UPDATING 78
4.1 Background 78
4.2 Genetic Algorithm (GA) 79
4.2.1 Selection 80
4.2.2 Crossover 81
4.2.3 Mutation 81
4.2.4 Elitism 82
4.3 Formulation of Objective Functions 82
4.4 Finite Element Model Updating Results 86
4.4.1 FE Model and Calibration 86
4.4.2 Damage Assessment Results 88
4.4.3 Validation of the Results 93
5 RESIDUAL COLLAPSE CAPACITY ESTIMATION 101
5.1 Background 101
5.2 Ductility-based Residual Capacity Estimation Using Acceleration Data 102
5.2.1 Pushover Analysis of Bents of the Bridge Specimen 102
5.2.2 From Measured Accelerations to Structural Drifts 104
5.2.3 Ductility-based Residual Capacity of the Specimen 107
5.2.4 Summarization of the Results 111
5.2.5 Application to a Toll Bridge Road 111
5.3 Residual Capacity Estimation Using Incremental Dynamic Analysis 118
5.3.1 Step-1: Incremental Dynamic Analysis of the Intact Structure 122
5.3.2 Step-2: Experimental Modal Analysis of Damaged Structure 123
5.3.3 Step-3: Generation of FE Realizations of Damaged Bridge 124
5.3.4 Step-4: Incremental Dynamic Analysis of the Damaged Bridge 128
5.3.5 Step-5: Functionality Status of the Damaged Bridge 133
5.3.6 Summary of the Methodology 134
6 CONCLUSIONS 136
6.1 Experimental Modal Analysis 138
6.2 FE Model Updating 140
6.3 Residual Capacity Estimation 141
7 REFERENCES 143

LIST OF FIGURES

Figure 2–1 Example of prototype location in a multi-span bridge 13
Figure 2–2 Schematic views of the bridge specimen 14
Figure 2–3 Sensor layout of the superstructure of the bridge specimen 15
Figure 2–4 Short-time Fourier transform of (a) earthquake and (b) white noise excitations 16
Figure 2–5 Spectral acceleration curves corresponding to input earthquake excitations 17
Figure 2–6 Damage progression @ Bent-3 (Top of west column) 20
Figure 2–7 Damage progression @ Bent-3 (Bottom of west column) 21
Figure 3–1 Modal identification procedure using FDD technique 27
Figure 3–2 Modal identification using FDD technique (W.N.1) 28
Figure 3–3 Modal identification using FDD technique (W.N.2) 29
Figure 3–4 Modal identification using FDD technique (W.N.3) 30
Figure 3–5 Modal identification using FDD technique (W.N.4) 31
Figure 3–6 Modal identification using FDD technique (W.N.5) 32
Figure 3–7 Modal identification methodology 49
Figure 3–8 Time-dependent modal properties (WN-1) 51
Figure 3–9 Time-dependent modal properties (Test-12) 52
Figure 3–10 Time-dependent modal properties (Test-13) 52
Figure 3–11 Time-dependent modal properties (Test-14) 53
Figure 3–12 Time-dependent modal properties (Test-15) 53
Figure 3–13 Time-dependent modal properties (Test-16) 54
Figure 3–14 Time-dependent modal properties (Test-17) 54
Figure 3–15 Time-dependent modal properties (WN-3) 55
Figure 3–16 Time-dependent modal properties (Test-18) 55
Figure 3–17 Time-dependent modal properties (WN-4) 56
Figure 3–18 Time-dependent modal properties (Test-19) 56
Figure 3–19 Time-dependent modal properties (WN-5) 57
Figure 3–20 Stabilization diagram (a) W.N.1 (b) Test-12 60
Figure 3–21 Stabilization diagram (a) Test-13 (b) Test-14 60
Figure 3–22 Stabilization diagram (a) W.N.2 (b) Test-15 60
Figure 3–23 Stabilization diagram (a) Test-16 (b) Test-17 61
Figure 3–24 Stabilization diagram (a) W.N.3 (b) Test-18 61
Figure 3–25 Stabilization diagram (a) W.N.4 (b) Test-19 61
Figure 3–26 Stabilization diagram (WN-5) 62
Figure 3–27 Acceleration measurements and simulation results (WN-1) 63

Figure 3–28 Acceleration measurements and simulation results (Test-12) 63
Figure 3–29 Acceleration measurements and simulation results (Test-13) 63
Figure 3–30 Acceleration measurements and simulation results (Test-14) 64
Figure 3–31 Acceleration measurements and simulation results (WN-2) 64
Figure 3–32 Acceleration measurements and simulation results (Test-15) 64
Figure 3–33 Acceleration measurements and simulation results (Test-16) 65
Figure 3–34 Acceleration measurements and simulation results (Test-17) 65
Figure 3–35 Acceleration measurements and simulation results (WN-3) 65
Figure 3–36 Acceleration measurements and simulation results (Test-18) 66
Figure 3–37 Acceleration measurements and simulation results (WN-4) 66
Figure 3–38 Acceleration measurements and simulation results (Test-19) 66
Figure 3–39 Acceleration measurements and simulation results (WN-5) 67
Figure 3–40 Time-dependent first mode frequency: (a) 300-point (b) 600-point window 72
Figure 3–41 Time-dependent second mode frequency: (a) 300-point (b) 600-point window 73
Figure 3–42 Time-dependent third mode frequency: (a) 300-point (b) 600-point window 73
Figure 3–43 Fitness distribution for earthquake responses (a) 300-point (b) 600-point window 74
Figure 3–44 Fitness distribution for white noise responses (a) 300-point (b) 600-point window 75
Figure 3–45(a, c, e) Comparison of natural frequencies identified from stable segments of the response (b, d, f) MAC values between mode shapes identified from two approaches 76
Figure 3–46 Fitness of state-space models identified from stable segments of the response 77
Figure 4–1 Flow chart of implemented optimization strategy 79
Figure 4–2 Analytical and experimental modal shapes of the bridge specimen (W.N.1) 87
Figure 4–3 Analytical and measured response histories on the superstructure of bridge (W.N.1) 87
Figure 4–4 Analytical and measured response histories on the superstructure of bridge (W.N.2) 90
Figure 4–5 Analytical and measured response histories on the superstructure of bridge (W.N.3) 91
Figure 4–6 Analytical and measured response histories on the superstructure of bridge (W.N.4) 91
Figure 4–7 Analytical and measured response histories on the superstructure of bridge (W.N.5) 92
Figure 4–8 Estimated average SNRs for measured signals during white noise excitations 93
Figure 4–9 Acceleration-drift relationships of the bents of the intact bridge specimen (W.N.1) 94
Figure 4–10 Acceleration-drift relationships for Bent-1 95
Figure 4–11 Acceleration-drift relationships for Bent-2 96
Figure 4–12 Acceleration-drift relationships for Bent-3 97
Figure 4–13 Stiffness correction factors (Bent-1) 98
Figure 4–14 Stiffness correction factors (Bent-2) 99
Figure 4–15 Stiffness correction factors (Bent-3) 99
Figure 4–16 Stiffness correction factors (Deck) 100
Figure 5–1 Flowchart of ductility-based residual capacity estimation method 102

Figure 5–2 Stress-strain relationship models for (a) concrete02 (b) reinforcing steel 103
Figure 5–3 Pushover curves of the bents 103
Figure 5–4 Frequency response of designed digital filter 104
Figure 5–5 Comparison of double integration results with displacement measurements (Test-12) 105
Figure 5–6 Comparison of double integration results with displacement measurements (Test-13) 105
Figure 5–7 Comparison of double integration results with displacement measurements (Test-14) 105
Figure 5–8 Comparison of double integration results with displacement measurements (Test-15) 106
Figure 5–9 Comparison of double integration results with displacement measurements (Test-16) 106
Figure 5–10 Comparison of double integration results with displacement measurements (Test-17) 106
Figure 5–11 Comparison of double integration results with displacement measurements (Test-18) 107
Figure 5–12 Comparison of double integration results with displacement measurements (Test-19) 107
Figure 5–13 Pushover curve and drift ratios estimated using double-integration (Bent-1) 108
Figure 5–14 Pushover curve and drift ratios estimated using double-integration (Bent-2) 109
Figure 5–15 Pushover curve and drift ratios estimated using double-integration (Bent-3) 110
Figure 5–16 Elevation and plan view of Coronado bridge and sensors layout 112
Figure 5–17 Elevation and plan view of Coronado bridge and sensors layout 113
Figure 5–18 Response histories measured by channels 48, 49, 50, and 51 at pier 19 114
Figure 5–19 Relative drift ratios from double integration procedure 116
Figure 5–20 Stress-strain relationship models for (a) concrete01 (b) reinforcing steel 116
Figure 5–21 FE model of pier 19 117
Figure 5–22 Pushover curves in transverse and longitudinal directions, and drift ratios estimated by double integration 118
Figure 5–23 Flowchart of IDA-based residual capacity estimation method 119
Figure 5–24 (a) Spectral acceleration of LMSR-N ground motion set (b) IDA curves for the intact bridge 122
Figure 5–25 Post-earthquake modal frequencies of the bridge 123
Figure 5–26 Error between analytical and modal properties 126
Figure 5–27 (a)-(e) IDA curves of damaged structure (f) Median IDA curves for all realizations of damaged structure (W.N.2) 129
Figure 5–28 (a)-(e) IDA curves of damaged structure (f) Median IDA curves for all realizations of damaged structure (W.N.3) 130
Figure 5–29 (a)-(e) IDA curves of damaged structure (f) Median IDA curves for all realizations of damaged structure (W.N.4) 131
Figure 5–30 (a) Spectral accelerations of the tests (b) Seismic Hazard Curves for the southern California Region . 132
Figure 5–31 Tagging criteria and bridge status in different phases of experiment 134

LIST OF TABLES

Table 2-1 Test Procedure....17
Table 3-1 Modal identification results (W.N.1)....28
Table 3-2 Modal identification results (W.N.2)....29
Table 3-3 Modal identification results (W.N.3)....30
Table 3-4 Modal identification results (W.N.4)....31
Table 3-5 Modal identification results (W.N.5)....32
Table 3-6 Properties of the first transverse vibration (prediction error method)....68
Table 3-7 Properties of the first transverse vibration mode (subspace method)....68
Table 3-8 Properties of the second transverse vibration mode (prediction error method)....69
Table 3-9 Properties of the second transverse vibration mode (subspace method)....69
Table 3-10 Properties of the third transverse vibration mode (prediction error method)....70
Table 3-11 Properties of the third transverse vibration mode (subspace method)....70
Table 3-12 Comparison of modal data identified from white noise excitations....71
Table 3-13 Fitness distributions properties....74
Table 4-1 Weighting factors for J_1....86
Table 4-2 Calibration factors estimated using modal and time domain data....88
Table 4-3 FE model updating results using (J_1): stiffness correction factors....88
Table 4-4 FE model updating results using (J_1): error decomposition....89
Table 4-5 FE model updating results using (J_2)....90
Table 4-6 Average slopes and experimental stiffness indices (Bent-1)....95
Table 4-7 Average slopes and experimental stiffness indices (Bent-2)....96
Table 4-8 Average slopes and experimental stiffness indices (Bent-3)....97
Table 5-1 Maximum Drift Ratios (Bent-1)....108
Table 5-2 Maximum Drift Ratios (Bent-2)....109
Table 5-3 Maximum Drift Ratios (Bent-3)....110
Table 5-4 Residual capacity of the bridge....111
Table 5-5 LMSR-N ground motion set....121
Table 5-6 Experimental modal analysis results....124
Table 5-7 Weighting factors....126
Table 5-8 Best ground motion-intensity pairs....127
Table 5-9 Mean collapse capacity of the bridge....128

CHAPTER 1

INTRODUCTION

Over the past 20 years, Caltrans, with the assistance of the California Geological Survey (CGS), has instrumented 68 bridge structures throught California with strong motion sensors for the purposese of advancing understanding of how bridge structures react to seismic imput and validating dynamic modeling techniques. For the first time, this project explores the usage of the strong motion data for automated, remote, real-time damage assessment of bridges immediatly after a destructive event.

Various vibration-based damage assessment methods are investigated for post-event damage assessment from noisy and incomplete measurements. Vibration-based structural health monitoring and damage assessment can revolutionize the way we inspect the bridges, particularly for post-event damage assessment, in a rapid, remote, automated, and objective fashion. By installing appropriate sensors at critical locations on a bridge structure, transmitting the sensor data through a communications network, and analyzing the data through a software platform, the location and severity of bridge damage caused by earthquakes or other damaging events can be automatically, remotely, and rapidly assessed, without sending inspection crew to

the bridge site. In this report, various aspects of vibration-based damage assessment of bridges are investigated: from damage detection to identification of it characteristics and consequences on the current and future functionality of the bridge.

1.1 Literature Review

Over the past few decades, research on vibration-based health monitoring and damage assessment of civil engineering structures has produced substantial literature. Numerous techniques and procedures have been developed and applied for evaluation of real-world and laboratory-tested structures from their response measurements. Rytter [1] proposed a four-level hierarchy for classification of damage assessment techniques based on level of assessment provided by each technique: (1) detection of existence of damage within the structure (2) determination of geometric location of damage (3) quantification of severity of damage (4) investigation of damage consequences and prediction of remaining service life or capacity of the damaged structure. The following presents a concise literature review on the vibration-based methods and procedures applied for health monitoring, damage assessment and residual capacity estimation of bridge structures:

Several researchers have applied system identification techniques for global health monitoring of bridge structures through experimental modal analysis: Farrar et al.[2] applied modal identification and damage detection techniques for assessment of I-40 bridge from ambient and forced vibrations recorded at different damage states of the bridge. Shinozuka and Ghanem[3, 4] reviewed several system identification approaches and assessed their performance in modal identification of structures from the response to earthquake excitations. In another research by Farrar and James[5] the similarities between cross-correlation functions of the response measurements on an ambiently excited structure and the impulse responses of the system were

utilized for modal identification of a highway bridge. The standard time domain curve fitting procedures, typically applied to impulse responses, were used to estimate the natural frequencies and modal damping ratios of closely-spaced vibration modes of a highway bridge from traffic-induced vibrations. Loh and Lee [6] applied linear system identification methodology for health monitoring of a 5-span continuous bridge located in Taiwan from responses to both weak and strong earthquake ground motions. They concluded that response level of the bridge is an important factor in identified dynamic characteristics of the bridge. Feng et al.[7] used ambient vibrations of a large-scale structure under wind loading to identify modal properties and update stiffness matrix of the structure. The results of study were used for the design of an active mass damper system targeted to suppress wind-induced vibrations of the structure. Lus et al.[8] proposed a system identification methodology based on eigensystem realization algorithm and observer/Kalman filter identification approach to study the dynamic responses of Vincent-Thomas cable-stayed bridge, located in the Los Angeles metropolitan area, during 1987 Whittier and 1994 Northridge earthquakes. The identified mathematical models for the bridge were shown to have excellent agreement with the real systems in predicting the structural response time histories when subjected to earthquake-induced ground motions. Smyth et al.[9] used a combination of linear and non-linear system identification techniques to study the dynamic responses of Vincent Thomas Bridge to the Whittier and Northridge earthquakes. The results of study showed that the apparent nonlinearities in the system restoring forces were quite significant, and application of equivalent linear modal properties contributed substantially to the improved fidelity of the model. Weng et al.[10] applied two system identification techniques named as frequency domain decomposition and stochastic subspace identification, for modal identification of a cable-stayed bridge from response measurements acquired by a wireless array

of sensors. He et al. [11] applied three time and frequency domain system identification techniques for identification of modal properties of the Alfred Zampa memorial long-span suspension bridge from ambient and forced vibrations tests. The experimental modal properties of the few contributing modes to the measured bridge vibration were found in good agreement with FE model analysis results. Comprehensive reviews of the experimental modal analysis techniques are presented by Ewins[12] and Maia and Silva[13].

More recently, there has been growing interest in using time-frequency decomposition techniques to study the nonstationary and nonlinear vibrations of the structures. Thus far, non-parametric methods such as short-time Fourier transform (STFT), Wigner-Ville distributions, Hilbert transform and wavelet-based methods are the most widely applied methods for time-frequency analysis of such systems. However, parametric model estimation methods such as prediction error minimization and subspace methods offer a number of potential advantages over the conventional non-parametric methods including representation parsimony, improved accuracy, resolution, and tracking, as well as flexibility in analysis, simulation and prediction[14]. Dalianis et al.[15] utilized the concept of generalized transfer function as a higher order system representation for the analysis of nonstationary systems. They successfully applied the proposed methodology to identify the time-dependent dynamic characteristics of a variable-mass cantilever beam. Owen et al.[16] studied the application of auto-regressive time series modeling for time-frequency analysis of nonstationary data from large amplitude responses of a cable-stayed bridge to wind excitation and nonlinear data from modal testing of cracked reinforced concrete beams. The results of study indicated the high sensitivity of the auto-regressive models to their design parameters (e.g. model order) for such applications. Nelid et al.[17] provided a general review of time-frequency methods for structural vibrations analysis. They studied the

nonlinear vibrations of a cracked beam at different crack-width levels using four time-frequency decomposition techniques. The study was supplemented by the results of another research by the same authors for damage assessment of the cracked beams from time-frequency analysis results[18]. Nagarajaiah and Li[19] presented a multi-input multi-output system identification technique, named as time segmented least square technique, that was applied for tracking piecewise linear representations of nonlinear behavior of a base-isolated building structure. Marchesiello and Garibaldi[20] proposed Nonlinear Subspace Identification technique handling the system nonlinearities as internal feedback forces. Results of application of the methodology to three numerical examples indicated the good conditioning and computational efficiency of the technique even with short data series. In another research by Marchesiello et al.[21], time-dependent dynamic properties of bridge structures with crossing loads were investigated using short-time stochastic subspace identification methods. A comprehensive review of parametric time domain methods for analysis of nonstationary random vibrations is presented by Poulimenos and Fassois [22].

Although experimental modal analysis can provide important information about the existence of damage throughout the structures, most often it does not provide the answer to the questions about the characteristics of the structural damage. Several methods and procedures have been developed and applied for vibration-based structural damage characterization. A rich source of damage identification methods has come from the finite element (FE) model updating literature[23]. The first step toward vibration-based damage assessment of structures through FE model updating is to develop a relatively accurate FE model of the structure that, potentially, can capture significant vibration characteristics of the real system. A priori knowledge about the structure and engineering expertise should be used to tackle several issues which arise during FE

model development, such as determination of the size and complexity level of the FE model, selection of the proper set of model parameters and their respective ranges. The second step consists of updating the FE model parameters by minimizing the objective function expressing the discrepancy between dynamic properties predicted by the FE model and the ones identified from measurements. Comparisons of the updated model parameters with the baseline model parameters can be used to identify the location and extent of damage throughout the structure. A comprehensive review of the literature in the area of finite element model updating is presented by Mottershead and Friswell [24]. The success of the FE model updating approach in accurate and reliable identification of damage is highly dependent on the performance of adopted optimization technique in convergence to the global minimum of the objective function. In the past few decades, many classical optimization techniques have been developed and applied to structural damage identification problems. Most of these techniques are calculus-based search techniques which utilize a point-to-point search strategy. A good initial guess of the parameter(s) and gradient or higher-order derivatives of the objective function are generally required and there is always a possibility to fall into a local minimum rather than the global minimum. On the other hand, evolutionary-based Genetic Algorithm (GA) optimization technique is a stochastic search algorithm based on heuristic concepts of natural evolution. By conducting a population-to-population search, GA is significantly more likely to converge to the global solution; Moreover, it does not require any information about the derivatives of the objective function, which makes it suitable for discontinuous, non-differentiable, stochastic or highly non-linear problems involving many parameters. Since introduced by Holland [25], many GA applications have been performed on a variety of optimization problems in the engineering area including civil engineering. Currently, interest in applying these techniques to structural damage assessment

problems is increasing. Some applications in the context of structural damage identification are reviewed as follows:

In the study by Friswell et al.[26], genetic and eigensensitivity algorithms were used to optimize the discrete damage location variables and their extents from natural frequencies. Chou and Ghaboussi [27] utilized GA to identify the changes of the characteristic properties of structural members of a truss by minimizing an objective function defined as a function of difference between the measured and analytical responses under static loading. Hao and Xia [28] used GA for damage detection of a laboratory tested cantilever beam and a frame structure. The objective function was defined as weighted error between experimental and FE model predicted natural frequencies and mode shapes. The results of the sensitivity analysis on the error weights showed that cases with lower mode shape to frequency weight values yielded more accurate results. Koh et al.[29] combined GA with two local search operators to improve the computational efficiency of the optimization procedure. Au et al. [30] studied the effectiveness of GA in structural damage assessment using incomplete and noisy modal test data. Franco et al. [31] proposed a parameter estimation technique based on an evolutionary strategy. The model parameters (mass, damping and stiffness) of various structural systems were estimated by direct matching of the simulated response with the measured response of the structure in time domain. Perera and Torres [32] compared the performance of GA in minimization of two objective functions defined based on eigenvalue equations and modified total modal assurance criterion. The results of an experimental study on an aluminum beam showed that the application of latter objective function produced more accurate damage prediction results.

Comprehensive reviews of the vibration-based structural damage assessment literature presented by Doebling et al.[33] Sohn et al.[34] and Carden and Fanning[35] show that majority of existing

damage assessment techniques focus on one of the first three levels of the hierarchy proposed by Rytter, without addressing the consequences of damage on the functionality status and remaining service life of the structure. Within the framework of performance based earthquake engineering, several methods and procedures have been developed for seismic performance evaluation and residual collapse capacity estimation of structures.

The nonlinear static procedure, known as pushover analysis is a widely accepted method that has become standard among practicing engineers for estimating seismic deformation demands as well as local and global capacities of the structures and also for evaluation of the safety of the structures against an earthquake-induced collapse. The procedure is introduced in FEMA 273 [36] and updated in FEMA 356 [37]. In 1997, Bracci et al. [38] proposed a 5-step methodology based on adaptive pushover analysis for seismic performance and retrofit evaluation of reinforced concrete structures. Several investigators [39, 40] have found that the procedure may not provide an accurate assessment of the structure behavior and may lead to gross underestimation of the demand and may fail to identify the failure pattern throughout the structure. In recognition of these deficiencies, several improved versions of the procedure have been proposed [41-43]. In fact improved procedures lead to better predictions in some cases, but none of them have been proven to be universally applicable [44].

Incremental dynamic analyses have recently emerged as powerful means to study the overall behavior of the structures, from their elastic response through yielding and nonlinear response and all the way to global dynamic instability [44]. Incremental dynamic analyses have been studied extensively lately by several investigators [45, 46]. Ibarra and Krawinkler[47] studied the global collapse of deteriorating multi-degree-of-freedom (MDOF) frame structures using IDA curves. They concluded that the collapse capacity of a structure strongly depends on post-

capping stiffness, ductility capacity of the rotational hinges and the first-mode period of the MDOF system. The second order P-Δ effects were recognized as accelerating components in the collapse of such systems, while cyclic deterioration was reported as an important but not dominant issue. Bazzurro et al.[48] proposed a six-step procedure based on incremental dynamic analyses to estimate the residual collapse capacity and corresponding occupancy status of a building for each of the previously identified damage states of the structure. In a parallel research, Luco et al. [49] compared the residual capacities estimated based on static pushover curves and incremental dynamic analysis curves and concluded that the static computation of the residual collapse capacity generally underestimates the more accurate results found by incremental dynamic analysis curves.

1.2 Scope of the Report and Organization of Material

This report focuses on development, application and verification of several vibration-based methodologies for health monitoring, damage identification and residual capacity estimation of reinforced concrete bridges. Experimental measurements during a shake table experiment on a large-scale reinforced concrete bridge structure were utilized for performance evaluation of the presented methodologies. The wide range of realistic seismic damage induced to the bridge structure at different stages of the experiment provides a unique opportunity to examine the efficacy of the presented methodologies at various structural damage levels. Contents of this report are organized in the following order:

Chapter 2 presents the details of the shake table experiment including test specimen properties, instrumentation and test procedure. Chapter 3 addresses the structural health monitoring of the bridge from both ambient vibrations and responses to earthquake base excitations. Structural damage assessment results through finite element model updating approach are presented in

chapter 4. Proposed residual capacity estimation procedures and corresponding results are presented in chapter 5; and finally the conclusions of this study are presented in chapter 6.

CHAPTER 2

EXPERIMENTAL SETUP, TEST SPECIMEN AND INSTRUMENTATION

2.1 Background

Catastrophic earthquakes over the past two decades which have caused immeasurable devastation, including extensive economic impacts and loss of lives, have directed considerable effort toward improving the seismic performance of the world's infrastructure systems including highway bridges. A vast amount of experimental research has been concentrated on broadening the technology to calculate the nonlinear response and understanding the performance of highway bridges under earthquake loadings. Numerous experiments have been performed on components of bridge systems to improve and validate modeling techniques and to evaluate the old and novel design procedures. However, due to limitations of earthquake testing facilities, large scale system level experiments have generally not been conducted. To fill in the gap in the earthquake engineering experimental research, the George E. Brown Network for Earthquake Engineering Simulation (NEES) was founded under National Earthquake Hazards Reduction Program (NEHRP) through the National Science Foundation (NSF). The Multiple shake table

facility at University of Nevada, Reno (UNR) is one of the fifteen NEES experimental research facilities that plays a significant role in experimental earthquake engineering research.

The experiment that is investigated within this report is a part of collaborative research to study soil-foundation-structure-interaction (SFSI) of bridge systems using the state-of-the-art experimental facilities available in UNR. During the experiment, the bridge specimen was subjected to a series of earthquake excitations introducing progressive damage to the bridge structure which finally led to the failure of a bent of the bridge. Considering the fact that there has been no experimental work that includes the failure of a large scale reinforced concrete bridge, comprehensive measurements during this experiment provide a unique opportunity to evaluate the reliability and accuracy of the proposed health monitoring, damage assessment and residual capacity estimation procedures for the case of a large-scale structure and in presence of extensive seismic damage.

2.2 Bridge Specimen

The prototype for the experimental studies (figure 2–1) is a two-span frame of a cast-in-place post-tensioned reinforced concrete box girder bridge. The span lengths are 121.35 ft (37.00m), and the substructure is composed of 3.94 ft (1.20 m) diameter 2-column piers on extended pile foundations. Seismic detailing of the prototype was based on the Caltrans SDC (Caltrans 2003) and NCHRP12-49 Recommended LRFD Guidelines for the Seismic Design of Highway Bridges (ATC/MCEER 2001). General design of the prototype was based on the American Association of State Highway and Transportation Officials AASHTO bridge specifications (AASHTO 2002).

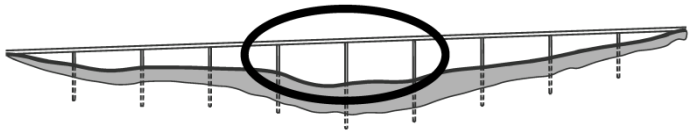

Figure 2–1 Example of prototype location in a multi-span bridge

The bridge specimen is designed to model the system interaction between three two-column bents of varying heights. It is created at quarter-scale to maximize the size of the specimen while remaining below the capacity of the shake tables. The total length of the bridge is 67.24 ft (20.50 m) that includes two spans of 30.00 ft (9.15 m) length and two cantilevered sections of 3.61 ft (1.10m) length. The bridge specimen has three double-column bents with varying clear heights of 6.00 ft (1.83 m), 8.00 ft (2.44 m), and 5.00 ft (1.52 m) with the tallest bent in the middle. All the columns of the specimen have circular sections of 0.98 ft (0.30 m) diameter with 1.56% longitudinal steel ratio and 0.90% spiral reinforcement ratio. The axial load index[1] for the bridge prototype is set at 8.2% which represents a typical value for column axial load level of highway bridges and is equivalent to a column axial load of 46.49 kip (206.8 kN). Due to the scaling effects, masses of the quarter-scale model provide a smaller axial stress than in the prototype scale. Therefore to match the column axial load indices of the of the prototype and test specimen, additional weights in the forms of concrete blocks of 120.05 kip (534.0 kN) and lead pallets of 58 kip (258.0 kN) are firmly attached to the superstructure of the bridge. The superstructure of the bridge consists of six precast reinforced concrete beams post-tensioned in transverse and longitudinal directions to function as a monotonic and continuous superstructure in both directions. However, the gaps provided at the connections of the beams and the cap beams cause the superstructure to perform as two independent simply supported spans in vertical direction.

[1] Axial load index is defined as the ratio of the axial load and the product of the gross section and the specified concrete compressive strength

Because of the high strength and stiffness of the prototype superstructure compared to the substructure, the superstructure remains essentially elastic when the bridge is subjected to seismic excitations. Also, because of the post-tensioning of the beams, the superstructure remained generally un-cracked during the whole experiment. Schematic views of the test specimen are presented in figure 2–2.

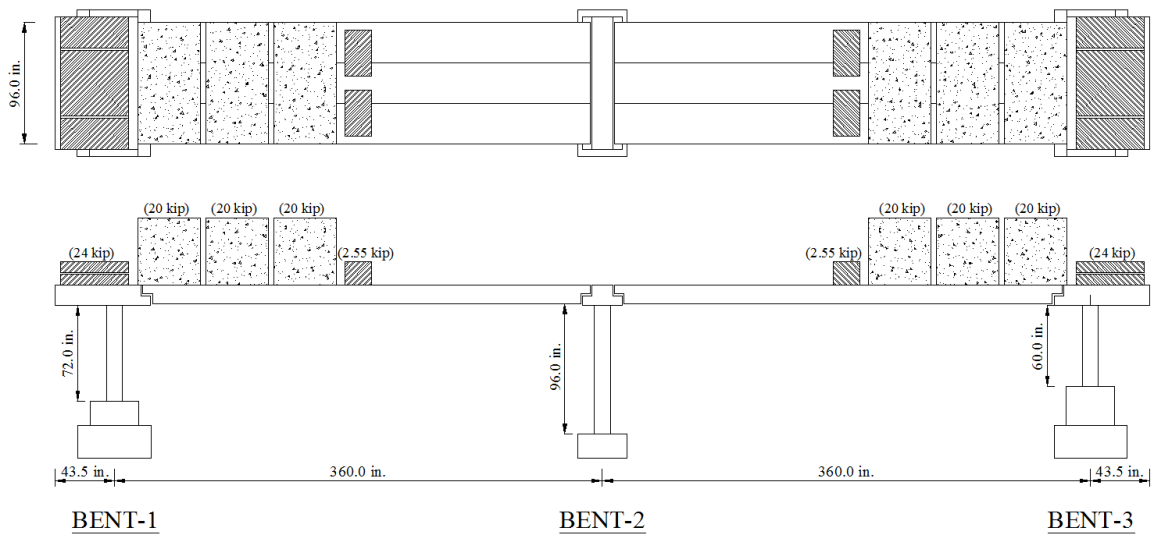

Figure 2–2 Schematic views of the bridge specimen

2.3 Instrumentation and Sensor Layout

The bridge specimen and the shake tables were instrumented with 298 working channels of displacement transducers, accelerometers, and strain gauges. The data were recorded at a rate of 100 Hz using both National Instruments and Pacific Instruments data acquisition systems. The superstructure of the specimen was instrumented with 14 accelerometers and 25 displacement transducers. The accelerometers were Crossbow high sensitivity LF series with a measurement range of plus or minus 2.00 g. The displacement transducers were UniMeasure PA series displacement transducers with a stroke of 3.35 ft (1.02 m). Displacements of the superstructure were measured in the transverse and vertical directions at the top of each bent and at the mid-

spans of the superstructure. Superstructure accelerations were measured at the top of each bent in both longitudinal and transverse directions of the superstructure. At both mid-spans of the superstructure accelerations were measured in all three orthogonal directions. The built-in instruments of the shake tables were used to measure displacements and accelerations of the shake tables. Figure 2–3 presents the layout of the accelerometers and displacement transducers installed on the superstructure of the bridge specimen.

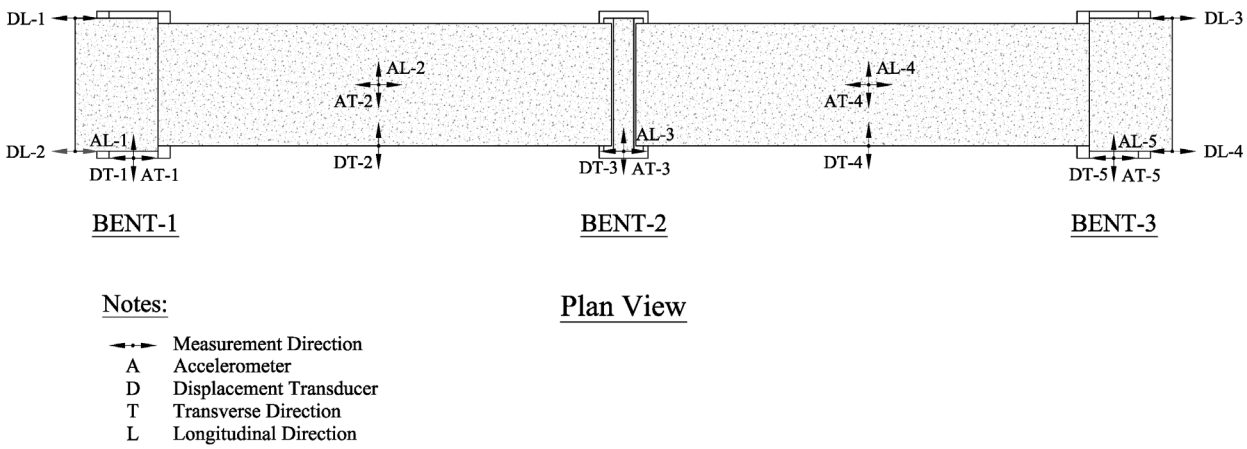

Figure 2–3 Sensor layout of the superstructure of the bridge specimen

2.4 Test Procedure

The bridge specimen was subjected to a series of earthquake and white noise excitations in transverse direction of the bridge. The high amplitude earthquake input motions were coherent for the three shake tables. The input motion signal were calculated based on the 1994 Northridge earthquake as recorded from the ground station at the Century City Country Club North. For successive tests, scaled versions of the earthquake time history with peak ground accelerations ranging from 0.08 g to 1.66 g were utilized. White noise excitations were low amplitude coherent motions that were not large enough to induce any damage to the bridge. The acceleration history used as “white noise” was a random motion having a peak ground acceleration of 0.10 g and

frequency range of 1~30 Hz that lasted for approximately 60 seconds. The advantage of the white noise inputs was that, due to their wide frequency range, they could excite all of the significant modes of vibration of the bridge in transverse direction. Square wave motions were also applied following each white noise test to subject the bridge to free vibration and restore it to equilibrium position. The sequence of input motions to the bridge specimen is listed in table 2-1. Damage descriptions provided in the last column of the table 2-1 reflects the results of visual inspections and longitudinal reinforcement strain gauge monitoring at the critical sections of the columns of the bridge specimen. Time-frequency decompositions of sample earthquake input motion (Test-12) and a white noise excitation (W.N.1) are presented in figure 2–4. The spectral acceleration curves corresponding to input earthquake ground motions are plotted in figure 2–5.

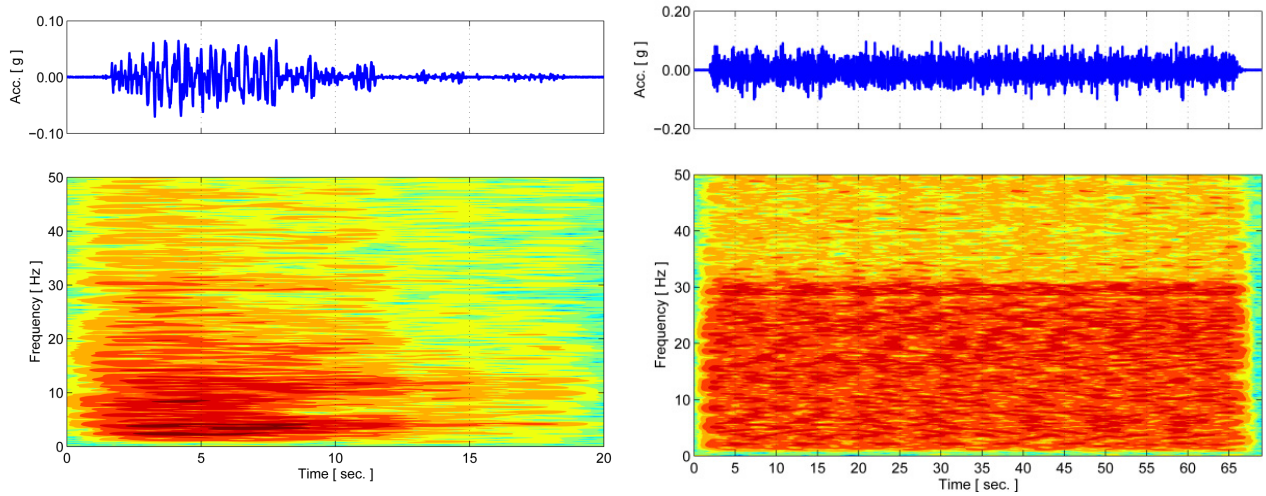

Figure 2–4 Short-time Fourier transform of (a) earthquake and (b) white noise excitations

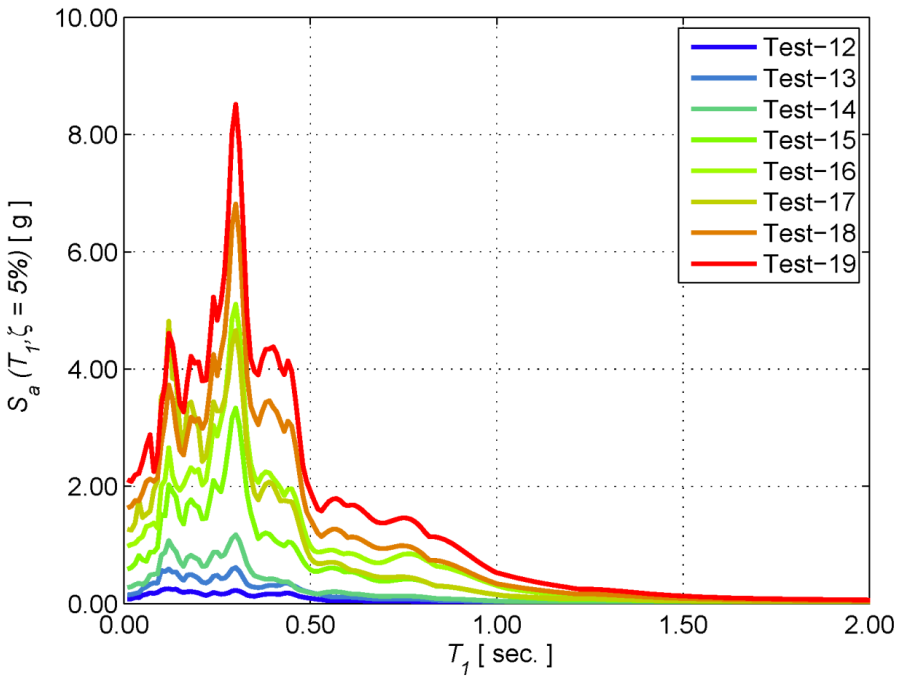

Figure 2–5 Spectral acceleration curves corresponding to input earthquake excitations

Table 2-1 Test Procedure

Test	Ground Motion Description	PGA (g)	Damage Description
W.N. 1	White Noise	0.100	
TEST 12	Low Earthquake	0.075	
TEST 13	Low Earthquake	0.150	Bent 1 Yields
TEST 14	Moderate Earthquake	0.250	Bent 3 Yields
W.N. 2	White Noise	0.100	
TEST 15	High Earthquake	0.500	Bent 2 Yields
TEST 16	High Earthquake	0.750	
TEST 17	High Earthquake	1.000	
W.N. 3	White Noise	0.100	
TEST 18	Severe Earthquake	1.330	
W.N. 4	White Noise	0.100	
TEST 19	Extreme Earthquake	1.660	Bent 3 Steel Buckles
W.N. 5	White Noise	0.100	

2.5 Material Properties

In order to guarantee the consistency of the concrete and reinforcing steel properties with the design requirements and the properties of the materials that were used in the prototype bridge, constitutive relationships for the concrete and reinforcing steel materials utilized during the construction of the bridge specimen were calculated through appropriate material testing procedures[50]. The results of testing procedures, reported by NEES@Reno research group were used in generation of linear and nonlinear FE models of the bridge. The following presents a brief review of the material testing results:

The concrete material had a 0.37 in (9.50 mm) maximum aggregate size and was rated for an unconfined compressive strength of 5003.80 psi (34.50 MPa) with expected cured strength ranging from 4496.17 psi (31.00 MPa) to 6004.56 psi (41.40 MPa). The unconfined compressive strength of the concrete used in the columns measured at the end of shake table experiment was 5903.04 psi (40.70 MPa) while the unconfined concrete compressive strength for the cap beams, spacer blocks, beams and footings ranged from 4800.75 psi (33.10 MPa) for the footings, to 7193.87 psi (49.60 MPa) for the superstructure beams.

Tensile testing was conducted for both the lateral W2.9 spiral wire reinforcement and the #3 longitudinal bar reinforcement in the columns. All the reinforcements used in the construction of the bridge were of Grade-60 type. The average measured yield and ultimate stresses for the wire was 67007.43 psi (462 MPa) and 80060.83 psi (552 MPa), respectively with the elastic modulus of 27557.17 ksi (190 GPa). The average yield and ultimate strength for the #3 reinforcing bar was 66572.32 psi (459 MPa) and 97030.25 psi (669 MPa), respectively with the elastic modulus of 29007.55 ksi (200 GPa). Detailed material testing results and constitutive relationships may be found in CCEER-06[50] report provided by the NEES@Reno research group.

2.6 Observed Shake Table Experiment Results

A brief review of the observed behavior of the bridge specimen during the shake table experiment is presented in this section. The observations included physical inspection of the state of the bridge between the tests that were documented as written events, drawings, and photographs at key locations (figure 2–6 and figure 2–7). Data recordings such as strains, displacements and accelerations were also monitored during the experiment to track the response and understand the damage state of the bridge.

During the experiment, no damage was observed in the superstructure of the bridge including the cap beams, beams and their longitudinal and transverse post-tensioning strands. No visible damage was observed within the footings of the bents and their bolted connections to the shake tables. The status of the added weights and their anchorage system to the superstructure of the bridge was reported intact after final stage of the high-amplitude earthquake excitations.

No damage was observed in the bridge till after test-13. During the test-13, initial hairline flexural cracks developed in bent-1. Flexural cracking began in bent-3 and became significant in the columns of both bent-1 and bent-3 during test-15. Also during test-15, initial hairline cracks began to develop in bent-2. During test-17, significant concrete spalling exposed the column lateral reinforcement in both bent-1 and bent-3. Significant spalling and exposure of lateral column reinforcement in bent-2 became evident during test-18. Also during test-18, the longitudinal reinforcement of bent-3, the shortest of the bents, became exposed and initial buckling was observed on the bottom west side of the west column. Both columns of bent-3 failed in flexure during test 19. The top and bottom of bent 3 columns experienced significant plastic hinging and crushing of the core concrete. Four of the bent-3 spirals fractured, and 36 longitudinal bars buckled.

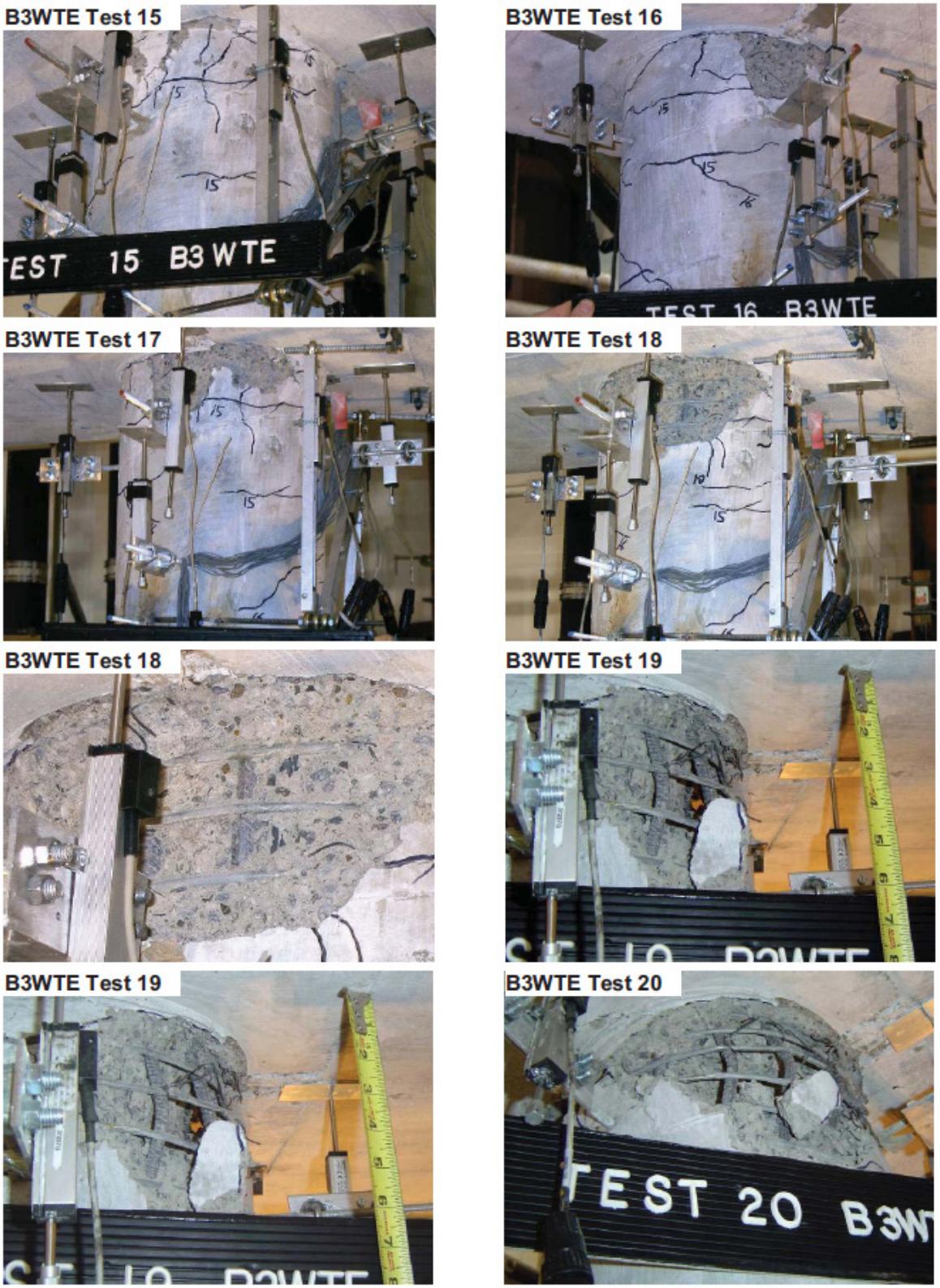

Figure 2–6 Damage progression @ Bent-3 (Top of west column)

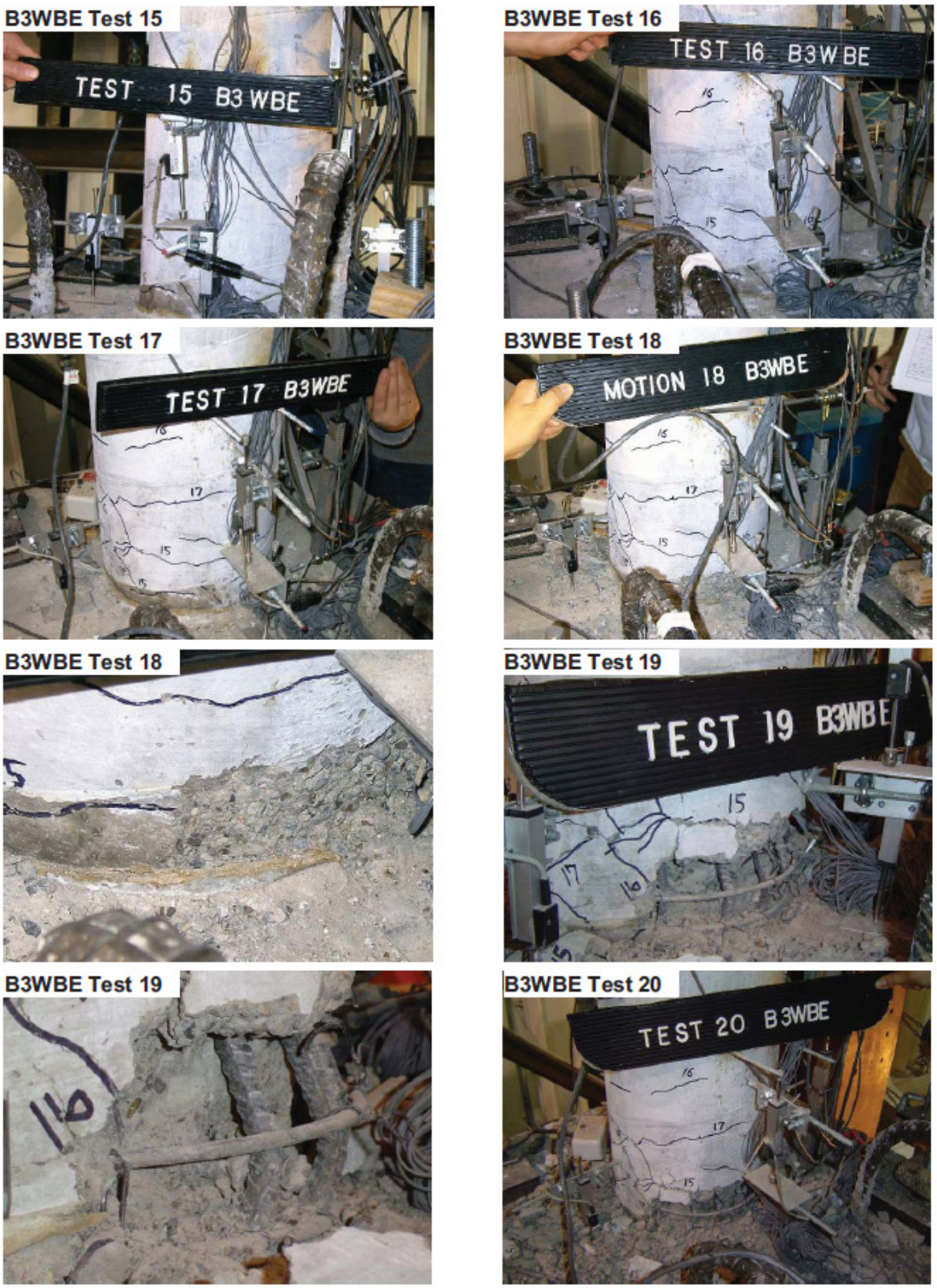

Figure 2–7 Damage progression @ Bent-3 (Bottom of west column)

CHAPTER 3

STRUCTURAL HEALTH MONITORING THROUGH EXPERIMENTAL MODAL ANALYSIS

3.1 Background

Experimental modal analysis of a structural system is the process of determining the dynamic characteristics of a linear, time-invariant structure including natural frequencies, damping ratios, modal shapes and modal scaling factors from vibration measurements. Predominately, experimental modal analysis is used to explain dynamic problems that are not obvious from intuition, available analytical models, or previous similar experience. Although experimental modal analysis may not provide the final answers to all inquiries of typical damage assessment problems, but it offers critical information about the dynamic characteristics of the structures which are the basic inputs for many damage assessment methodologies. It is also important to mention that many vibration analysis problems fall outside of the basic assumptions associated with the experimental modal analysis (linearity of the system for example). For these situations, one of the available alternatives should be selected based analyst's engineering judgment.

As mentioned earlier, the bridge specimen tested during the shake table experiment was subjected to two types of input excitations: (1) White noise excitations which were input to

bridge to mimic the ambient vibrations of the structure and due to their low amplitude could not induce any damage to the bridge structure. The bridge response to these excitations is assumed linear and time-invariant (2) Earthquake excitations which were targeted to induce progressive seismic damage to the lateral force resisting elements of the bridge specimen. Due to the damage and associated nonlinear characteristics during earthquake excitations, basic assumptions of conventional modal identification techniques do not hold for the total response of the bridge to these excitations. For experimental modal analysis of the bridge from the responses to white noise and earthquake excitations two system identification approaches are proposed and applied. An output-only frequency domain system identification technique, named as frequency-domain decomposition (FDD) technique, is utilized for modal identification from the response to the white noise excitations. For the analysis of nonlinear responses of the bridge to the high amplitude earthquake excitations, a three-step procedure is proposed. The proposed procedure takes advantage of robust time-domain system identification techniques for time-frequency analysis of the response during earthquake excitations. The obtained time-frequency representation is subsequently used for identification of linear and stable segments of the response from which modal properties of the specimen are identified. Details of the mentioned modal identification methodologies are presented in the following sections.

3.2 Modal Identification from White Noise Excitations

Vibrations of the bridge specimen during white noise excitations resemble the ambient vibrations of the civil engineering structures under environmental and/or operational loadings such as wind-induced vibrations or motions caused by vehicles or pedestrians traffic. Normally, in these cases the input loads are unknown, and thus, modal identification has to be carried out based on response measurements only. The FDD technique is an output-only system identification

technique which is an extension of classical frequency domain approach often referred to as basic frequency domain (BFD) technique or peak picking technique. The main advantages of classical approach over other approaches such as Ibrahim time domain or stochastic subspace identification techniques can be summarized as simplicity, user-friendliness and low computational cost. However in modal identification using BFD technique, the modal frequency estimations are limited by frequency resolution of spectral density functions, detection of close vibration modes can be difficult and, even if detectable, estimates of such modes could be heavily biased. Frequency domain decomposition technique, removes all disadvantage associated with BFD technique while keeping important features of simplicity and user-friendliness[51]. The theoretical background of the technique is presented in the following section.

3.2.1 Frequency Domain Decomposition Technique

The relationship between unknown inputs, $x(t)$, and the measured responses, $y(t)$, can be expressed as:

$$G_{yy}(j\omega) = \bar{H}(j\omega)G_{xx}(j\omega)H(j\omega)\,. \tag{3-1}$$

Where $G_{xx}(j\omega)$ is the power spectral density (PSD) matrix of the input, $G_{yy}(j\omega)$ is the PSD matrix of the output responses and $H(j\omega)$ is the frequency response function (FRF) matrix and the overbar and superscript T denote the complex conjugate and transpose, respectively. The FRF can be written in partial fraction form:

$$H(j\omega) = \sum_{k=1}^{n} \frac{R_k}{j\omega - \lambda_k} + \frac{\bar{R}_k}{j\omega - \bar{\lambda}_k}\,. \tag{3-2}$$

Where n is the number of the modes, λ_k is the pole and R_k is the residue:

$$R_k = \phi_k \gamma_k^T \tag{3-3}$$

Where ϕ_k and γ_k are the mode shape vector and modal participation factor respectively. For the case of white noise input ($G_{xx}(j\omega) = C$) the output PSD can be written as:

$$G_{yy}(j\omega) = \sum_{k=1}^{n} \frac{A_k}{j\omega - \lambda_k} + \frac{\overline{A}_k}{j\omega - \overline{\lambda}_k} + \frac{R_k}{-j\omega - \lambda_k} + \frac{\overline{R}_k}{-j\omega - \overline{\lambda}_k}. \tag{3-4}$$

Where A_k is the k th residue matrix calculated as:

$$A_k = R_k C(\sum_{s=1}^{n} \frac{R_s}{-\lambda_k - \lambda_s} + \frac{\overline{R}_s}{-\lambda_k - \overline{\lambda}_s}). \tag{3-5}$$

The contribution to the residue from the k th mode is given by:

$$A_k = \frac{R_k C R_k^T}{2\alpha_k}. \tag{3-6}$$

Where α_k is the minus the real part of the pole $\lambda_k = -\alpha_k + j\omega_k$. For the case of lightly damped structures A_k becomes proportional to the mode shape vector:

$$A_k \propto R_k C R_k^T = \phi_k \gamma_k^T C \gamma_k \phi_k^T = d_k \phi_k \phi_k^T. \tag{3-7}$$

Where d_k is a scalar constant. At a certain frequency, ω, only a limited number of modes will contribute significantly which are denoted as $sub(\omega)$. As a result, the output PSD matrix of a lightly damped structure with white noise excitation can be written as:

$$G_{yy}(j\omega) = \sum_{k \in sub(\omega)} \frac{d_k \phi_k \phi_k^T}{j\omega - \lambda_k} + \frac{\overline{d}_k \overline{\phi}_k \overline{\phi}_k^T}{j\omega - \overline{\lambda}_k}. \tag{3-8}$$

which represents the modal decomposition of PSD matrix of the measured responses.

The first step in system identification using frequency domain decomposition technique is to estimate the PSD matrices, of the response measurement signals. The PSD matrix at each discrete frequency, ω_i, can be directly estimated by taking the Fourier transform of the cross-correlation matrices of the output signals. The estimated PSD matrices ($\hat{G}_{yy}$) at discrete

frequencies, ω_i, are then decomposed by applying singular value decomposition (SVD) technique:

$$\hat{G}_{yy}(j\omega_i) = U_i S_i U_i^H \tag{3-9}$$

where $U_i = [u_{i1}, u_{i2}, ..., u_{im}]$ is the unitary matrix of singular vectors; S_i is the diagonal matrix of the singular values, s_{ij}, and the superscript H denotes the complex conjugate and transpose.

In the proximity of the peak corresponding to natural frequency of the kth mode of vibration, this mode and possible close modes will dominate the response. If only one mode is dominating the first singular vector, u_{i1}, is an estimate of the mode shape and the corresponding singular values around the peak comprise the auto-PSD function of the SDOF system that have the same dynamic properties as that vibration mode. The limits of the auto-PSD function of each mode are, normally, identified by comparing the mode shape estimate (singular vector at the peak frequency) with the singular vectors for the frequency lines around the peak. As long as the singular vectors are in good agreement with the estimated mode shape, the corresponding singular value is assumed to be a part of SDOF auto-PSD function. Modal assurance criterion (MAC) is used to quantify the consistency between singular vectors and estimated mode shapes:

$$MAC(\varphi_1, \varphi_2) = \frac{\left(\varphi_1^T . \varphi_2\right)^2}{\left(\varphi_1^T . \varphi_1\right) . \left(\varphi_2^T . \varphi_2\right)} \tag{3-10}$$

The MAC value ranges between zero and unit. The higher values of the MAC indicate the better match between mode shape vectors. For the modal analysis of the bridge specimen, the range of each auto-PSD function is limited to the singular values which their corresponding singular vector have MAC values of 0.90 and higher with the estimated mode shape vector. After SDOF systems corresponding to all significant modes of vibration of the structure are identified, the

auto-PSD functions are taken back to time domain by an inverse Fourier transform (IFFT) to accurately calculate the modal frequencies and damping ratios from crossing times and logarithmic decrement of the auto-correlation function corresponding to each mode. The modal identification procedure through FDD technique is shown in figure 3–1.

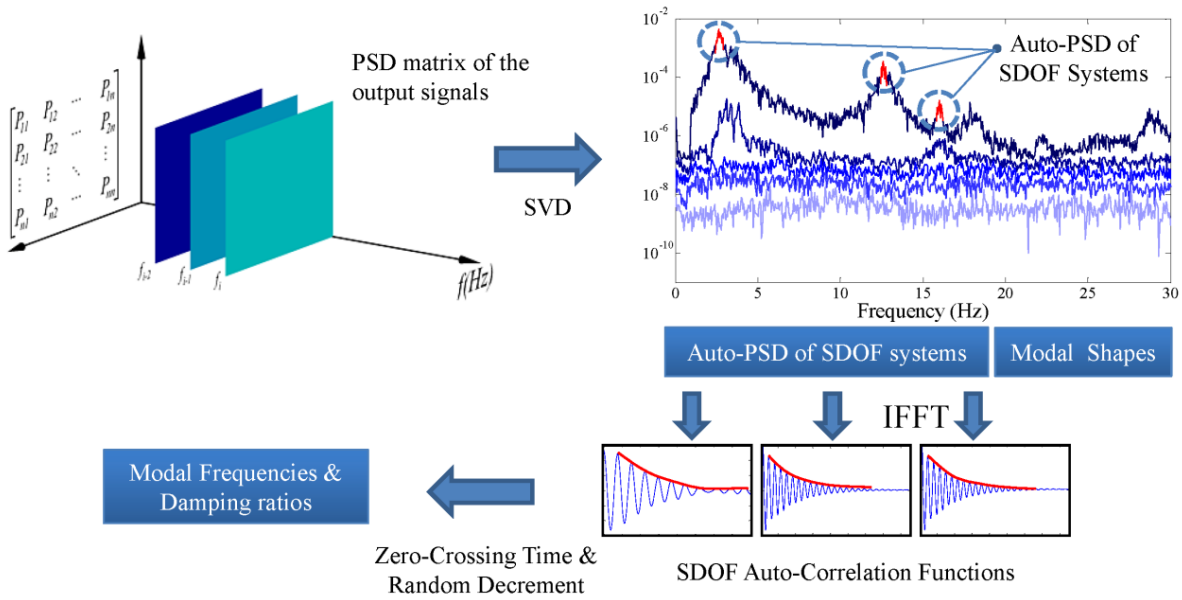

Figure 3–1 Modal identification procedure using FDD technique

3.2.2 Application of FDD Technique to Bridge Response Measurements

The FDD technique is applied for identification of modal properties of the bridge specimen from the response measurements on the superstructure during white noise excitations. In order to minimize the effect of noise on the modal identification results, the PSD matrices of the response measurements are estimated using Welch's averaging method with Hamming window function of 20.48 second long and 50% overlapping factor. The singular values of output PSD matrices during white noise excitations (W.N.1~5), calculated auto-correlation functions and complex representation of the modal shape vectors are presented in figure 3–2 through figure 3–6 and table 3-1 through table 3-5.

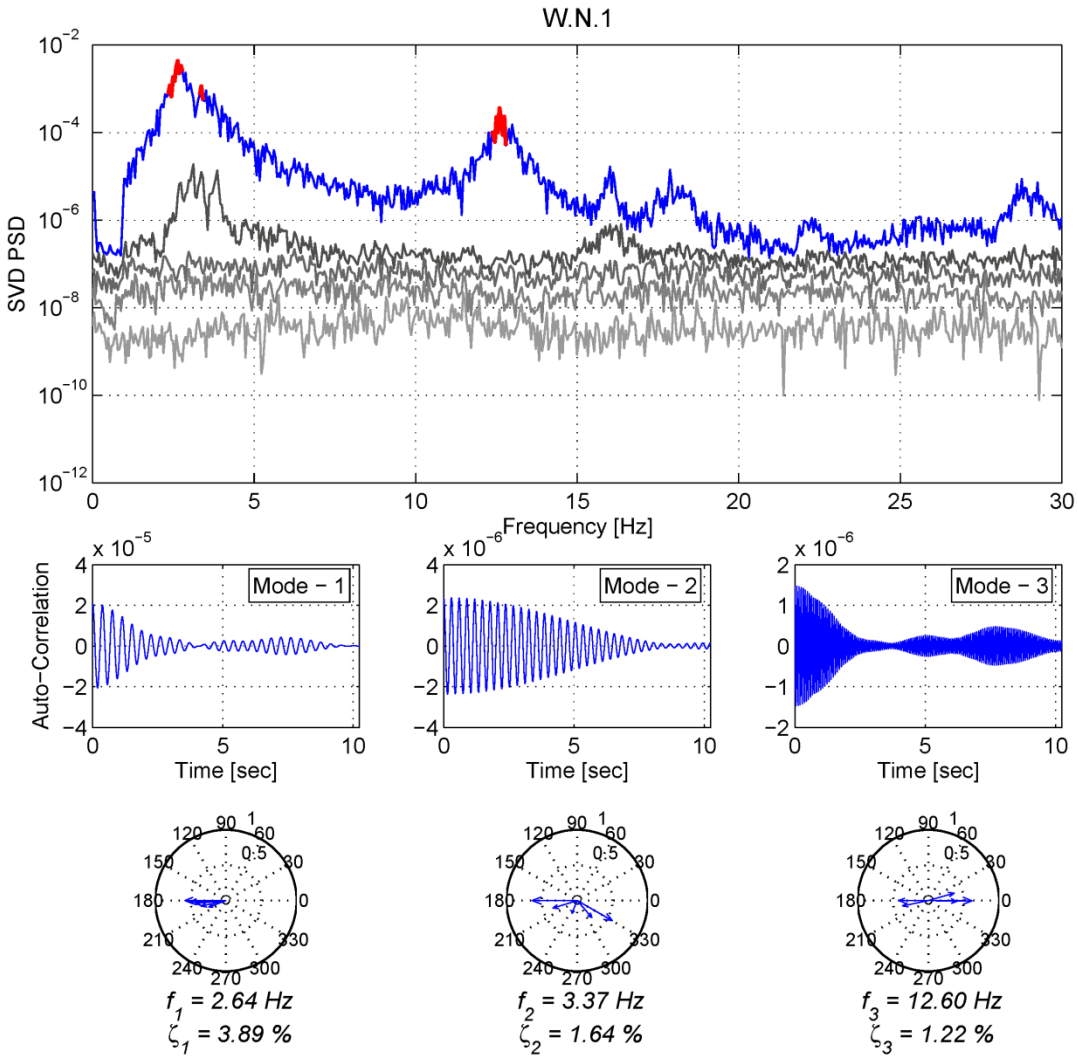

Figure 3–2 Modal identification using FDD technique (W.N.1)

Table 3-1 Modal identification results (W.N.1)

Mode #	f_i	ζ_i	Mode Shape				
			ϕ_{1i}	ϕ_{2i}	ϕ_{3i}	ϕ_{4i}	ϕ_{5i}
1	2.703	3.89%	-0.582	-0.523	-0.438	-0.360	-0.257
2	3.351	1.64%	-0.634	-0.359	-0.196	0.322	0.572
3	12.621	1.22%	-0.417	0.405	0.616	0.380	-0.373

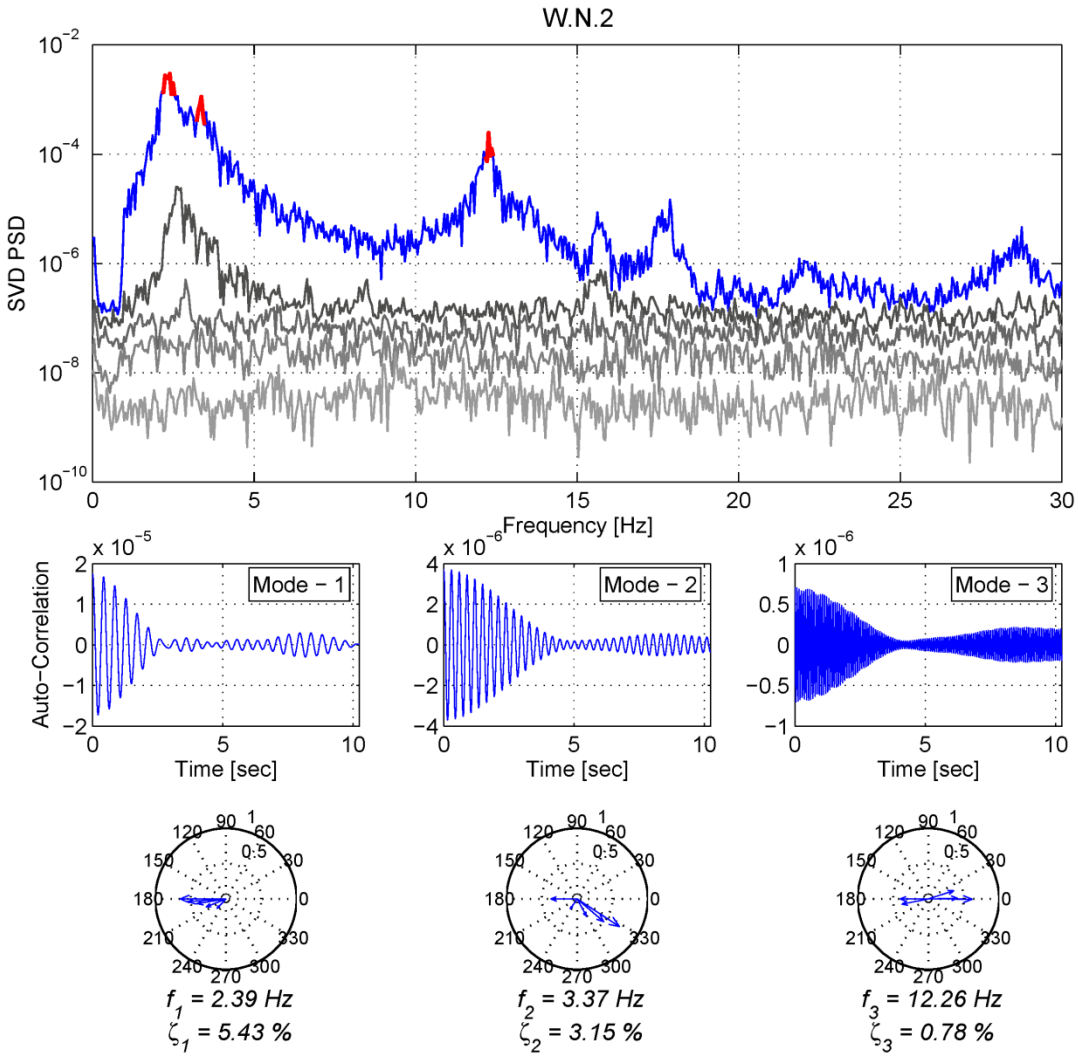

Figure 3–3 Modal identification using FDD technique (W.N.2)

Table 3-2 Modal identification results (W.N.2)

Mode #	f_i	ζ_i	Mode Shape				
			ϕ_{1i}	ϕ_{2i}	ϕ_{3i}	ϕ_{4i}	ϕ_{5i}
1	2.326	5.43%	-0.648	-0.535	-0.412	-0.299	-0.183
2	3.368	3.15%	-0.370	-0.173	0.277	0.497	0.714
3	12.281	0.78%	-0.399	0.410	0.621	0.377	-0.381

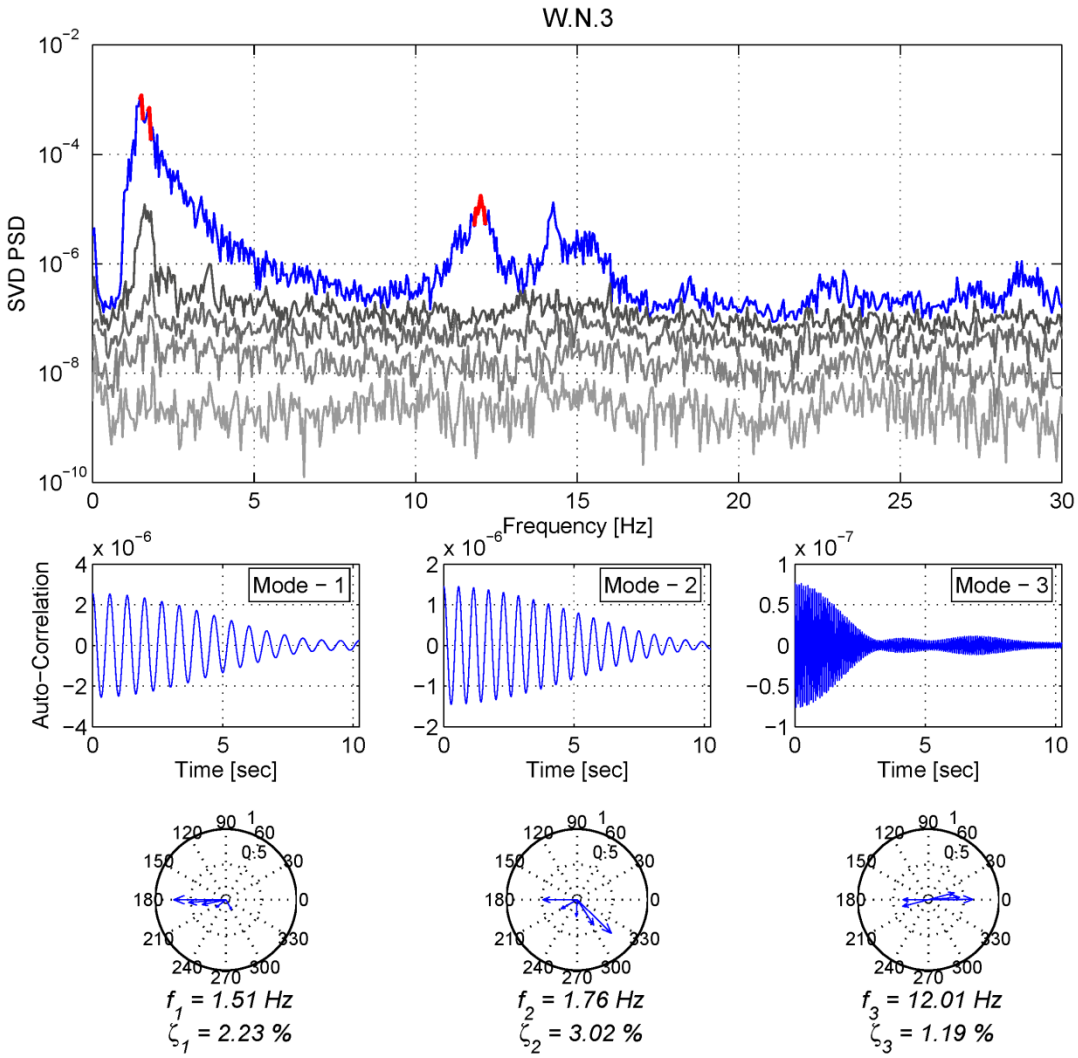

Figure 3–4 Modal identification using FDD technique (W.N.3)

Table 3-3 Modal identification results (W.N.3)

Mode #	f_i	ζ_i	Mode Shape				
			ϕ_{1i}	ϕ_{2i}	ϕ_{3i}	ϕ_{4i}	ϕ_{5i}
1	1.493	2.23%	-0.739	-0.529	-0.342	-0.179	0.160
2	1.717	3.02%	-0.483	-0.259	-0.238	0.429	0.678
3	12.019	1.19%	-0.359	0.443	0.627	0.378	-0.374

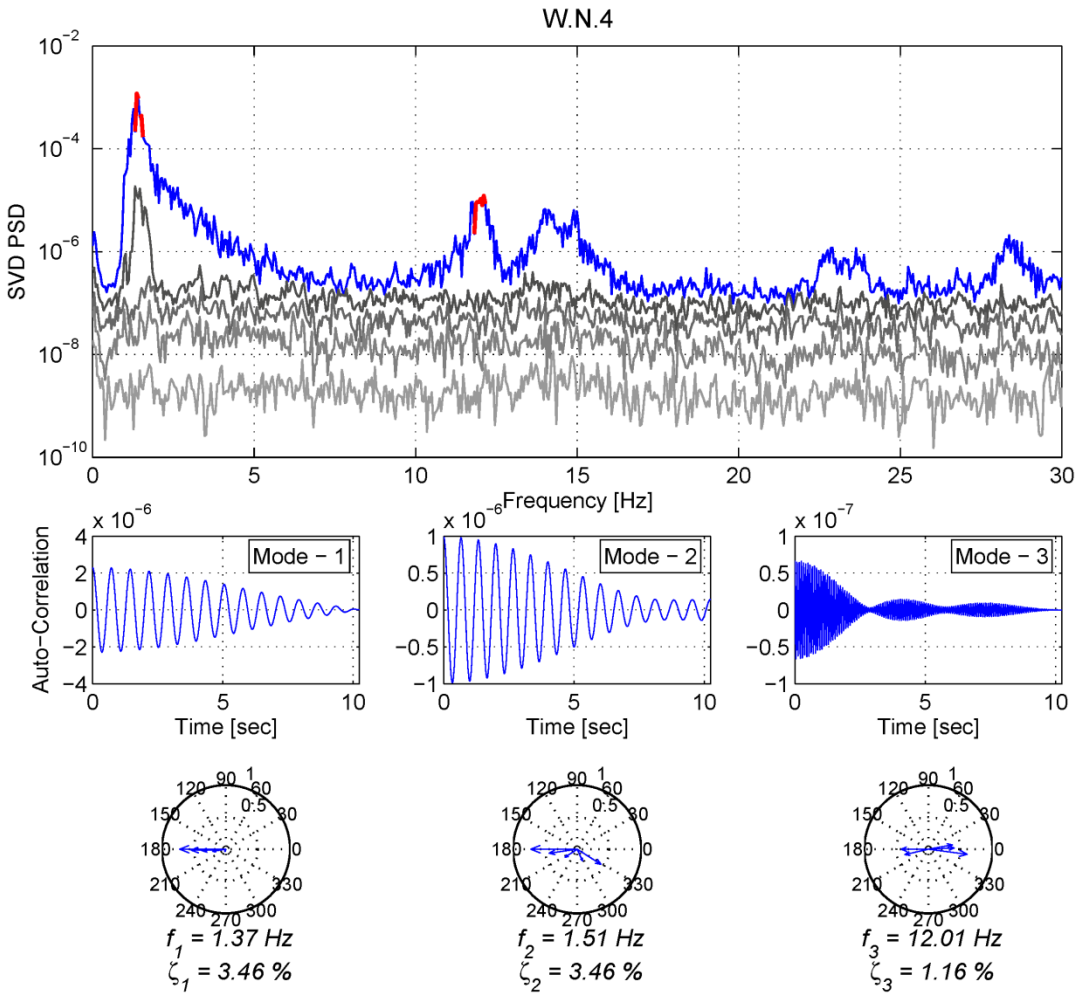

Figure 3–5 Modal identification using FDD technique (W.N.4)

Table 3-4 Modal identification results (W.N.4)

Mode #	f_i	ζ_i	Mode Shape				
			ϕ_{1i}	ϕ_{2i}	ϕ_{3i}	ϕ_{4i}	ϕ_{5i}
1	1.394	3.45%	-0.721	-0.542	-0.376	-0.210	-0.041
2	1.468	3.46%	-0.722	-0.440	-0.227	0.199	0.441
3	12.025	1.19%	-0.424	0.402	0.611	0.380	-0.376

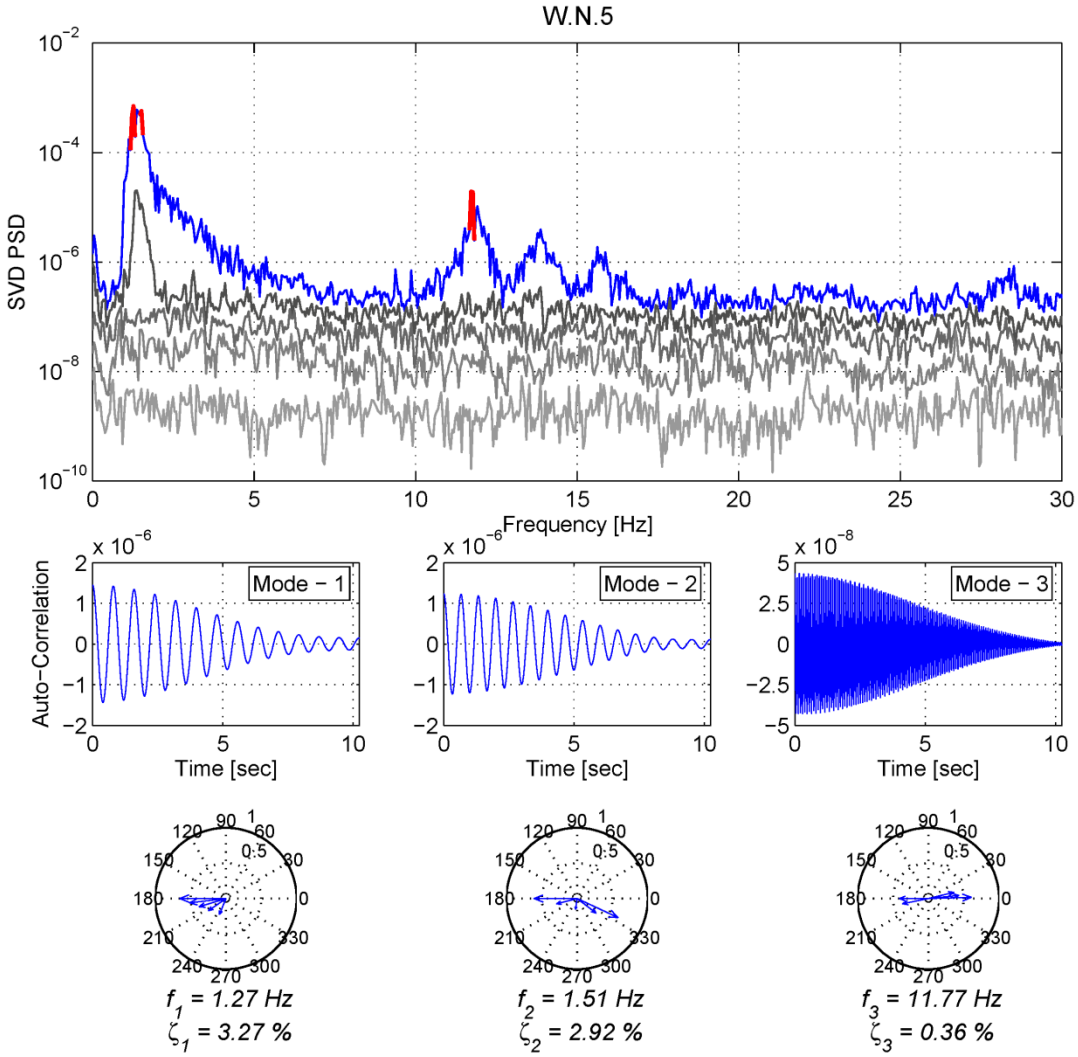

Figure 3–6 Modal identification using FDD technique (W.N.5)

Table 3-5 Modal identification results (W.N.5)

Mode #	f_i	ζ_i	Mode Shape				
			ϕ_{1i}	ϕ_{2i}	ϕ_{3i}	ϕ_{4i}	ϕ_{5i}
1	1.268	3.27%	-0.653	-0.519	-0.396	-0.299	-0.241
2	1.484	2.91%	-0.608	-0.299	-0.151	0.336	0.637
3	11.712	0.66%	-0.410	0.433	0.607	0.371	-0.372

3.3 Modal Identification From High-Amplitude Earthquake Excitations

Many of the vibration-based structural health monitoring techniques are based on the comparison of the dynamic characteristics of the structures (modal frequencies, damping ratios and mode shapes) before and after occurrence of damage. During damaging events, such as high amplitude earthquakes, structures normally exhibit nonlinear dynamic behavior with gradual or abrupt changes in the stiffness and damping properties of structural elements which result in time-varying dynamic characteristics over such events. As a result, conventional modal identification procedures are not applicable for the analysis of the structural response to such events due to violation of their basic assumptions. In this study, a three step procedure is proposed for the analysis of nonlinear and non-stationary responses of the structures during high amplitude earthquake excitations. Discrete state space models are used to describe the relationship between the input, noise and output signals of the structural systems during earthquake excitations. Two well known parameter estimation techniques are applied for estimation of state space model parameters from input and output measurements. In the following subsections, theoretical backgrounds and details of state space models, adopted parameters estimation methods named as prediction error and stochastic subspace identification methods are presented.

3.3.1 System Identification Approach

3.3.1.1 State Space Models

State-space models are mathematical models that use state variables to describe a dynamical system by a set of first-order differential or difference equations. State variables can be reconstructed from the measured input-output or output-only data, but are not themselves

measured during an experiment. A linear time-invariant system can be described by a discrete-time state-space model as:

$$\begin{aligned} x(t+1) &= \mathbf{A}\,x(t) + \mathbf{B}\,u(t) + w(t) \\ y(t) &= \mathbf{C}\,x(t) + \mathbf{D}\,u(t) + v(t) \end{aligned} \tag{3-11}$$

Where the vectors, $u(t) \in \mathbf{R}^{m\times 1}$ and $y(t) \in \mathbf{R}^{p\times 1}$ are measured inputs and outputs of the system at time instant t. The order of the system and the dimension of the state vector, $x(t) \in \mathbf{R}^{n\times 1}$, is n; $\mathbf{A} \in \mathrm{R}^{n\times n}$ is the matrix that completely characterizes the global dynamics of the system by its eigenvalues. $\mathbf{B} \in \mathrm{R}^{n\times m}$ is the input matrix. $\mathbf{C} \in \mathrm{R}^{p\times n}$ is the output matrix that correlates the internal states of the state space model with the real system physical parameters and $\mathbf{D} \in \mathrm{R}^{p\times m}$ is the direct feed through matrix. $w(t) \in \mathbf{R}^{n\times 1}$ and $v(t) \in \mathbf{R}^{p\times 1}$, are immeasurable noise vector sequences called process and measurement noise respectively. The noise vectors are assumed to be zero-mean, white and stationary signals. The state space model identification problem can be described as identification of system matrices and noise characteristics using a relatively large number of measured inputs and outputs of the system. Numerous methods have been developed and applied for identification of state space model matrices. In this study, performances of two model parameter estimation approaches are investigated: (1) prediction-error methods (2) subspace methods. Brief reviews of these methods are presented in the following section.

3.3.1.2 State Space Model Parameters Estimation Methods

<u>Prediction-Error Parameter Estimation Methods</u>

Prediction-error methods (PEMs) are a broad family of model parameter estimation methods that can be applied to different modeling structures. The PEM provides a number of advantages over other model parameter estimation techniques such as (1) Model structure flexibility: it could be applied for parameter estimation of a wide spectrum of model structures. (2) Excellent

asymptotic properties, do to its kinship with maximum likelihood (3) ability to handle systems in closed loop (the input is partly determined as output feedback, when data are collected). It also has some drawbacks like (1) it requires an explicit parameterization of the model (2) The search for the parameters that gives the best output prediction fit may be laborious and involve search surfaces that have many local minima[52]. A brief review of the theoretical background of PEM is presented as follows: Let $Z^N = \{u(1), y(1), u(2), y(2), ..., u(N), y(N)\}$ collect all the past data measured up to time N. The basic idea behind prediction error approach is very simple. Describe the model as a predictor of the next output:

$$\hat{y}_m(t \mid t-1) = f(Z^{t-1}) \tag{3-12}$$

Here $\hat{y}_m(t \mid t-1)$ denotes the one-step ahead prediction of the output and f is and arbitrary function of past observed data. Parameterize the predictor in terms of a finite-dimensional parameter vector θ:

$$\hat{y}(t \mid \theta) = f(Z^{t-1}, \theta) \tag{3-13}$$

Determine an estimate of parameter vector, $\hat{\theta}$, from the model parameterization and observed data set Z^N so that the distance between response prediction vector $\{\hat{y}(1 \mid \theta), ..., \hat{y}(N \mid \theta)\}$ and measurements vector $\{y(1), ..., y(N)\}$ is minimized in suitable norm. The prediction error of a certain model parameterized with θ_* is given by:

$$\varepsilon(t, \theta_*) = y(t) - \hat{y}(t \mid \theta) \tag{3-14}$$

When the data set Z^N is known, these errors can be computed for $t = 1, 2, \ldots N$. We are interested in finding model parameters that can minimize the error for all of observed data. Now, let the prediction error sequence be filtered through a stable linear filter $L(q)$:

$$\varepsilon_F(t,\theta) = L(q)\varepsilon(t,\theta) \tag{3-15}$$

Applying the filter $L(\cdot)$ allows extra freedom in dealing with non-momentary properties of the prediction error like high-frequency disturbances which are not essential to the modeling problem. Now let define the following norm:

$$V_N(\theta, Z^N) = \frac{1}{N}\sum_{t=1}^{N} l(\varepsilon_F(t,\theta)) \tag{3-16}$$

Where $l(\cdot)$ is a scalar-valued (typically positive) function. The function $V_N(\theta, Z^N)$ is a natural measure of the validity of the selected model. Now the model parameter estimate, $\hat{\theta}$, is found by minimization of the norm function:

$$\hat{\theta}_N = \hat{\theta}_N(Z^N) = \arg\min_{\theta \in D_M} V_N(\theta, Z^N) \tag{3-17}$$

As stated earlier, prediction error identification methods refer to a broad family of identification approaches. Different versions of the method can be achieved by changing the choice of $l(\cdot)$, the choice of filter $L(\cdot)$, choice of model structure and even choice of minimization method that is used for finding $\hat{\theta}$. In this study, the PEM function provided within Matlab system identification package is utilized for state space model parameter identification. The following error norm is utilized in definition of $V_N(\theta, Z^N)$:

$$l(\varepsilon) = \det(\varepsilon^T \times \varepsilon) \tag{3-18}$$

The frequency weighting function, $L(\cdot)$, is calculated as the product of the input spectrum and the inverse of the noise model. As a result, higher weights are assigned to frequencies excited by the input signal and lower weights are used for frequencies in the noise range.

Stochastic Subspace System Identification Method

Stochastic subspace identification methods are well-established family of identification methods that take advantage of robust techniques such QR factorization and singular value decomposition (SVD) to estimate the model order , n , and system matrices A , B , C and D matrices in a state space model. Details of determination of system matrices and initial states are presented[53].

It is well known that the state space model input-output relationship presented in equation (3-11) can also be described by:

$$\begin{aligned} \tilde{x}(t+1) &= T^{-1}A\tilde{x}(t+1) + T^{-1}Bu(t) + \tilde{w}(t) \\ y(t) &= CT\tilde{x}(t) + Du(t) + v(t) \end{aligned} \tag{3-19}$$

For any invertible matrix T . This corresponds to change of basis $\tilde{x}(t) = T^{-1}x(t)$ in the state space. Subspace algorithms are based on the following observations:

- If $\hat{A}$ and $\hat{C}$ are known, it is an easy linear least squares problem to estimate $\hat{B}$ and $\hat{D}$

$$y(t) = \hat{C}(qI - \hat{A})^{-1}Bu(t) + Du(t) \tag{3-20}$$

  Using the predictor:

$$\hat{y}(t \mid B, D) = \hat{C}(qI - \hat{A})^{-1}Bu(t) + Du(t) \tag{3-21}$$

  (The initial state $x(0)$ can also be estimated)

- If the observability matrix, O_r , of the system is known, then it is easy to determine C and A . Use the first block row of O_r and the shift property respectively.

$$O_r = \begin{bmatrix} C \\ CA \\ \vdots \\ CA^{r-1} \end{bmatrix} \tag{3-22}$$

- The extended observability matrix can be consistently estimated from input-output data by direct least-squares like steps.

- Once the observability matrix has been estimated, the states $x(t)$ can be constructed and the statistical properties of the noise contributions $w(t)$ and $v(t)$ can be established.

<u>*Estimating the Extended Observability Matrix*</u>

Using state space model ,(3-11), we find that:

$$\begin{aligned}
y(t+k) &= Cx(t+k) + Du(t+k) + v(t+k) \\
y(t+k) &= C[Ax(t+k-1) + Bu(t+k-1) + w(t+k-1)] + Du(t+k) + v(t+k) \\
&\vdots \\
y(t+k) &= CA^k x(t) + CA^{k-1}Bu(t) + CA^{k-2}Bu(t+1) + \cdots \\
&\quad + CBu(t+k-1) + Du(t+k) \\
&\quad + CA^{k-1}w(t) + CA^{k-2}W(t+1) + \cdots \\
&\quad + Cw(t+k-1) + v(t+k)
\end{aligned} \tag{3-23}$$

Now, form the vectors

$$Y_r(t) = \begin{bmatrix} y(t) \\ y(t+1) \\ \vdots \\ y(t+r-1) \end{bmatrix}, \qquad U_r(t) = \begin{bmatrix} u(t) \\ u(t+1) \\ \vdots \\ u(t+r-1) \end{bmatrix} \tag{3-24}$$

and rewrite (3-23) as

$$Y_r(t) = O_r x(t) + S_r Y_r(t) + V(t) \tag{3-25}$$

$$S_r = \begin{bmatrix} D & 0 & \cdots & 0 & 0 \\ CB & D & \cdots & 0 & 0 \\ \vdots & \vdots & \ddots & \vdots & \vdots \\ CA^{r-2}B & CA^{r-3}B & \cdots & CB & D \end{bmatrix} \tag{3-26}$$

and the k th block component of $V(t)$

$$\begin{aligned}
V_k(t) &= CA^{k-2}w(t) + CA^{k-3}w(t+1) + \cdots \\
&\quad + Cw(t+k-2) + v(t+k-1)
\end{aligned} \tag{3-27}$$

In order to estimate O_r using measured input and output signals, now let's define the following matrices:

$$
\begin{aligned}
\mathbf{Y} &= [Y_r(1) \quad Y_r(2) \cdots Y_r(N)] \\
\mathbf{X} &= [x\ (1) \quad x\ (2) \cdots x\ (N)] \\
\mathbf{U} &= [U_r(1) \quad U_r(2) \cdots U_r(N)] \\
\mathbf{V} &= [V\ (1) \quad V\ (2) \cdots V\ (N)]
\end{aligned}
\tag{3-28}
$$

Where N is the number of recorded data points. Using the above definitions equation (3-25) can be written in following format:

$$\mathbf{Y} = O_r\mathbf{X} + S_r\mathbf{U} + \mathbf{V} \tag{3-29}$$

Now, consider the problem of obtaining an estimate of O_r in (3-29), with knowledge of data matrices $\mathbf{Y}$ and $\mathbf{U}$. If the impulse response matrix S_r was known, we could simply subtract the $S_r\mathbf{U}$ term from $\mathbf{Y}$ and apply SVD for extraction of O_r. An unstructured least square estimate

$$\min_{S_r} \left\| \mathbf{Y} - S_r\mathbf{U} \right\|_F^2 \tag{3-30}$$

Where $\|\cdot\|_F$ denotes the Frobenius norm, leads to the matrix

$$\mathbf{Y} - \hat{S}_r\mathbf{U} = \mathbf{Y}\Pi_{U^T}^{\perp} \tag{3-31}$$

Where $\Pi_{U^T}^{\perp}$ is the orthogonal projection onto the null space of $\mathbf{U}$:

$$\Pi_{U^T}^{\perp} = \mathbf{I} - \mathbf{U}^T(\mathbf{U}\mathbf{U}^T)^{-1}\mathbf{U} \tag{3-32}$$

The indicated inverse exists if the input is persistently exciting and $N > mr$ since

$$\mathbf{U}\Pi_{U^T}^{\perp} = 0 \tag{3-33}$$

We have in effect removed the part of the output $y(t)$ that did not originate from the state $x(t)$. The remaining part is

$$\mathbf{Y}\Pi_{U^T}^{\perp} = O_r\mathbf{X}\Pi_{U^T}^{\perp} + V\Pi_{U^T}^{\perp} \tag{3-34}$$

The next problem is to eliminate the last term. Since this term is made up of noise contributions, the idea is to correlate it away with a suitable matrix. Define the $s \times N$ matrix ($s \geq N$).

$$\Phi = [\varphi_s(1) \quad \varphi_s(1) \quad \cdots \quad \varphi_s(N)] \tag{3-35}$$

Here $\varphi_s(t)$ is a yet undefined vector. Multiply (3-34) from the right by Φ^T and normalize by N

$$G = \frac{1}{N}\mathbf{Y}\Pi_{U^T}^{\perp}\Phi^T = O_r\frac{1}{N}\mathbf{X}\Pi_{U^T}^{\perp}\Phi^T + \frac{1}{N}\mathbf{V}\Pi_{U^T}^{\perp}\Phi^T \square O_r\tilde{T}_N + V_N \tag{3-36}$$

Here $\tilde{T}_N$ is an $n \times s$ matrix. Suppose now that we can find $\varphi_s(t)$ so that:

$$\lim_{N\to\infty} V_N = \lim_{N\to\infty}\frac{1}{N}\mathbf{V}\Pi_{U^T}^{\perp}\Phi^T = 0 \tag{3-37}$$

$$\lim_{N\to\infty} \tilde{T}_N = \lim_{N\to\infty}\frac{1}{N}\Pi_{U^T}^{\perp}\Phi^T = \tilde{T} \tag{3-38}$$

Then (3-36) becomes:

$$G = \frac{1}{N}\mathbf{Y}\Pi_{U^T}^{\perp}\Phi^T = O_r\tilde{T}_N + E_N \tag{3-39}$$

$$E_N = O_r(\tilde{T}_N - \tilde{T}) + V_N \to 0 \quad as \quad N \to \infty \tag{3-40}$$

The $pr \times s$ matrix G can thus be seen as a noisy estimate that can be used to obtain estimates of A and C. The only remaining question is how to achieve (3-37) and (3-38). Using the expression (3-32) for $\Pi_{U^T}^{\perp}$ and writing out the matrix multiplications as sums gives

$$\begin{aligned}\frac{1}{N}\mathbf{V}\Pi_{U^T}^{\perp}\Phi^T = &\frac{1}{N}\sum_{t=1}^{N}V(t)\varphi_s^T(t) - \frac{1}{N}\sum_{t=1}^{N}V(t)U_r^T(t) \\ &\times\left[\frac{1}{N}\sum_{t=1}^{N}U_r(t)U_r^T(t)\right]^{-1} \times \frac{1}{N}\sum_{t=1}^{N}U_r(t)\varphi_s^T(t)\end{aligned} \tag{3-41}$$

Under mild conditions, the law of large numbers states that the sample sums converge to their respective expected values:

$$\lim_{N\to\infty}\frac{1}{N}\mathbf{V}\Pi^{\perp}_{U^T}\Phi^T = \bar{E}(V(t)\varphi_s^T(t)) - \bar{E}(V(t)U_r^T(t))R_u^{-1}\bar{E}(U_r^T(t)\varphi_s^T(t))$$
$$R_u = \bar{E}(U_r(t)U_r^T(t)) \tag{3-42}$$

Here R_u is the $r\times r$ covariance matrix of the input. Now assume that the input u is independent of the noise term V. Then $E(V(t)U_r^T(t))=0$. Assume also that R_u is invertible which means that the input is persistently exciting of order r. Then the second term of (3-42) will be zero. For the first term to be zero, we must require $V(t)$ and $\varphi_s(t)$ to be uncorrelated. Since $V(t)$ is made up of white noise terms from time t and onwards, any choice $\varphi_s(t)$ built up from data prior to time t will satisfy (3-42). A typical choice would be

$$\varphi_s(t) = \begin{bmatrix} y(t-1) \\ \vdots \\ y(t-s_1) \\ u(t-1) \\ \vdots \\ u(t-s_2) \end{bmatrix} \tag{3-43}$$

Summing up, forming $G = \frac{1}{N}\mathbf{Y}\Pi^{L}_{U^T}\Phi^T$ with Φ defined by (3-43) and (3-35) gives the properties of (3-39) and (3-40) which allows us to consistently determine A and C as presented in the following subsection.

<u>*Estimation of A and C from extended observability matrix*</u>

Suppose that a $pr\times n^*$ dimensional matrix G is given, that is related to the extended observability matrix of the system,(3-22). We have to determine A and C from G. In the case of known system order, C can easily be found as the first p rows of O_r:

$$\hat{C} = O_r(1:p,1:n) \tag{3-44}$$

Similarly, $\hat{A}$ can be found from the following equation:

$$O_r(p+1:pr,1:n) = O_r(1:p(r-1),1:n)\hat{A} \tag{3-45}$$

Which is easily seen from definition of O_r. Under the assumption of observability, O_{r-1} has rank n, so $\hat{A}$ can be determined uniquely. Note that the extended observability matrix depends on the choice of basis in the state space representation. It is easy to verify that the observability matrix would be:

$$\tilde{O}_r = O_r T \tag{3-46}$$

Applying (3-44) and (3-45) to $\tilde{O}_r$ would thus give the system matrices associated with (3-19). Consequently, multiplying the extended observability matrix from the right by any invertible matrix before applying (3-44) and (3-45) will not change the system estimate.

Now, suppose that the order of the system is unknown and that n^* - the number of columns of G - is just an upper bound for the order. This means that we have:

$$G = O_r \tilde{T} \tag{3-47}$$

For some unknown but full rank, $n \times n^*$ matrix $\tilde{T}$, where also n is unknown to us. The rank of G is n. The straightforward way to deal with this would be determine this rank, delete the last $n^* - n$ columns of G and then proceed as above. A more general and numerically sound way of reducing the column space is to use singular value decomposition (SVD):

$$G = USV^T = U\begin{bmatrix} \sigma_1 & 0 & 0 & \cdots & 0 \\ 0 & \sigma_2 & 0 & \cdots & 0 \\ 0 & 0 & \sigma_3 & \cdots & 0 \\ \vdots & \vdots & \vdots & \ddots & \vdots \\ 0 & 0 & 0 & \cdots & \sigma_{n^*} \\ 0 & 0 & 0 & \cdots & 0 \\ \vdots & \vdots & \vdots & \cdots & \vdots \\ 0 & 0 & 0 & \cdots & 0 \end{bmatrix} V^T \tag{3-48}$$

Here U and V are orthonormal matrices ($U^T U = I$, $V^T V = I$) of dimensions $pr \times pr$ and $n^* \times n^*$ respectively. S is a $pr \times n^*$ matrix with singular values of G along the diagonal and zeros elsewhere. If G has rank n, only the first n singular values σ_k will be non-zero. This means that we can rewrite

$$G = USV^T = U_1 S_1 V_1^T \tag{3-49}$$

Where U_1 is a $pr \times n$ matrix containing the first n columns of U, while S_1 is the $n \times n$ upper left part of S, and V_1 consists of the first n columns of V ($V_1^T V_1 = I$ still remains valid). From (3-47) and (3-49), and by multiplying V_1 from the right we will have:

$$O_r \tilde{T} V_1 = O_r T = U_1 S_1 \tag{3-50}$$

For some invertible matrix $T = \tilde{T} V_1$. We are now in the situation (3-46) that we know the observability matrix up to an invertible matrix T or we know the observability matrix in some state space basis. Consequently we can use $\hat{O}_r = U_1 S_1$ or $\hat{O}_r = U_1$ or any matrix that can be written as:

$$\hat{O}_r = U_1 R \tag{3-51}$$

for some invertible R in (3-44) and (3-45).

Let us now assume that the given $pr \times n^*$ matrix is a noisy estimate of the true observability matrix

$$G = O_r \tilde{T} + E_N \tag{3-52}$$

Where E_N is small and tends to zero as $N \to \infty$. The rank of O_r is not known, while the noise matrix E_N is likely to be of full rank. It is reasonable to proceed as above and perform an SVD on G:

$$G = USV^T \tag{3-53}$$

Due to the noise, S will have all singular values $\sigma_k : k = 1, \ldots, min(n^*, pr)$ non-zero. The first n will be supported by O_r, while the remaining ones stem from E_N. If the noise is small, one should expect that the latter are significantly smaller than the former. Therefore determine the $\hat{n}$ as the number of singular values which are significantly larger than zero. Then keep those and replace others in S by zero and proceed as the mentioned above to determine S_1 and U_1.

<u>*Using Weighting Matrices in the SVD*</u>

For more flexibility we could pre- and post- multiply G as $\hat{G} = W_1 G W_2$ before performing SVD.

$$\hat{G} = W_1 G W_2 = USV^T \approx U_1 S_1 V_1^T \tag{3-54}$$

and then instead of (3-51) use

$$\hat{O}_r = W_1^{-1} U_1 R \tag{3-55}$$

to determine the $\hat{C}$ and $\hat{A}$. Here R is an arbitrary matrix that will determine the coordinate basis for the state representation. The post multiplication by W_2 just corresponds to change of

basis in the state space and the pre- multiplication by W_1 is eliminated in (3-55) so in the noiseless case these weightings are without consequence. However when noise is present, they have an important influence on the space spanned by U_1 and on the quality of the estimates $\hat{C}$ and $\hat{A}$.

<u>*Estimation of B and D Matrices*</u>

For given $\hat{A}$ and $\hat{C}$ model structure:

$$\hat{y}(t \mid B, D) = \hat{C}(qI - \hat{A})^{-1} Bu(t) + Du(t) \tag{3-56}$$

is clearly linear in B and D. The predictor is also formed entirely from past inputs, so it is an output error model structure. The predictor can be written in standard linear regression form:

$$\hat{y}(t) = \varphi(t)\theta = \varphi(t)\begin{bmatrix} Vec(B) \\ Vec(D) \end{bmatrix} \tag{3-57}$$

With a $p \times (mn + mp)$ matrix $\varphi(t)$. Here $Vec(\cdot)$ is the operation that builds a vector from a matrix, by stacking its columns on top of each other. Let $r = (k-1)n + j$. To find the rth column of $\varphi(t)$ which corresponds to r^{th} element of model parameters ,θ, we differentiate the above equation with respect to this element and obtain:

$$\varphi_r(t) = \hat{C}(qI - \hat{A})^{-1} E_j u_k(t) \tag{3-58}$$

Where E_j is the column vector with the jth element equal to 1 and the others equal to 0. The rows for $r > nm$ are handled in similar way. If desired the initial state $x_0 = x(0)$ can be estimated in an analogous way:

$$\hat{y}(t \mid B, D, x_0) = \hat{C}(qI - \hat{A})^{-1} x_0 \delta(t) + \hat{C}(qI - \hat{A})^{-1} Bu(t) + Du(t) \tag{3-59}$$

Which is linear also in x_0. Here $\delta(t)$ is the unit impulse at time 0.

Summary of Subspace-based Methods

The complete subspace algorithm can be summarized as follows:

1. From the input-output data, form

$$G = \frac{1}{N}\mathbf{Y}\Pi_{U^T}^{\perp}\Phi^T \tag{3-60}$$

with the involved matrices defined by equations (3-28), (3-24), (3-32) and (3-43). In construction of Φ, assumption of $s_1 = s_2$ is common.

2. Select weighting matrices W_1 ($rp \times rp$ and invertible) and W_2 ($(ps_1 + ms_2) \times \alpha$)) and perform SVD:

$$\hat{G} = W_1 G W_2 = USV^T \approx U_1 S_1 V_1^T \tag{3-61}$$

Where the last approximation is obtained by keeping the n most significant values of the singular values in S and setting the remaining ones to zero.(U_1 is now $rp \times n$ S_1 is $n \times n$ and V_1^T is $n \times \alpha$).

3. Select a full rank matrix R and define the $rp \times n$ matrix $\hat{O}_r = W_1^{-1} U_1 R$. Typical choices for R are $R = I$, $R = S_1$ or $R = S_1^{1/2}$. Solve

$$\hat{C} = O_r(1:p, 1:n) \tag{3-62}$$

$$O_r(p+1:pr, 1:n) = O_r(1:p(r-1), 1:n)\hat{A} \tag{3-63}$$

For $\hat{C}$ and $\hat{A}$. The latter equation should be solved in a least square sense.

4. Estimate $\hat{B}$ and $\hat{D}$ and $\hat{x}_0$ from the linear regression problem:

$$\min_{B,D,x_0} \frac{1}{N}\sum_{t=1}^{N}\left\| y(t) - \hat{C}(qI - \hat{A})^{-1}Bu(t) - Du(t) - \hat{C}(qI - \hat{A})^{-1}x_0\delta(t) \right\| \tag{3-64}$$

The subspace family of methods contains a number of design variables. Different algorithms described in the literature correspond to different choices of these variables and it is still not fully understood how to choose them optimally. The design variables of this family of methods include (1) the correlation vector $\varphi_s(t)$ (2) the scalar r which is the maximal prediction horizon used (3) the weighting matrices W_1 and W_2 (4) matrix R in step 3 of the procedure.

In this study, N4SID routine of system identification toolbox of Matlab software package is utilized. The routine takes advantage of Akaike Information Criterion for the selection of r, s_1 and s_2 design variables. The weighting matrices as proposed by Verhaegen[54] and implemented in Multivariable Output-Error State Space (MOESP) class of algorithms are calculated as:

$$W_1 = I\,, \qquad W_2 = (\frac{1}{N}\Phi\Pi_{U^T}^{\perp}\Phi^T)^{-1}\Phi\Pi_{U^T}^{\perp} \tag{3-65}$$

Once the system matrices of the state space models are calculated modal properties of the structure including modal frequencies, damping ratios and mode shapes can easily be found. Details of extraction of modal properties from state space model matrices are presented in the following section:

3.3.1.3 Extraction of Modal Data from System Matrices

As stated earlier, matrix A of a state space model controls the dynamic properties of the system by its eigenvalues. Eigenvalue decomposition of state matrix (A) is represented in the form of

$$A = \Psi\Lambda\Psi^{-1} \tag{3-66}$$

Where Ψ and Λ are eigenvector and eigenvalue matrices, respectively. The modal properties of a continuous-time system can be derived from the following equations:

$$\Lambda = diag(\overline{\eta}_i \pm j\overline{\mu}_i) \tag{3-67}$$

$$\overline{\eta}_i \pm j\overline{\mu}_i = f_s(\ln(\overline{\eta}_i) \pm j\ln(\overline{\mu}_i)) \tag{3-68}$$

$$\omega_i = \sqrt{\eta_i^2 + \mu_i^2} \tag{3-69}$$

$$\zeta_i = -cos(tan^{-1}(\frac{\mu_i}{\eta_i})) \tag{3-70}$$

$$\phi_i = C\Psi_i \tag{3-71}$$

Where f_s is the sampling frequency and ω_i, ζ_i and ϕ_i represent natural frequency, damping ratio and the mode shape of the ith mode of vibration of the structure. Through the use of stability diagrams, the physical modal properties of the structure can be accurately identified and distinguished from the spurious ones generated due to the process and measurement noises.

3.3.2 Modal Identification Methodology

Presented system identification approaches are utilized within a modal identification framework for identification of post-earthquake modal properties from nonlinear responses of the structure to high amplitude earthquake excitations. As displayed in figure 3–7, the procedure has three main steps: (1) Time-frequency analysis of the nonlinear response (2) Identification of stable segments of the response (3) modal identification from identified stable segments. Details of each step are discussed in following subsections

3.3.2.1 Step-1: Time-Frequency Analysis

In order to study the nonlinear behavior of the bridge during damaging earthquake excitations, time-frequency relationships are derived from the measured acceleration responses. Time-dependent modal properties of the structure are estimated by identifying low-order ($n = 20$) state space model parameters from successive and overlapping short time-windows of the response.

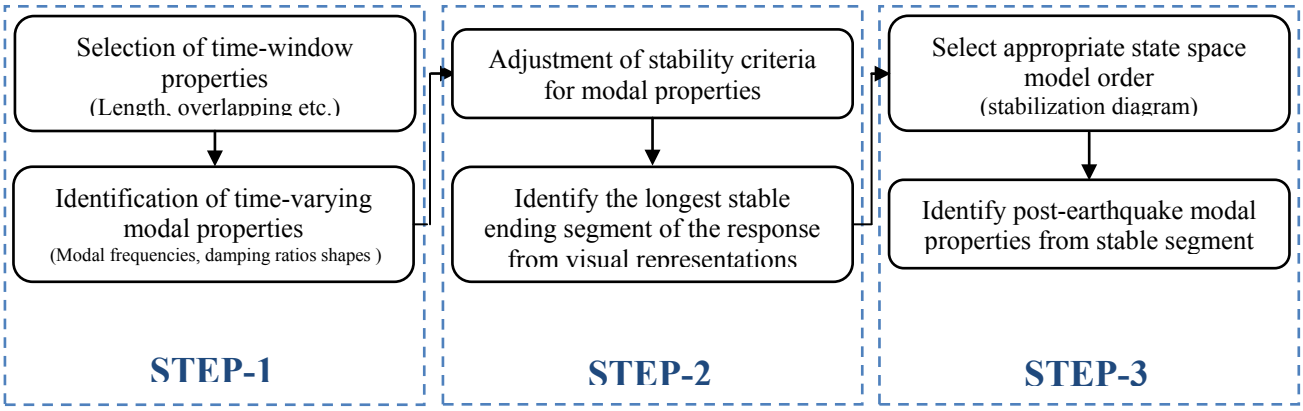

Figure 3–7 Modal identification methodology

During each time-window, bridge system is approximated as a linear and time-invariant system. Performances of presented system identification approaches (prediction-error method and subspace-based method) in model parameter estimation from such short segments of the response are investigated and compared. The critical quantity in time-frequency decomposition is the duration of the segments: while short segments may lead to inaccurate and unreliable modal properties, long segments may not provide sufficient time resolution to adequately capture the evolution of dynamic properties of the system [22]. Thus, a compromise between achievable accuracy and time resolution is necessary. In order to study the sensitivity of the system identification methods to the length of the signal, two windows of 300-data -points and 600-data-points length are utilized. The windows are shifted by 50-data-point increments over the measured signals. In order to evaluate and compare the model fitting results using different system identification approaches and window lengths, a measure of fit between model simulation results and bridge response measurements is adopted:

$$fit = 100 \times \left[1 - \frac{norm(\hat{y}(t) - y(t))}{norm(y(t) - mean(y(t)))} \right] \tag{3-72}$$

Here, $y(t)$ and $\hat{y}(t)$ denote output measurement and simulation results and $norm(\cdot)$ operator returns the Euclidean length of the vector.

3.3.2.2 Step-2: Identification of Stable Segment of Response

The time-frequency decomposition of the bridge response measurements obtained in the previous step is utilized for identification of the longest segment of the response with stable modal properties. The errors between the modal properties identified from successive time-windows of the response are used to determine the stability status of the dynamic characteristics between the center times of the windows. Three stability criteria are defined as the maximum acceptable errors between natural frequencies, damping ratios and modal shapes identified from successive windows. Applied stability criteria for the frequencies, damping ratios and mode shapes of significant modes of vibration are presented in equations (3-73) through (3-75):

$$max\left(\left|\frac{f_j^i - f_j^{i-1}}{f_j^i}\right|, \left|\frac{f_j^i - f_j^{i+1}}{f_i}\right|\right) \leq 0.01 \tag{3-73}$$

$$max\left(\left|\frac{\zeta_j^i - \zeta_j^{i-1}}{\zeta_j^i}\right|, \left|\frac{\zeta_j^i - \zeta_j^{i+1}}{\zeta_j^i}\right|\right) \leq 0.05 \tag{3-74}$$

$$max\left(\left[1 - MAC\left(\phi_j^i, \phi_j^{i-1}\right)\right], \left[1 - MAC\left(\phi_j^i, \phi_j^{i+1}\right)\right]\right) \leq 0.03 \tag{3-75}$$

In above equations, superscripts denote the time window sequence number while subscripts represent the number of the identified mode. In order to visualize the stability status of modal properties corresponding to each window, different visual styles are used for different stability levels:

- (+) for stable frequency
- (×) for stable frequency and damping
- (⊗) for stable frequency and mode shape

- (⊕) for stable frequency, damping and mode shape

Results of time-frequency analysis of the response of the bridge to white noise and earthquake excitations for the case of subspace identification from 600-data-point windows are presented in figure 3–8 through figure 3–18. In each of these figures, the time-history plot at the top demonstrates the acceleration response measurement at channel#1 (located at top of Bent-1). The bottom plot shows the identified time-dependent modal properties overlaid the contour plot of short-time Fourier transform of the response at channel#1. Identified stable segments of the response are marked with black double-arrows.

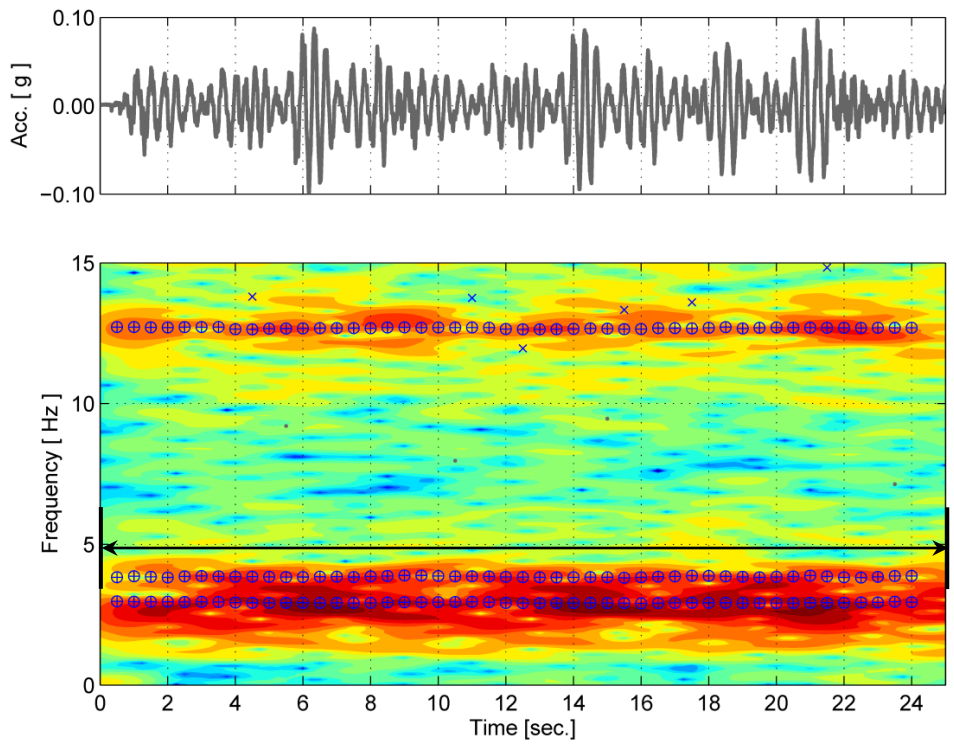

Figure 3–8 Time-dependent modal properties (WN-1)

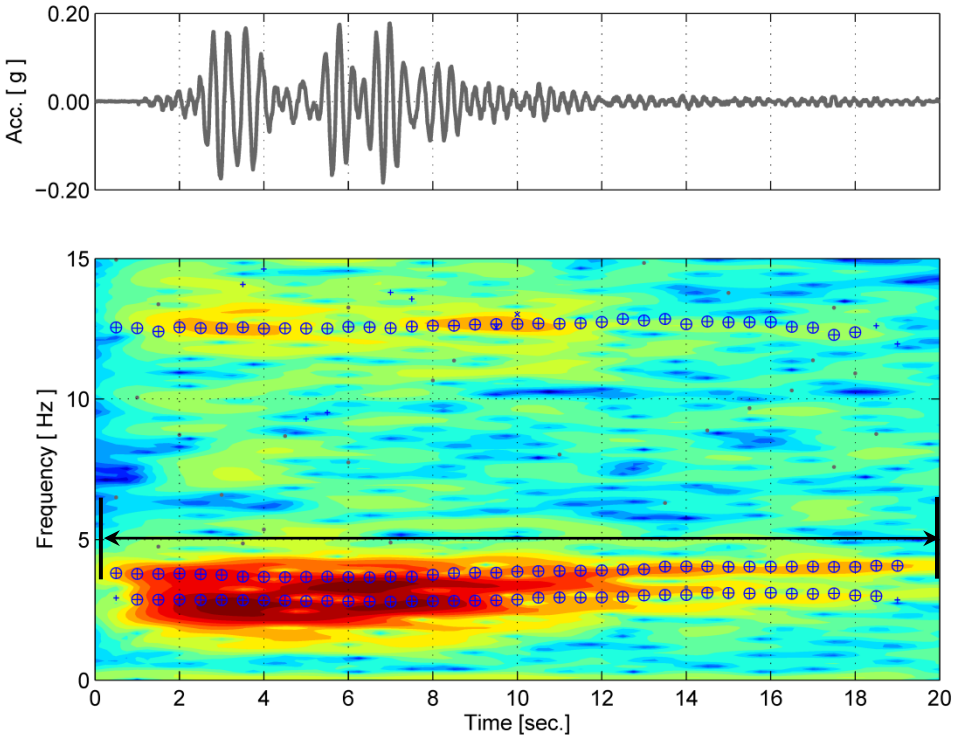

Figure 3–9 Time-dependent modal properties (Test-12)

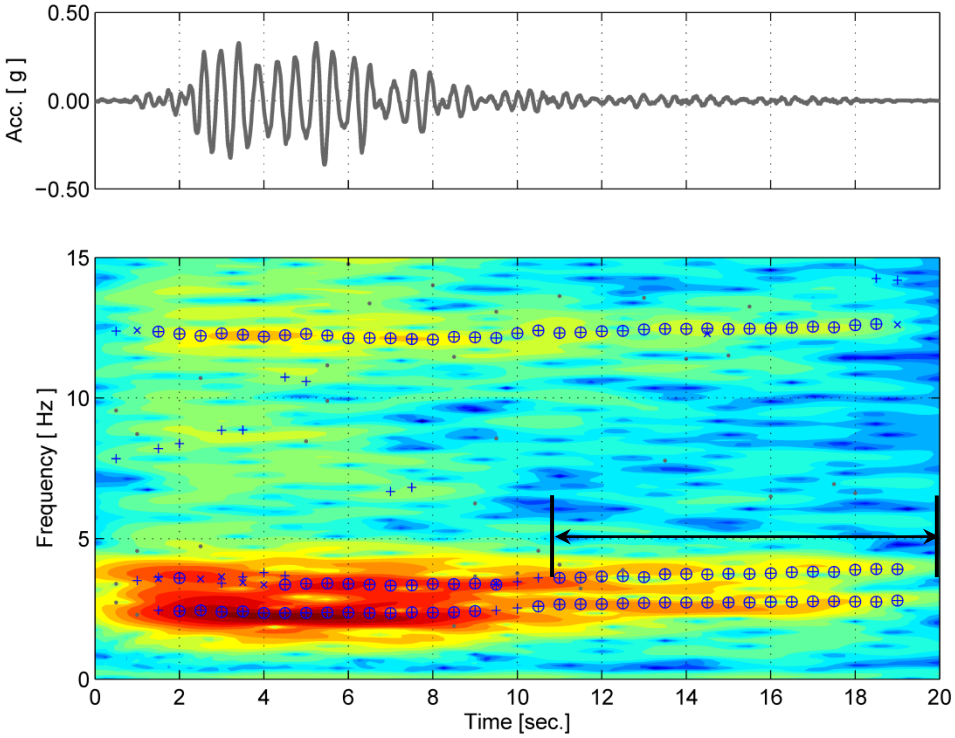

Figure 3–10 Time-dependent modal properties (Test-13)

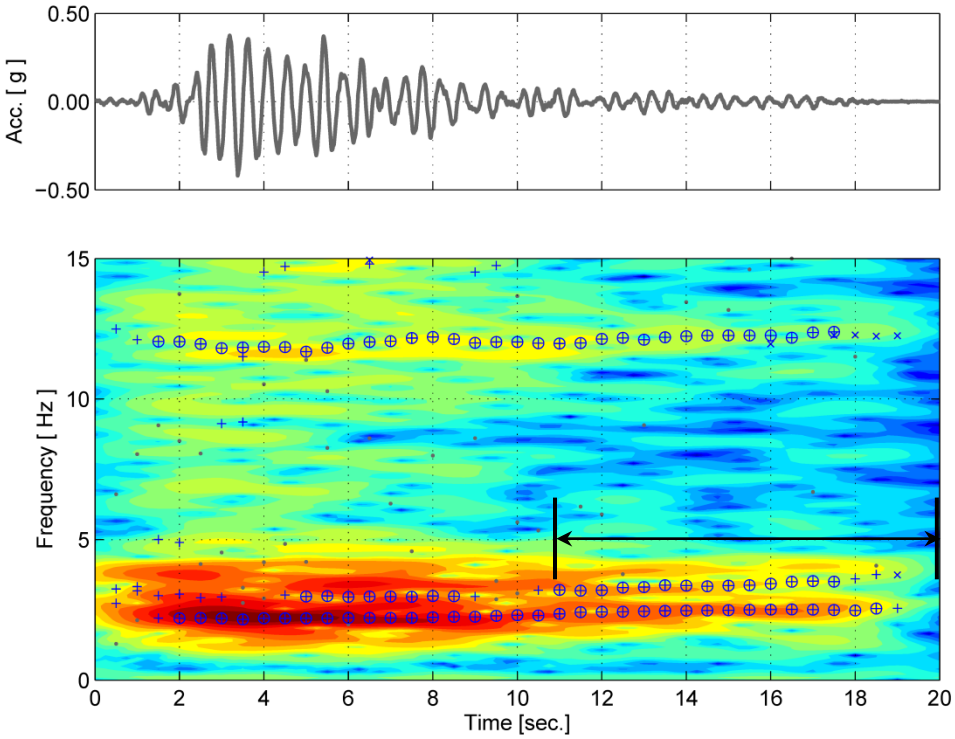

Figure 3–11 Time-dependent modal properties (Test-14)

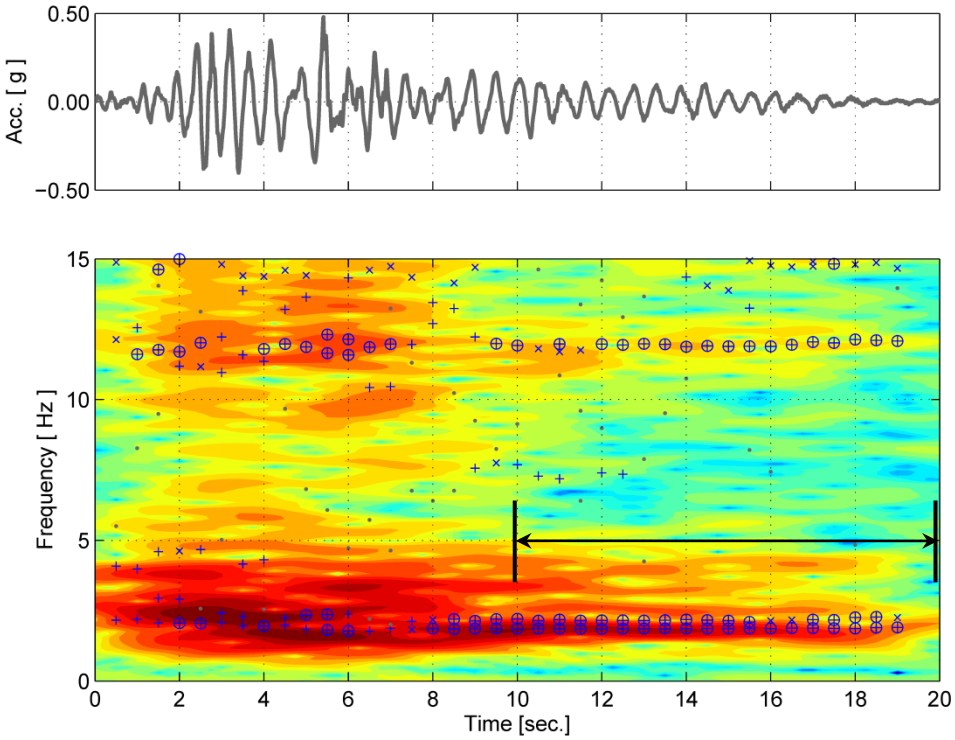

Figure 3–12 Time-dependent modal properties (Test-15)

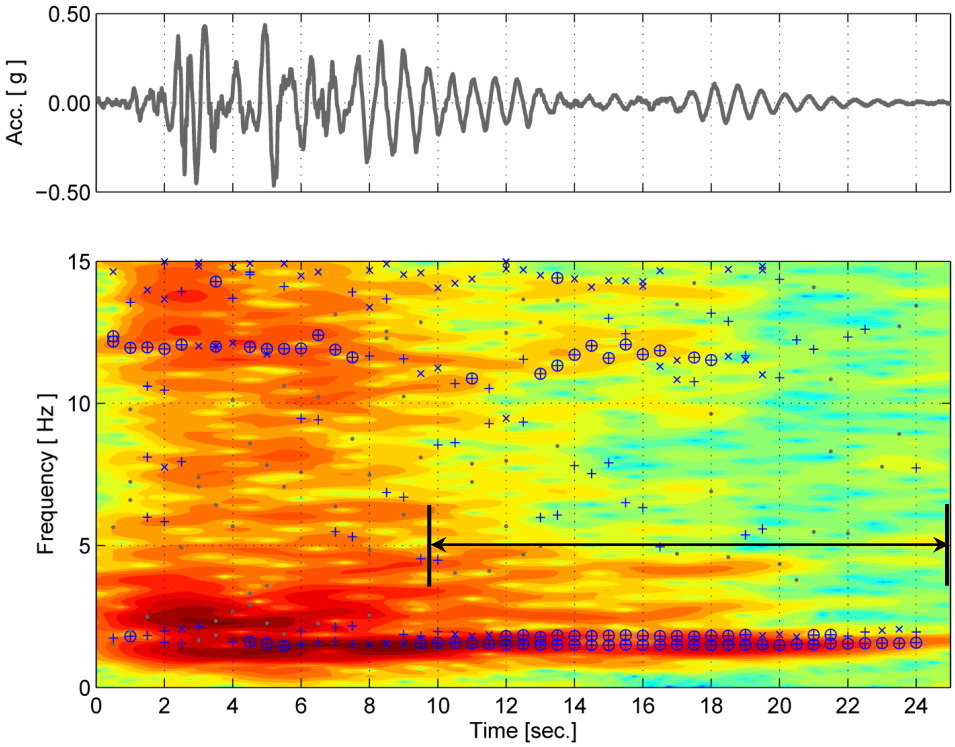

Figure 3–13 Time-dependent modal properties (Test-16)

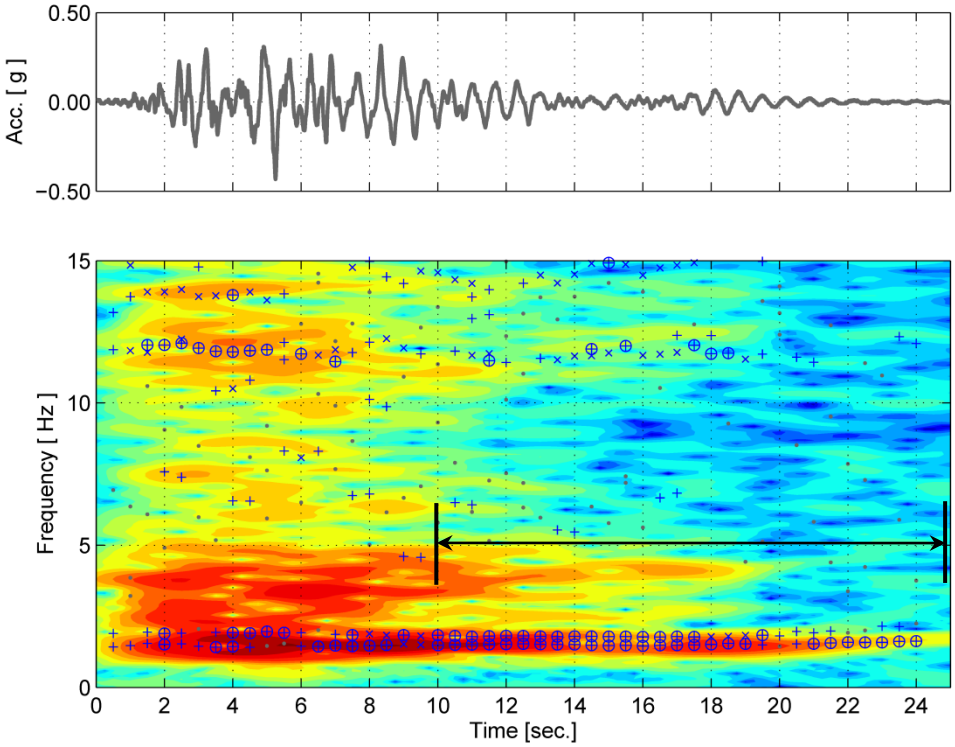

Figure 3–14 Time-dependent modal properties (Test-17)

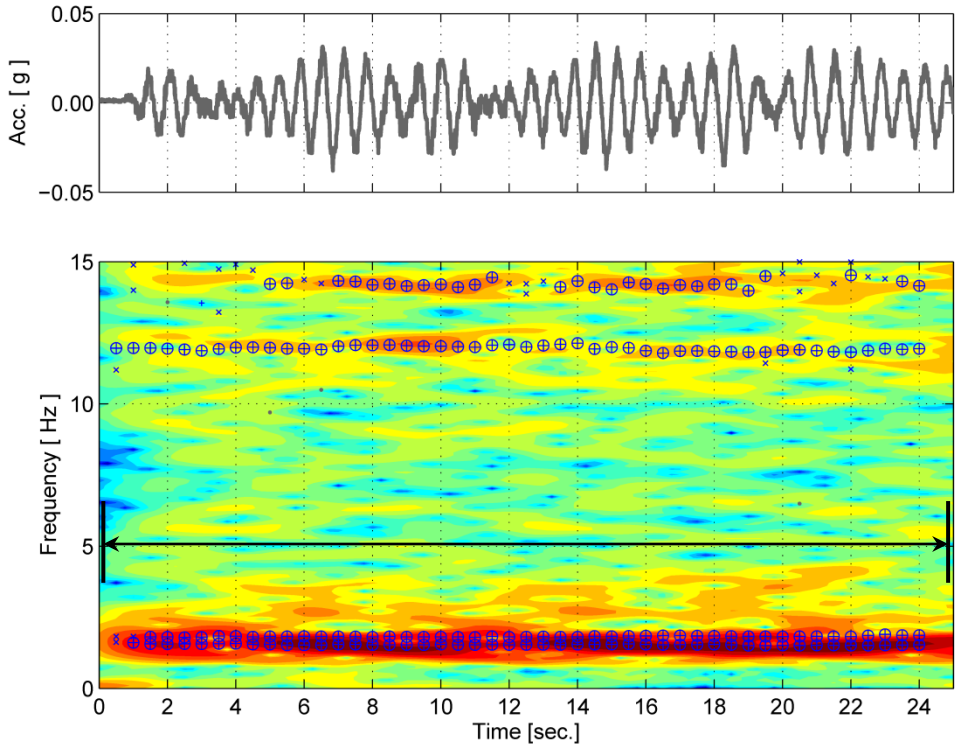

Figure 3–15 Time-dependent modal properties (WN-3)

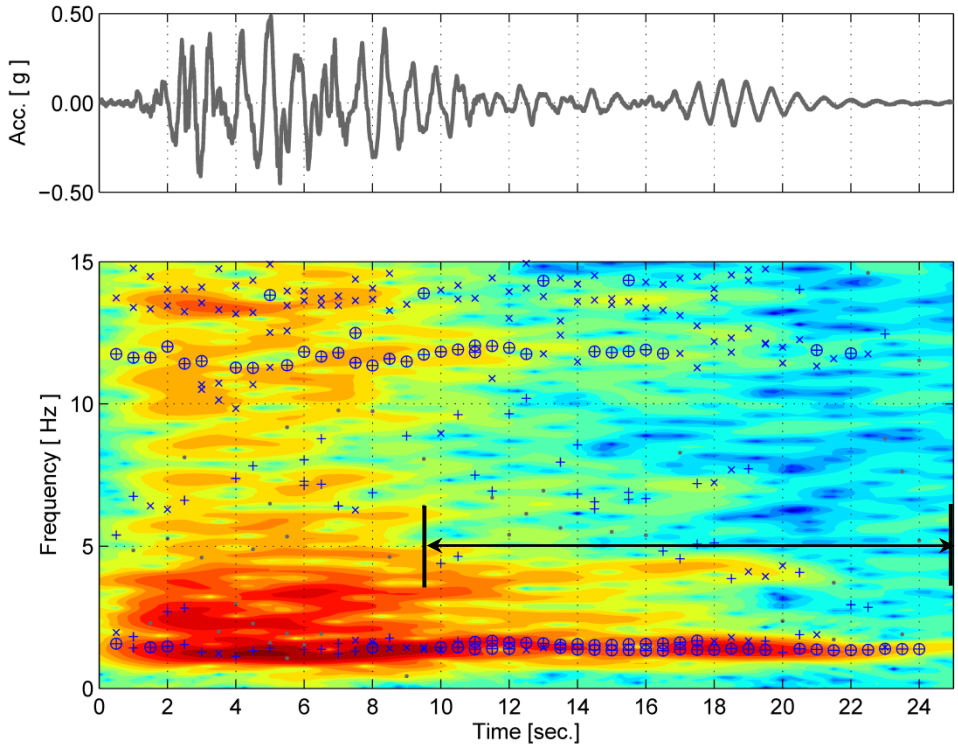

Figure 3–16 Time-dependent modal properties (Test-18)

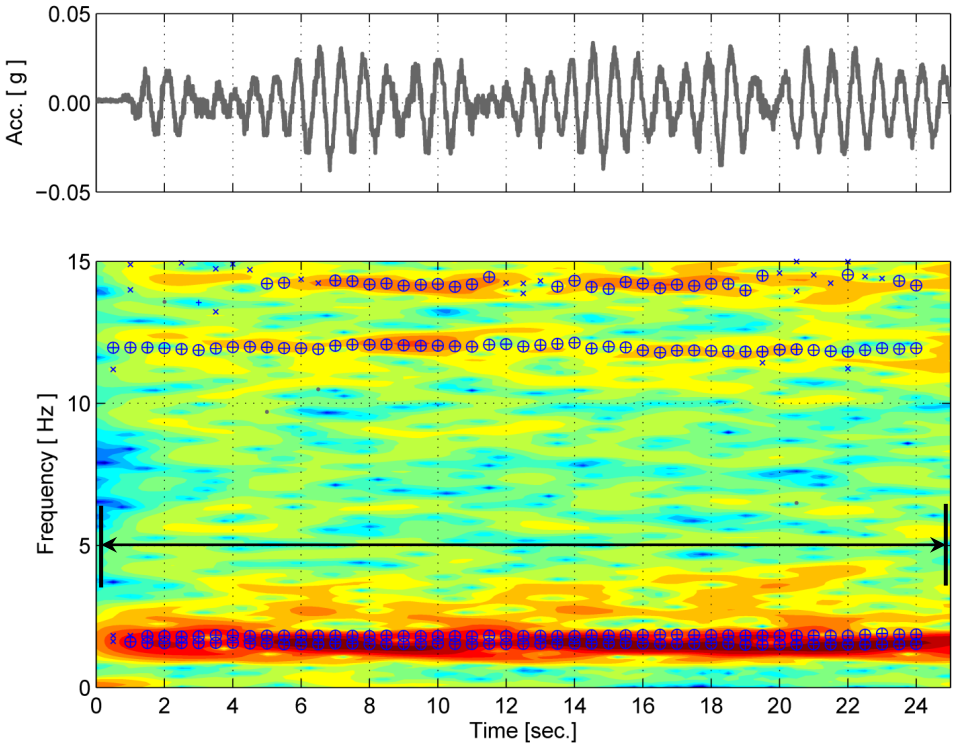

Figure 3–17 Time-dependent modal properties (WN-4)

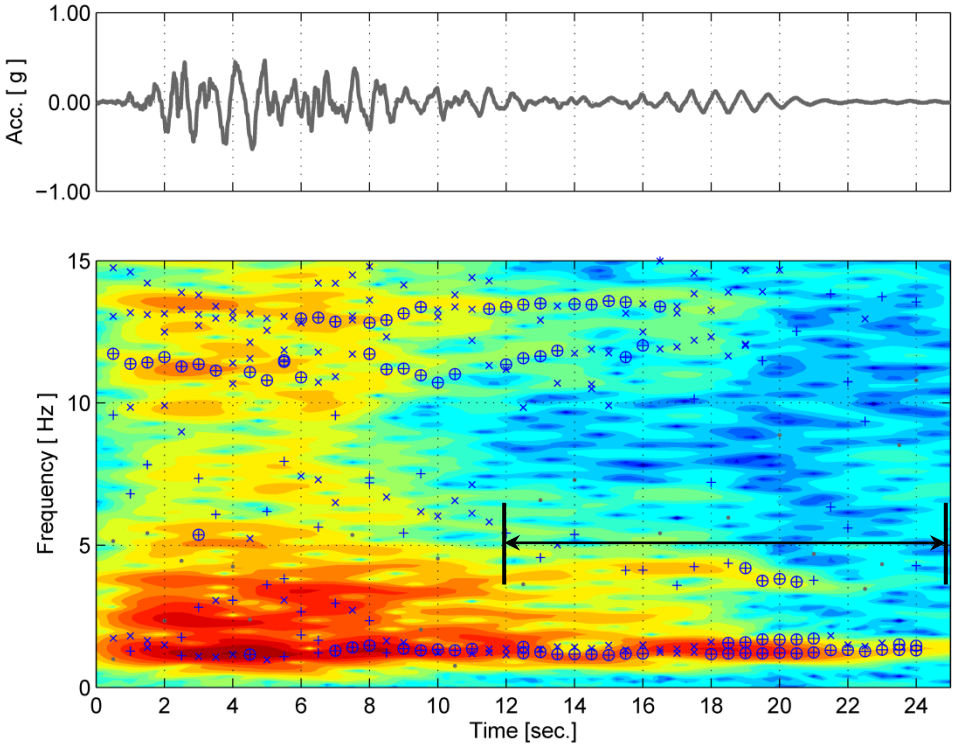

Figure 3–18 Time-dependent modal properties (Test-19)

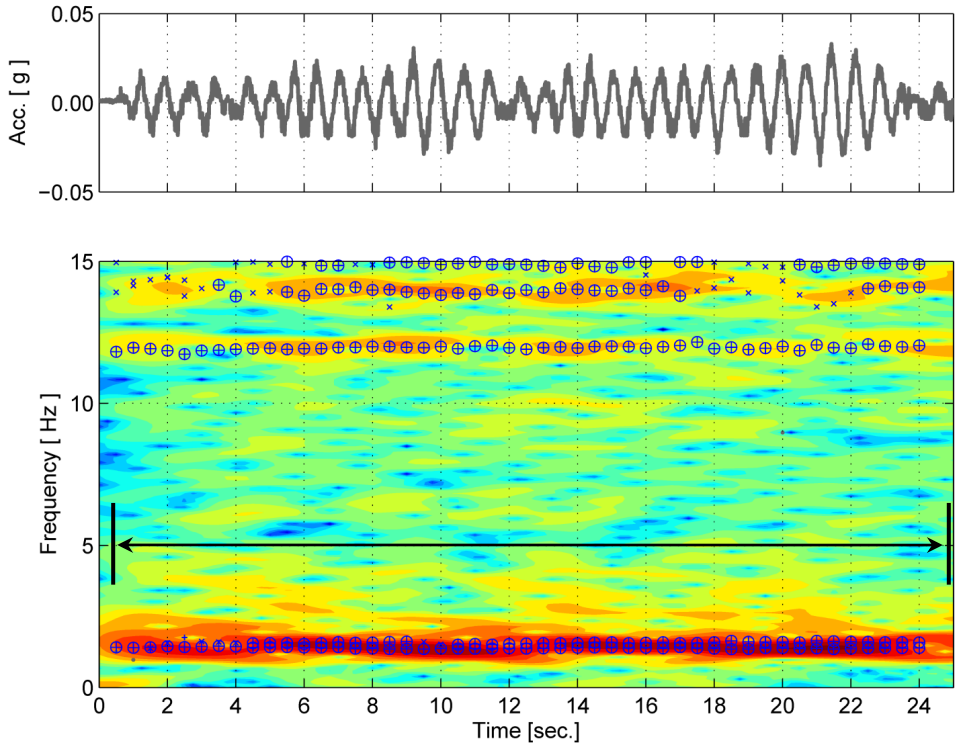

Figure 3–19 Time-dependent modal properties (WN-5)

Results of analysis show stable results over the whole time history of Test-12 and all white noise excitations which is in complete consistency with the visual inspection results that indicated no damage during these input motions. It is important to mention that stable segment of the response is selected based on the stability of the vibration modes that have been appropriately excited by the input motion. As an example, during the ending segment of Test-16 the third mode of vibration has very small contribution to the total response of the structure. As a result, corresponding modal properties are accurately identified only from a limited number of time windows and in other cases estimations are biased or corrupted by other modes' properties; hence stability criteria are not met for properties of this mode which shouldn't be interpreted as a result of nonlinearity within the structure. In such cases, the stability criteria are only checked for the significant modes of vibration to find the stable segment of the response.

3.3.2.3 Step-3: Modal Identification from Stable Segments

Stable segment of the response estimated during the second step of the procedure is used for identification of modal properties of the bridge in post-damage condition of the bridge. One of the key steps in experimental modal analysis of large-scale structures is the selection of order of the mathematical model, n, used for describing the behavior of the structure. Normally, model orders are chosen higher than the number of significant modes of vibration of the structure in order to reduce the bias on the estimates and increase the accuracy of the identified characteristics even in presence of large amount of measurement noise. As a consequence, excessive mathematical poles are added to the identified properties of the system. In order to discriminate between physically meaningful poles and the mathematical poles, stabilization diagrams are used. The basic idea is to perform several system identification runs with increasing model orders and combine identified poles in a single diagram with pole frequency as horizontal axis and model order as vertical axis. Experience on a very large range of problems shows that in such analysis, the pole values of the physical modes always appear at a nearly identical frequency, while mathematical poles tend to scatter around the frequency range [55]. Pole stability criteria are utilized to discriminate between the stable physical modes and mathematical modes. Different levels of pole stability are defined based on the deviation of the identified frequencies, damping ratios and modal shapes from the values obtained at a lower system order. The same criteria and visual styles as the ones used for identification of stable segments of the response are utilized for the analysis of the stability of identified poles. In all cases, the minimum model order that produces stable physical poles is selected.

The stabilization diagrams corresponding to the identified stable segments of the response during the second step of the procedure are presented in figure 3–20 through figure 3–26.

In these figures, left vertical axis shows the model order while right axis is used for complex mode indication function (CMIF) plot (dotted lines) of the stable segment of the response. The CMIF is the generalized version of the FDD technique and is frequently used for locating vibration modes of the physical systems in frequency domain. It is defined as the eigenvalues solved from the normal matrices of the system. The normal matrix at the spectral line ($\omega = \omega_i$) is formed from the FRF matrix of the system at the same frequency: $[H(j\omega_i)]^H [H(j\omega_i)]$. By this definition, the CMIF is equal to the square of the magnitude of the singular values. Therefore, the peaks detected in CMIF plot indicate the existence of modes and corresponding frequencies gives the corresponding damped natural frequencies.

$$CMIF_k(j\omega) \equiv \mu_k(j\omega) \equiv \sigma_k^2(j\omega) \qquad k = 1, 2, , N_d \tag{3-76}$$

$$\left[H\left(j\omega\right)\right]^H \left[H\left(j\omega\right)\right] = \left[V\left(j\omega\right)\right] \left|\Sigma^2\left(j\omega\right)\right| \left[V\left(j\omega\right)\right]^H \tag{3-77}$$

Here $CMIF_k(j\omega)$ is the k th CMIF at frequency ω. $\mu_k(j\omega)$ is the k th eigenvalue of the normal matrix of FRF at frequency ω. $\sigma_k^2(j\omega)$ is the k th singular value of the FRF matrix at frequency ω and N_d is the number of dominant modes of vibration of the structure. For more details of the method, interested reader is referred to Shih et al. [56].

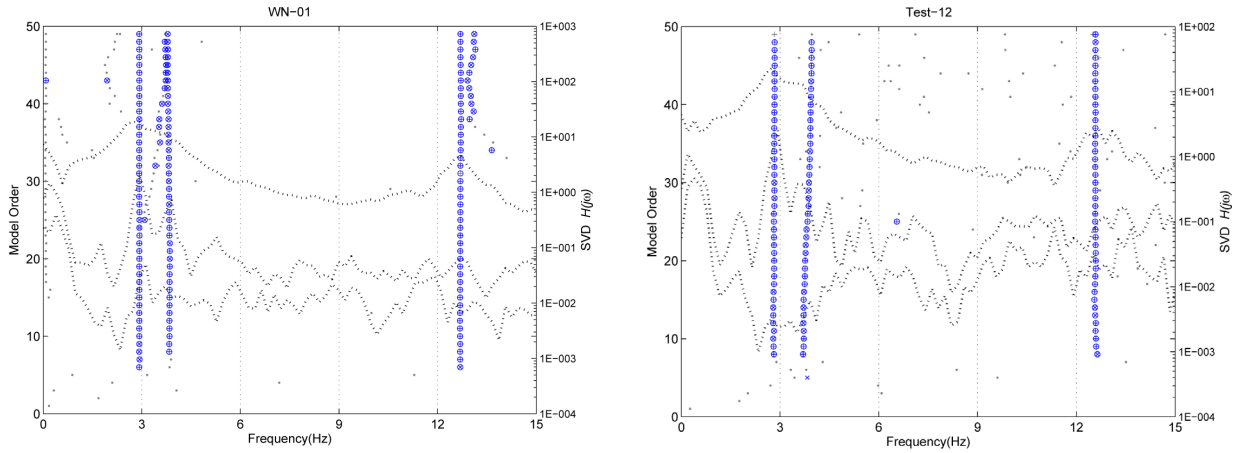

(a) (b)

Figure 3–20 Stabilization diagram (a) W.N.1 (b) Test-12

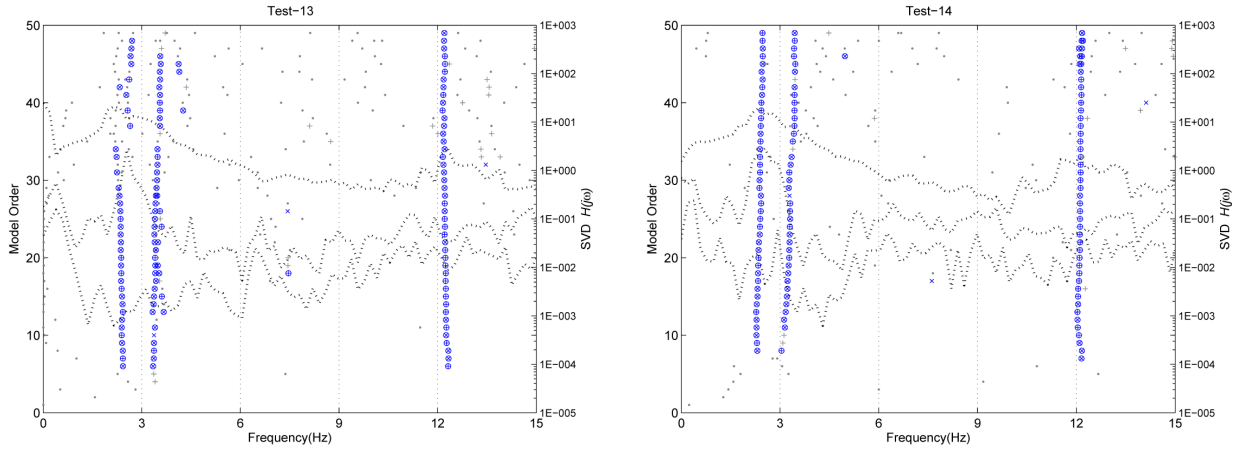

(a) (b)

Figure 3–21 Stabilization diagram (a) Test-13 (b) Test-14

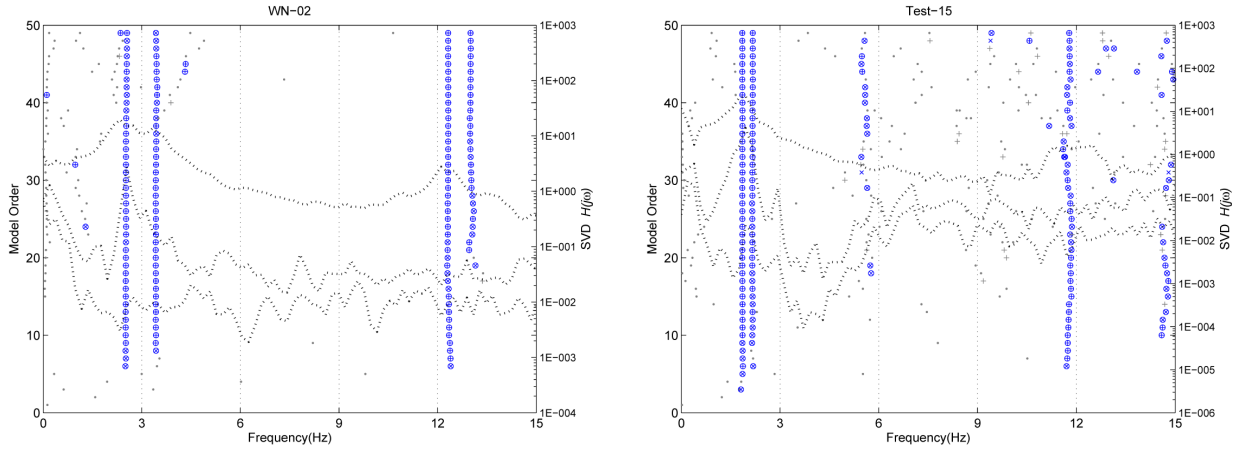

(a) (b)

Figure 3–22 Stabilization diagram (a) W.N.2 (b) Test-15

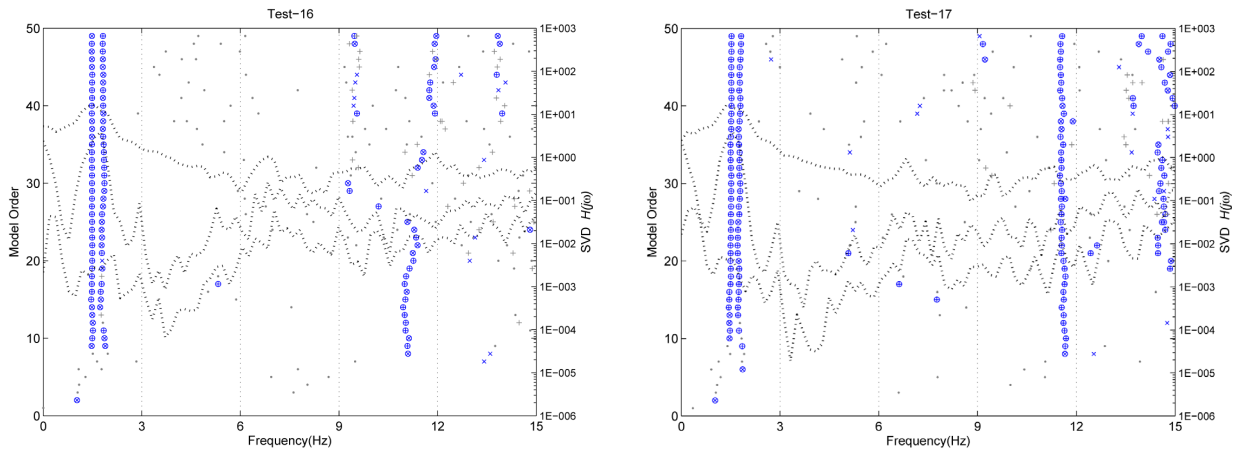

(a) (b)

Figure 3–23 Stabilization diagram (a) Test-16 (b) Test-17

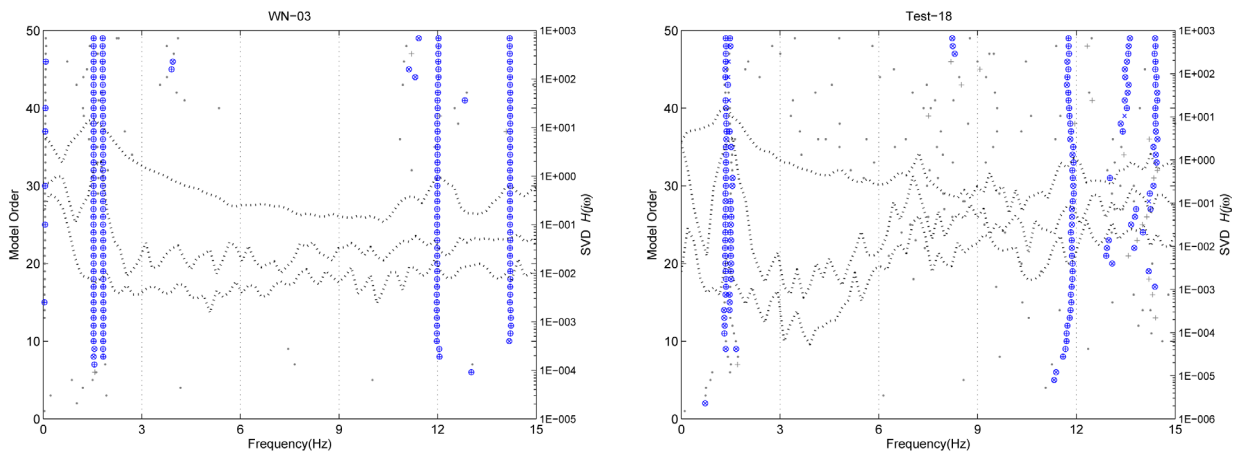

(a) (b)

Figure 3–24 Stabilization diagram (a) W.N.3 (b) Test-18

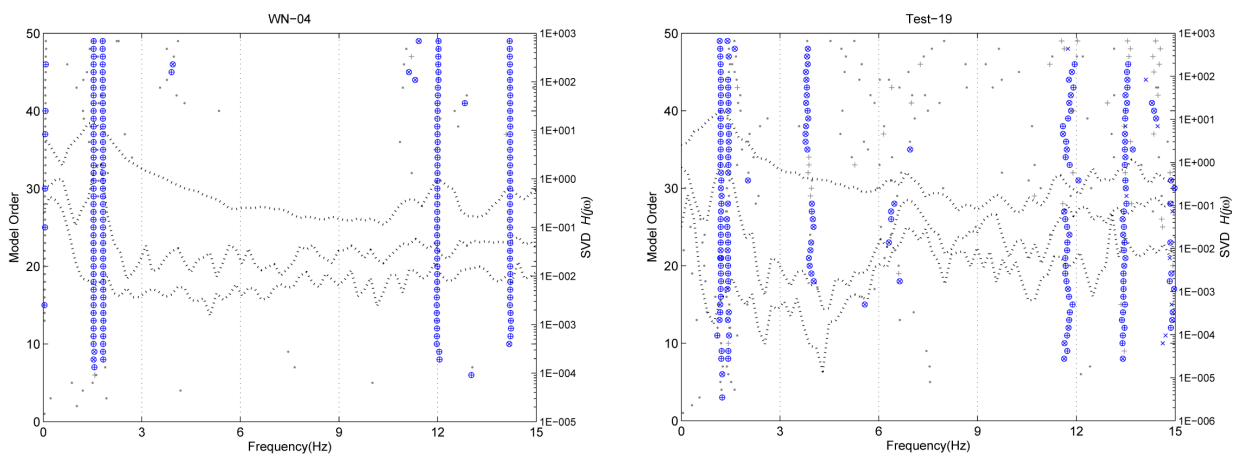

(a) (b)

Figure 3–25 Stabilization diagram (a) W.N.4 (b) Test-19

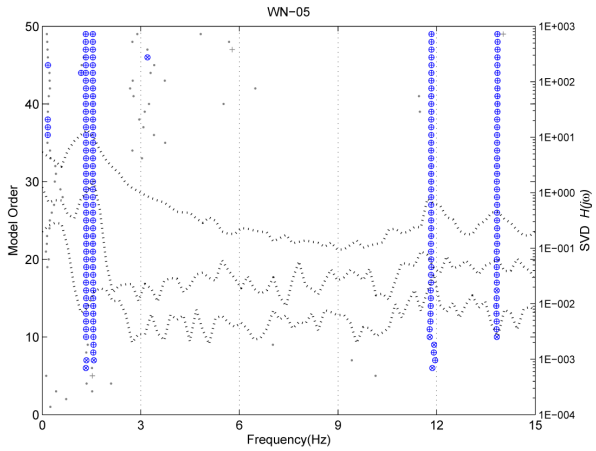

Figure 3–26 Stabilization diagram (WN-5)

Using the selected model order post-damage modal properties of the bridge are identified from stable segment of the response resulted from the second step of the procedure. Both prediction error and subspace-based methods are applied for system identification of the bridge. In figure 3–27 through figure 3–39 the results of simulation using prediction error method are compared with the acceleration response measurements at channels 1,3 and 5 located at the top of the bents of the bridge. The good matches between the response measurements and results of simulation using a single linear time-invariant state space model indicate the efficacy of proposed procedure for identification of linear segment of the response with stable dynamic properties. It is also important to mention that both system identification approaches showed outstanding performance for parameter estimation from short signals with non-zero initial conditions. Further analysis of the results is presented in the following section.

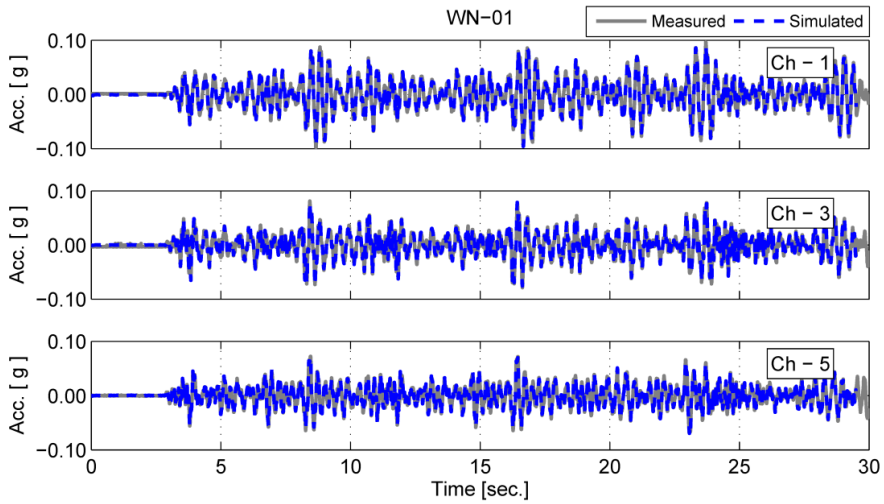

Figure 3–27 Acceleration measurements and simulation results (WN-1)

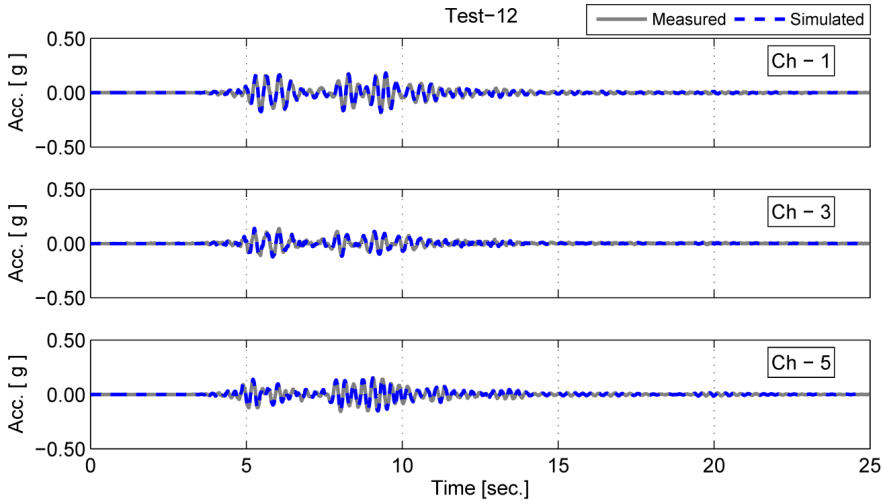

Figure 3–28 Acceleration measurements and simulation results (Test-12)

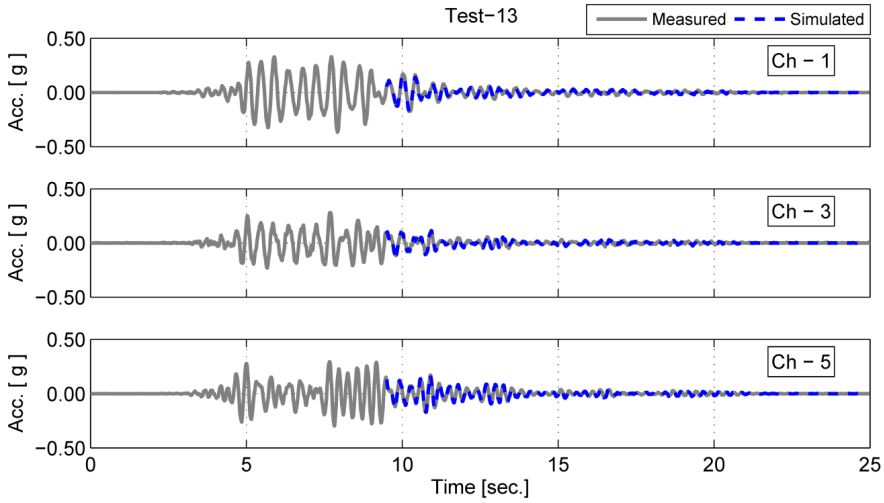

Figure 3–29 Acceleration measurements and simulation results (Test-13)

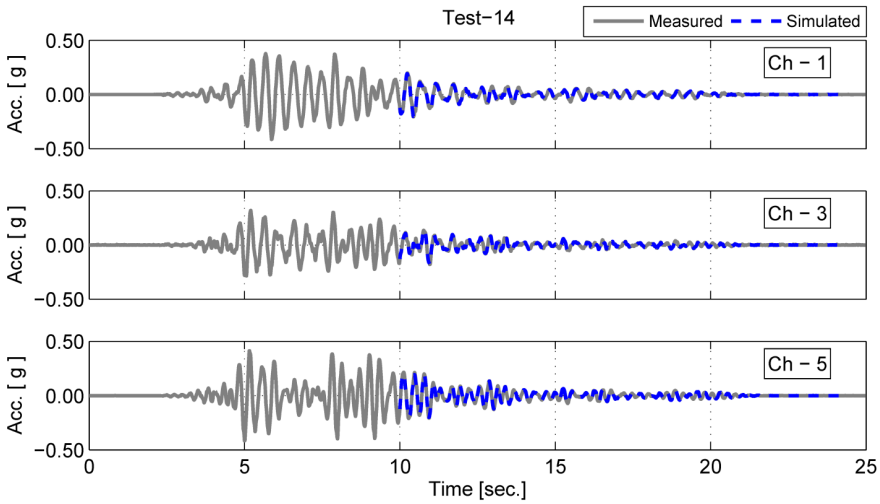

Figure 3–30 Acceleration measurements and simulation results (Test-14)

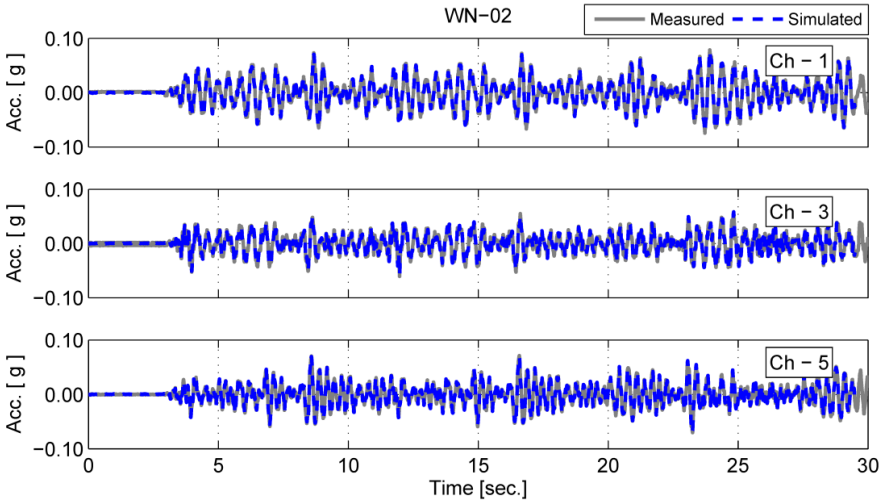

Figure 3–31 Acceleration measurements and simulation results (WN-2)

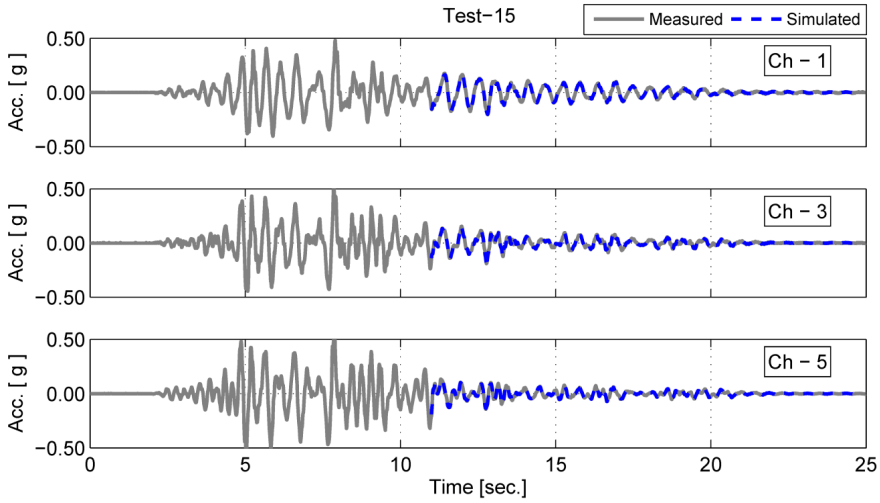

Figure 3–32 Acceleration measurements and simulation results (Test-15)

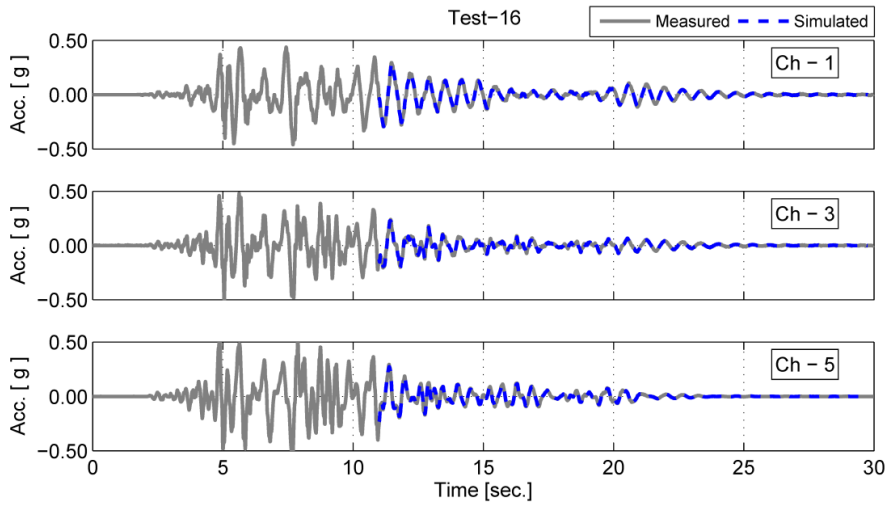

Figure 3–33 Acceleration measurements and simulation results (Test-16)

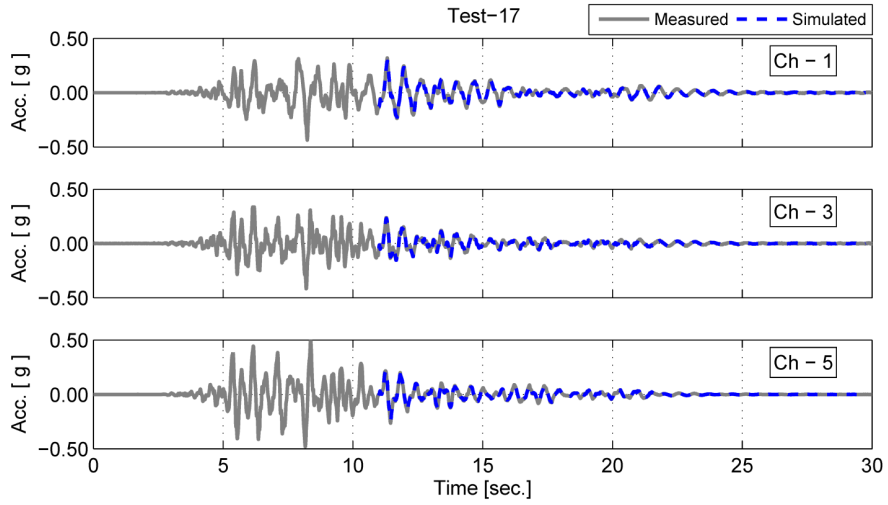

Figure 3–34 Acceleration measurements and simulation results (Test-17)

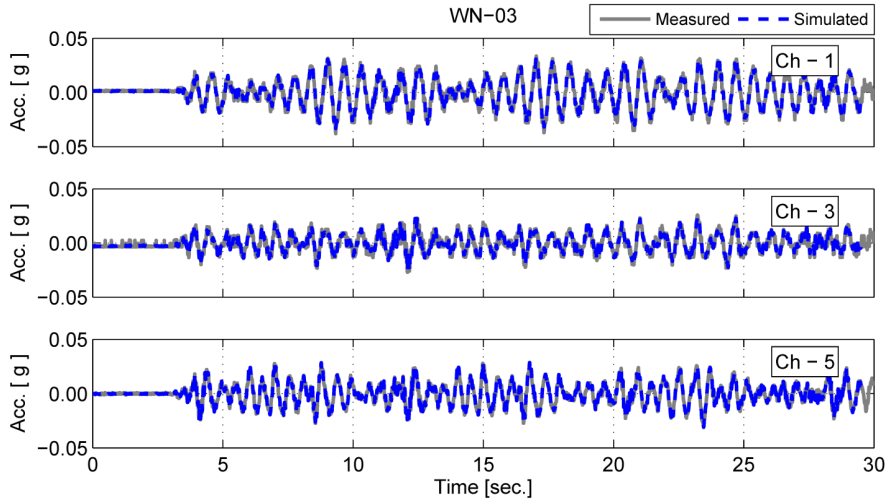

Figure 3–35 Acceleration measurements and simulation results (WN-3)

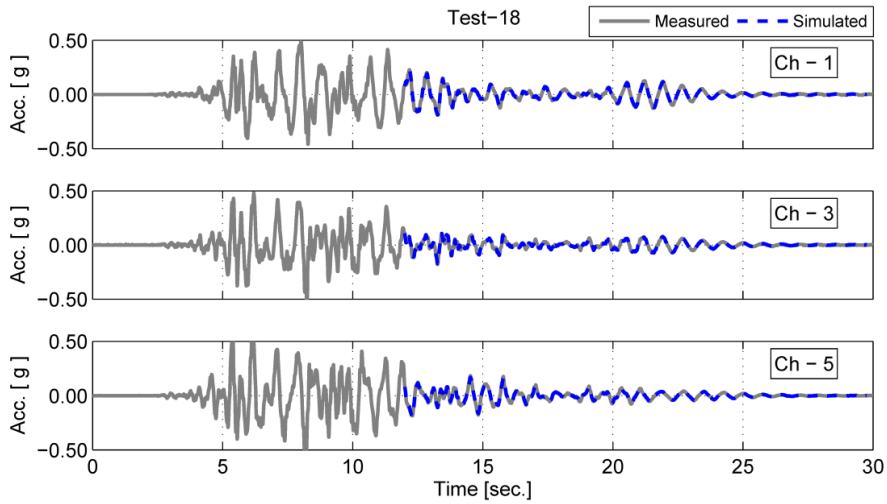

Figure 3–36 Acceleration measurements and simulation results (Test-18)

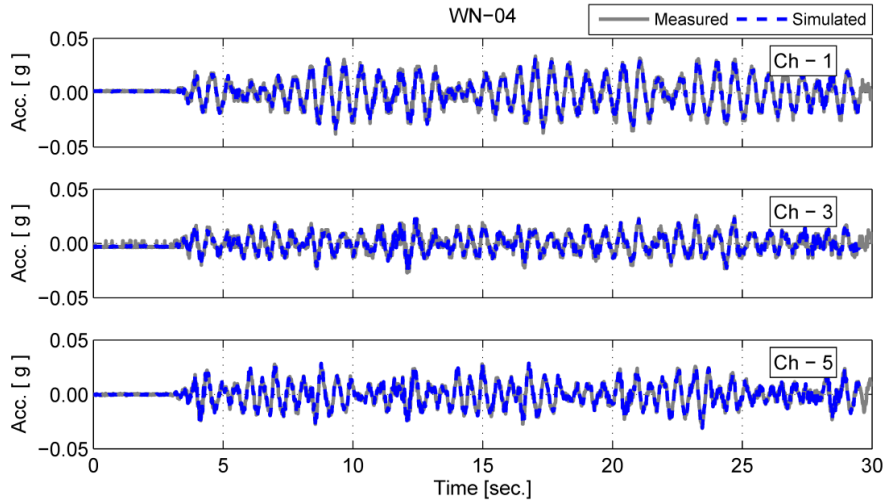

Figure 3–37 Acceleration measurements and simulation results (WN-4)

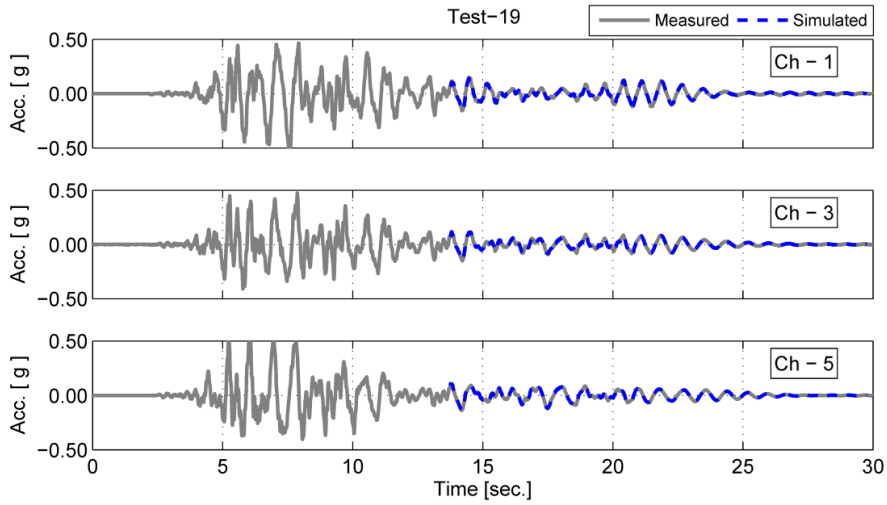

Figure 3–38 Acceleration measurements and simulation results (Test-19)

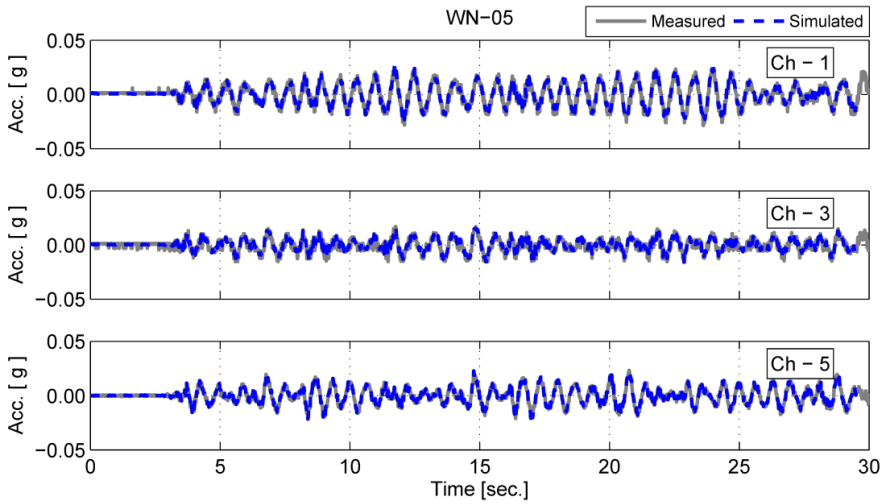

Figure 3–39 Acceleration measurements and simulation results (WN-5)

The modal properties (natural frequencies, damping ratios and mode shapes) of the first three transverse vibration modes of the bridge identified from white noise and stable segments of earthquake excitations using prediction-error and subspace-based methods are listed in table 3-6 through table 3-11. In the last column of each table, modal shapes of the bridge identified from different types of motion but from the same damage states of the bridge are compared. As an example, modal shapes identified from stable ending segment of Test-14 are compared with the shapes identified from W.N.-2 (which was input to the bridge right after Test-14).

Table 3-6 Properties of the first transverse vibration (prediction error method)

	f_1 (Hz)	ζ_1	ϕ_{1i}	ϕ_{2i}	ϕ_{3i}	ϕ_{4i}	ϕ_{5i}	*MAC*
WN-1	2.920	1.9%	0.649	0.545	0.423	0.295	0.127	1.000
Test-12	2.810	2.1%	0.654	0.544	0.417	0.291	0.134	
Test-13	2.390	2.4%	0.663	0.543	0.407	0.288	0.128	
Test-14	2.240	3.7%	0.667	0.543	0.406	0.282	0.124	0.998
WN-2	2.490	2.0%	0.678	0.548	0.405	0.261	0.087	
Test-15	1.850	3.0%	0.633	0.531	0.419	0.322	0.194	
Test-16	1.500	6.0%	0.653	0.534	0.415	0.297	0.166	
Test-17	1.500	7.1%	0.653	0.534	0.415	0.297	0.166	0.970
WN-3	1.530	4.0%	0.711	0.551	0.377	0.218	0.029	
Test-18	1.360	7.0%	0.553	0.503	0.436	0.386	0.319	0.993
WN-4	1.390	7.7%	0.592	0.527	0.428	0.346	0.263	
Test-19	1.200	10.2%	0.242	0.348	0.424	0.515	0.613	0.666
WN-5	1.330	7.3%	0.626	0.525	0.424	0.323	0.222	

Table 3-7 Properties of the first transverse vibration mode (subspace method)

	f_1 (Hz)	ζ_1	ϕ_{1i}	ϕ_{2i}	ϕ_{3i}	ϕ_{4i}	ϕ_{5i}	*MAC*
WN-1	2.925	1.7%	0.653	0.548	0.418	0.290	0.121	1.000
Test-12	2.825	1.8%	0.655	0.546	0.414	0.292	0.129	
Test-13	2.410	2.6%	0.649	0.543	0.414	0.299	0.151	
Test-14	2.260	3.2%	0.655	0.541	0.415	0.293	0.141	0.994
WN-2	2.498	2.4%	0.684	0.547	0.400	0.258	0.076	
Test-15	1.862	3.1%	0.671	0.539	0.403	0.281	0.133	
Test-16	1.508	6.9%	0.661	0.536	0.409	0.293	0.151	
Test-17	1.496	8.2%	0.679	0.538	0.402	0.272	0.123	1.000
WN-3	1.541	4.9%	0.678	0.536	0.403	0.274	0.122	
Test-18	1.377	8.2%	0.595	0.516	0.429	0.355	0.265	0.995
WN-4	1.402	7.0%	0.564	0.499	0.430	0.384	0.316	
Test-19	1.199	8.5%	0.321	0.390	0.432	0.496	0.559	0.814
WN-5	1.342	7.0%	0.593	0.515	0.431	0.357	0.265	

Table 3-8 Properties of the second transverse vibration mode (prediction error method)

	f_i (Hz)	ζ_i	ϕ_{1i}	ϕ_{2i}	ϕ_{3i}	ϕ_{4i}	ϕ_{5i}	MAC
WN-1	3.660	2.5%	0.410	0.082	-0.228	-0.492	-0.729	0.998
Test-12	3.660	2.3%	0.381	0.051	-0.216	-0.495	-0.749	
Test-13	3.320	0.6%	0.346	0.029	-0.245	-0.505	-0.751	
Test-14	2.970	0.9%	0.323	0.017	-0.247	-0.511	-0.757	0.999
WN-2	3.360	3.2%	0.341	0.020	-0.261	-0.512	-0.743	
Test-15	2.200	14.9%	0.375	0.094	-0.211	-0.493	-0.751	
Test-16	1.840	5.6%	0.365	0.073	-0.219	-0.475	-0.767	
Test-17	1.820	11.9%	0.384	0.082	-0.192	-0.467	-0.769	0.995
WN-3	1.830	7.5%	0.346	0.031	-0.220	-0.487	-0.770	
Test-18	1.610	13.1%	0.547	0.209	-0.091	-0.391	-0.704	1.000
WN-4	1.580	8.4%	0.536	0.209	-0.089	-0.387	-0.715	
Test-19	1.440	7.6%	0.721	0.410	0.170	-0.198	-0.495	0.652
WN-5	1.560	5.9%	0.455	0.119	-0.158	-0.435	-0.751	

Table 3-9 Properties of the second transverse vibration mode (subspace method)

	f_i (Hz)	ζ_i	ϕ_{1i}	ϕ_{2i}	ϕ_{3i}	ϕ_{4i}	ϕ_{5i}	MAC
WN-1	3.855	2.5%	0.357	0.028	-0.242	-0.509	-0.744	1.000
Test-12	3.710	2.5%	0.361	0.029	-0.238	-0.507	-0.745	
Test-13	3.348	0.6%	0.341	0.015	-0.251	-0.511	-0.748	
Test-14	3.007	0.9%	0.330	0.022	-0.245	-0.507	-0.757	0.997
WN-2	3.474	3.9%	0.306	-0.015	-0.268	-0.520	-0.751	
Test-15	2.200	13.4%	0.207	-0.102	-0.307	-0.526	-0.759	
Test-16	1.832	6.0%	0.488	0.158	-0.136	-0.425	-0.733	
Test-17	1.820	11.1%	0.407	0.095	-0.193	-0.467	-0.755	0.980
WN-3	1.835	6.3%	0.303	0.021	-0.235	-0.502	-0.775	
Test-18	1.572	11.5%	0.654	0.328	0.100	-0.295	-0.607	0.876
WN-4	1.581	9.6%	0.496	0.208	-0.148	-0.418	-0.717	
Test-19	1.442	9.1%	0.699	0.392	0.145	-0.230	-0.532	0.776
WN-5	1.559	5.1%	0.499	0.167	-0.127	-0.413	-0.732	

Table 3-10 Properties of the third transverse vibration mode (prediction error method)

	f_i (Hz)	ζ_i	ϕ_{1i}	ϕ_{2i}	ϕ_{3i}	ϕ_{4i}	ϕ_{5i}	MAC
WN-1	12.780	2.0%	0.409	-0.409	-0.607	-0.385	0.385	1.000
Test-12	12.640	1.9%	0.411	-0.411	-0.616	-0.376	0.376	
Test-13	12.440	2.5%	0.404	-0.404	-0.590	-0.404	0.404	
Test-14	12.390	4.0%	0.388	-0.388	-0.582	-0.355	0.485	0.996
WN-2	12.500	2.4%	0.390	-0.404	-0.598	-0.376	0.431	
Test-15	11.770	5.0%	0.404	-0.404	-0.607	-0.404	0.376	
Test-16	11.020	7.7%	0.386	-0.386	-0.675	-0.434	0.241	
Test-17	11.470	5.1%	0.416	-0.416	-0.594	-0.416	0.357	0.981
WN-3	12.100	2.6%	0.301	-0.402	-0.652	-0.402	0.402	
Test-18	11.300	7.8%	0.374	-0.421	-0.654	-0.421	0.280	0.989
WN-4	12.080	1.7%	0.313	-0.402	-0.671	-0.402	0.358	
Test-19	11.870	5.1%	0.341	-0.426	-0.511	-0.426	0.511	0.962
WN-5	11.900	1.4%	0.323	-0.415	-0.645	-0.415	0.369	

Table 3-11 Properties of the third transverse vibration mode (subspace method)

	f_i (Hz)	ζ_i	φ_{1i}	φ_{2i}	φ_{3i}	φ_{4i}	φ_{5i}	MAC
WN-1	12.709	1.7%	0.407	-0.416	-0.616	-0.366	0.384	1.000
Test-12	12.608	1.9%	0.401	-0.414	-0.624	-0.364	0.382	
Test-13	12.305	2.7%	0.390	-0.416	-0.620	-0.376	0.385	
Test-14	12.141	4.3%	0.395	-0.407	-0.616	-0.372	0.399	1.000
WN-2	12.375	2.2%	0.388	-0.416	-0.619	-0.371	0.394	
Test-15	11.732	5.1%	0.391	-0.407	-0.609	-0.411	0.375	
Test-16	11.033	8.6%	0.375	-0.412	-0.646	-0.458	0.250	
Test-17	11.557	5.1%	0.402	-0.397	-0.604	-0.408	0.387	0.991
WN-3	12.064	2.3%	0.318	-0.422	-0.636	-0.389	0.406	
Test-18	11.505	7.5%	0.368	-0.424	-0.599	-0.433	0.373	0.991
WN-4	12.084	1.8%	0.305	-0.413	-0.648	-0.394	0.400	
Test-19	11.777	4.5%	0.441	-0.402	-0.506	-0.363	0.506	0.964
WN-5	11.895	1.7%	0.350	-0.410	-0.628	-0.397	0.397	

3.4 Summary of Modal Identification Results

The results of modal identification from the responses to white noise and earthquake excitations are analyzed and compared in this section. As the first step, modal properties identified from the responses to white noise excitations using output-only and input-output techniques are compared. Table 3-12 presents the relative error between identified frequencies and MAC values between identified mode shapes using FDD technique as an output-only technique and prediction-error and stochastic subspace methods as input-output identification techniques.

Table 3-12 Comparison of modal data identified from white noise excitations

		Mode – 1		Mode – 2		Mode – 3	
	Id. Methods	Δf_1	MAC_1	Δf_2	MAC_2	Δf_3	MAC_3
WN-1	*PEM-FDD*	7.43%	0.974	8.44%	0.672	1.24%	1.000
	SS-FDD	7.59%	0.971	13.07%	0.607	0.69%	0.999
	PEM-SS	0.17%	1.000	5.33%	0.994	0.56%	0.999
WN-2	*PEM-FDD*	6.59%	0.988	0.24%	0.975	1.75%	0.997
	SS-FDD	6.89%	0.985	3.05%	0.959	0.76%	1.000
	PEM-SS	0.32%	1.000	3.39%	0.997	1.00%	0.998
WN-3	*PEM-FDD*	2.42%	0.961	6.17%	0.729	0.67%	0.993
	SS-FDD	3.11%	0.906	6.43%	0.699	0.37%	0.997
	PEM-SS	0.72%	0.986	0.27%	0.998	0.30%	0.999
WN-4	*PEM-FDD*	0.29%	0.915	7.09%	0.724	0.46%	0.983
	SS-FDD	0.57%	0.869	7.15%	0.665	0.49%	0.984
	PEM-SS	0.86%	0.994	0.06%	0.994	0.03%	0.997
WN-5	*PEM-FDD*	4.66%	0.998	4.87%	0.833	1.58%	0.989
	SS-FDD	5.51%	0.991	4.81%	0.882	1.54%	0.994
	PEM-SS	0.90%	0.996	0.06%	0.994	0.04%	0.998

Considering the approximation involved in modal identification from output-only data, the results of the FDD technique are in good agreement with input-output methods' results.

Comparisons of the modal data from prediction-error and subspace methods indicate almost perfect agreement between the results of two input-output methods. The largest discrepancies between modal data appeared on the second mode properties. The proximity of natural frequencies of the first two modes and lower participation of the second mode in total response contributed to the biased estimated of the second mode properties.

In order to evaluate the performance of applied system identification approaches, the results of each system identification method during the time-frequency analysis and modal identification process are compared. The time-dependent modal frequencies of the bridge over the whole experiment identified using prediction error and subspace-based method s are compared in figure 3–40 through figure 3–42. In these figures, the plot on the left shows the modal frequency tracking results using 300-data-point time windows and right plot presents the results of 600-data-point windows. Moving averages curves of the identified modal frequencies are added for general comparison purposes (dashed and dotted lines).

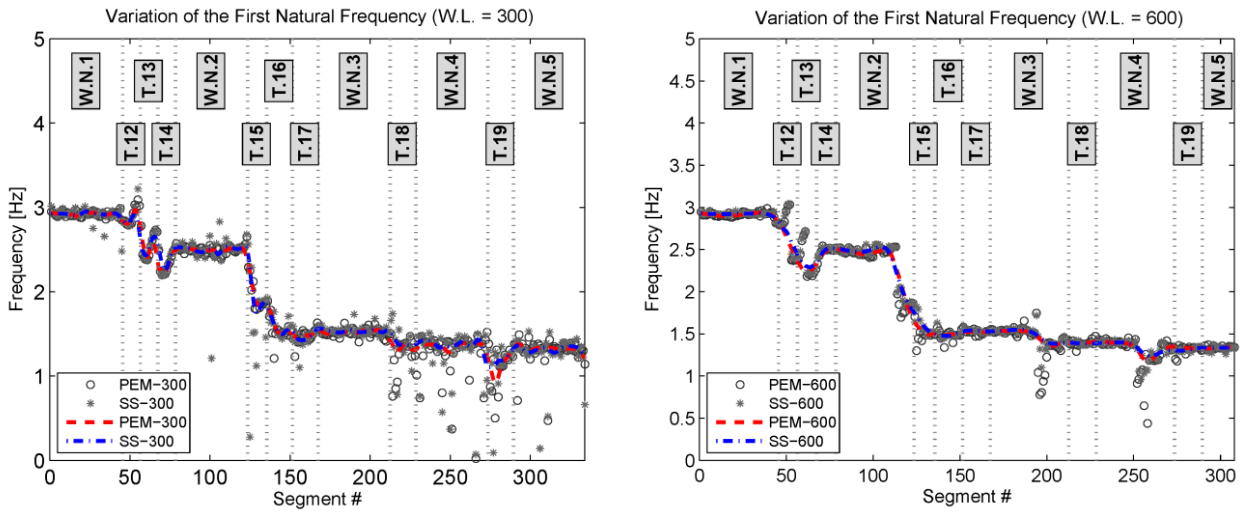

(a) (b)

Figure 3–40 Time-dependent first mode frequency: (a) 300-point (b) 600-point window

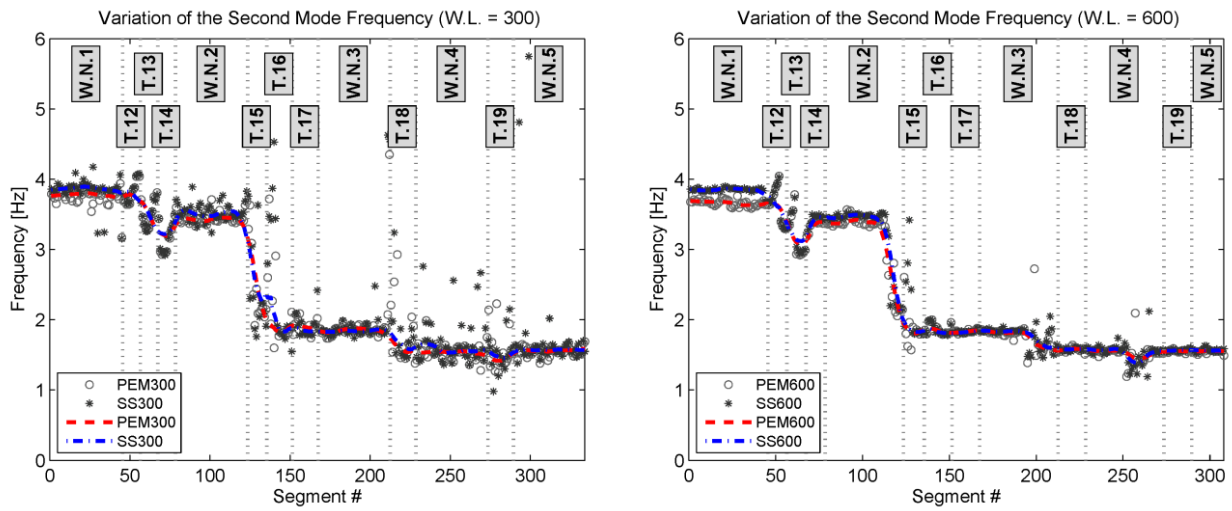

(a) (b)

Figure 3–41 Time-dependent second mode frequency: (a) 300-point (b) 600-point window

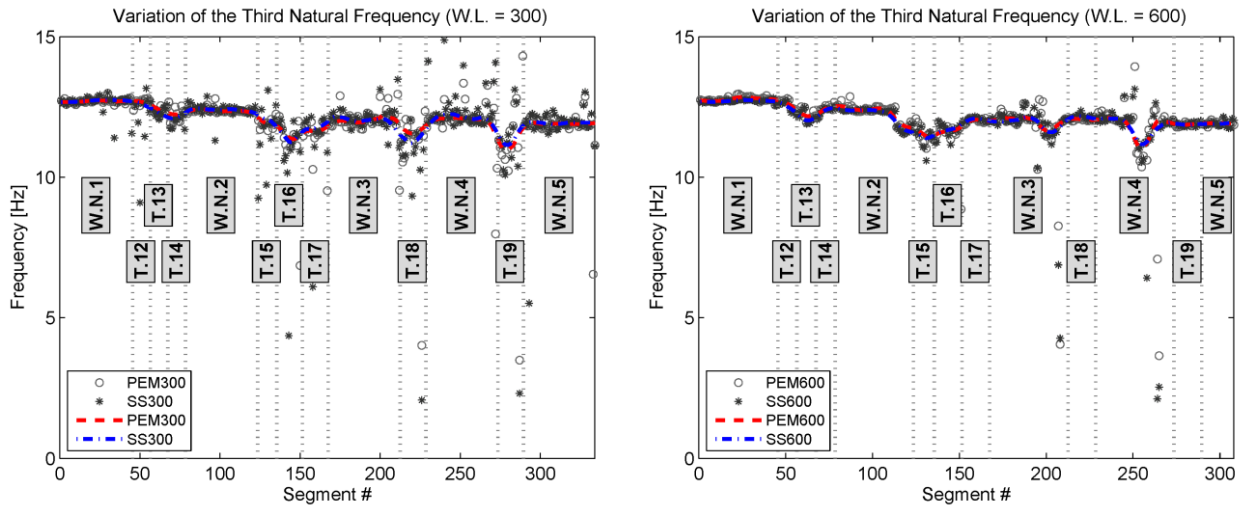

(a) (b)

Figure 3–42 Time-dependent third mode frequency: (a) 300-point (b) 600-point window

The comparison of the identified time-dependent modal frequencies demonstrates the good agreement between natural frequencies identified from both applied system identification approaches. As it was expected, both methods produced more scattered (and less reliable) modal frequencies from the shorter time windows (300-point). In order to investigate the effect of the window length and the choice of system identification technique in a quantitative manner, model fitness values defined in equation (3-72) are utilized. The fitness values of all state space models

fitted by either of the system identification approaches using either of time windows are calculated for the responses to white noise and earthquake excitations. Due to different characteristics of the responses to these different motion types, corresponding fitness values are analyzed separately. Density distributions of fitness values are presented in figure 3–43 and figure 3–44. As listed in table 3-13 in all variations of input motion type and time window length, prediction error system identification technique produced higher mean fitness values with lower dispersion properties. This could be interpreted as the higher reliability of the PEM results which are generally produced at higher computational costs.

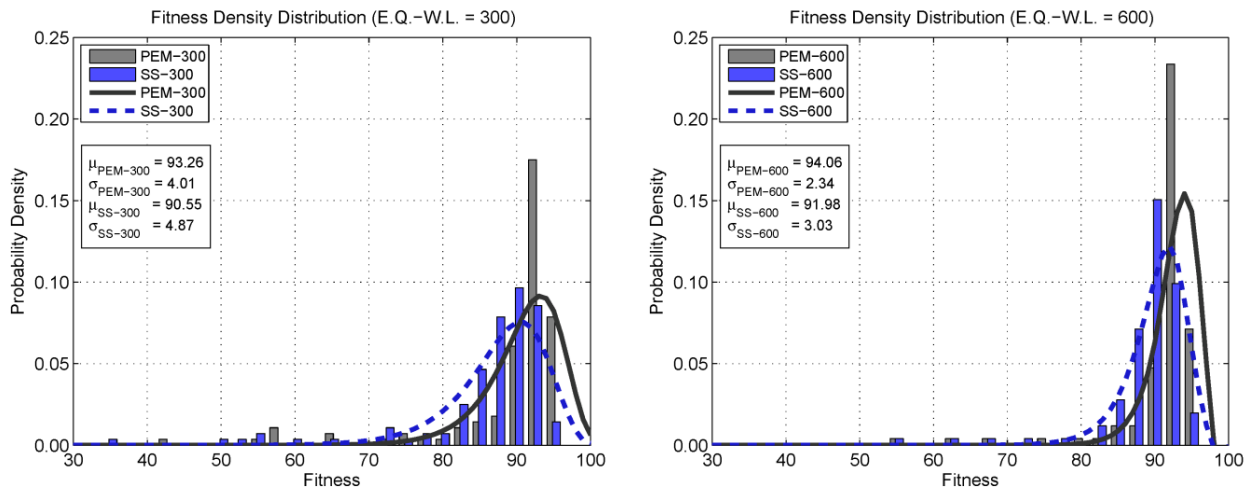

(a) (b)

Figure 3–43 Fitness distribution for earthquake responses (a) 300-point (b) 600-point window

Table 3-13 Fitness distributions properties

Identification Method		*Prediction Error Method*		*Stochastic Subspace Method*	
Window Length		*300-points*	*600-points*	*300-points*	*600-points*
Earthquake Responses	μ_{fit}	93.26	94.06	90.55	91.98
	σ_{fit}	4.01	2.34	4.87	3.03
White Noise Response	μ_{fit}	82.91	83.65	80.84	82.31
	σ_{fit}	5.57	4.34	6.21	4.41

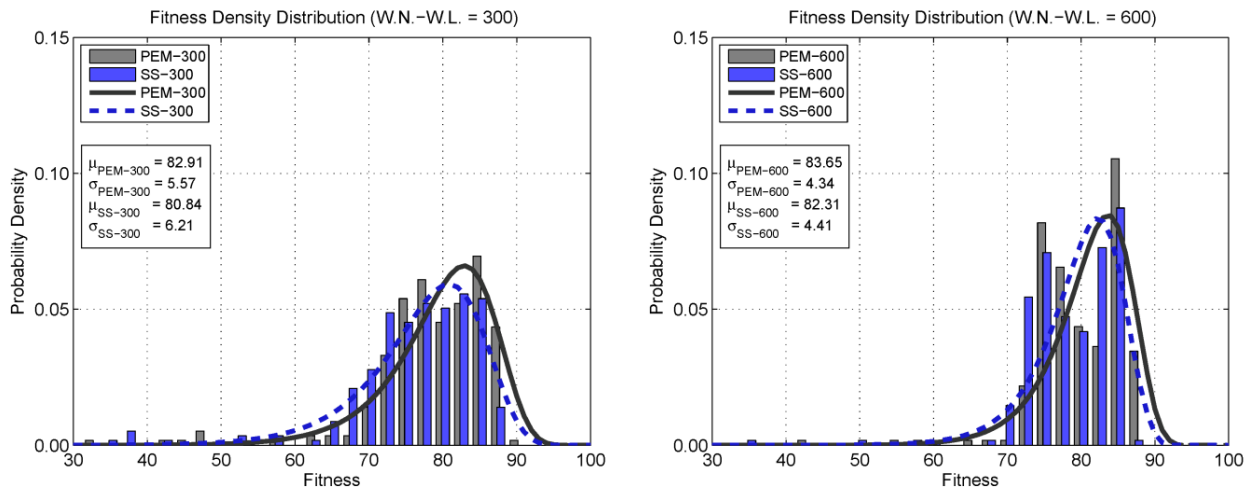

(a) (b)

Figure 3–44 Fitness distribution for white noise responses (a) 300-point (b) 600-point window

As the last step, modal data identified from stable segments of the response of the bridge are investigated. The comparison of the modal data identified from the stable segments with the values extracted from white noise excitations which excited the specimen at the same damage state shows that (1) modal shapes identified from both types of motions are in a very good agreement (last column of table 3-6 through table 3-11), (2) natural frequencies identified from white noise excitations are slightly higher than the values identified from stable segments of the response to earthquake excitations (specially during low-damage states of the bridge) which could be interpreted as a result of lower amplitude levels during white noise excitations which lead to the closure of cracks and stiffer behavior of the reinforced concrete elements.

The comparisons of the modal data from prediction-error and subspace methods are presented in figure 3–45. In most of the cases, identified natural frequencies and mode shapes from both methods are in good agreement. In order to make a choice between the results of two methods for the next step of health monitoring and damage assessment procedure the fitness of fitted models using these methods are compared (figure 3–46).

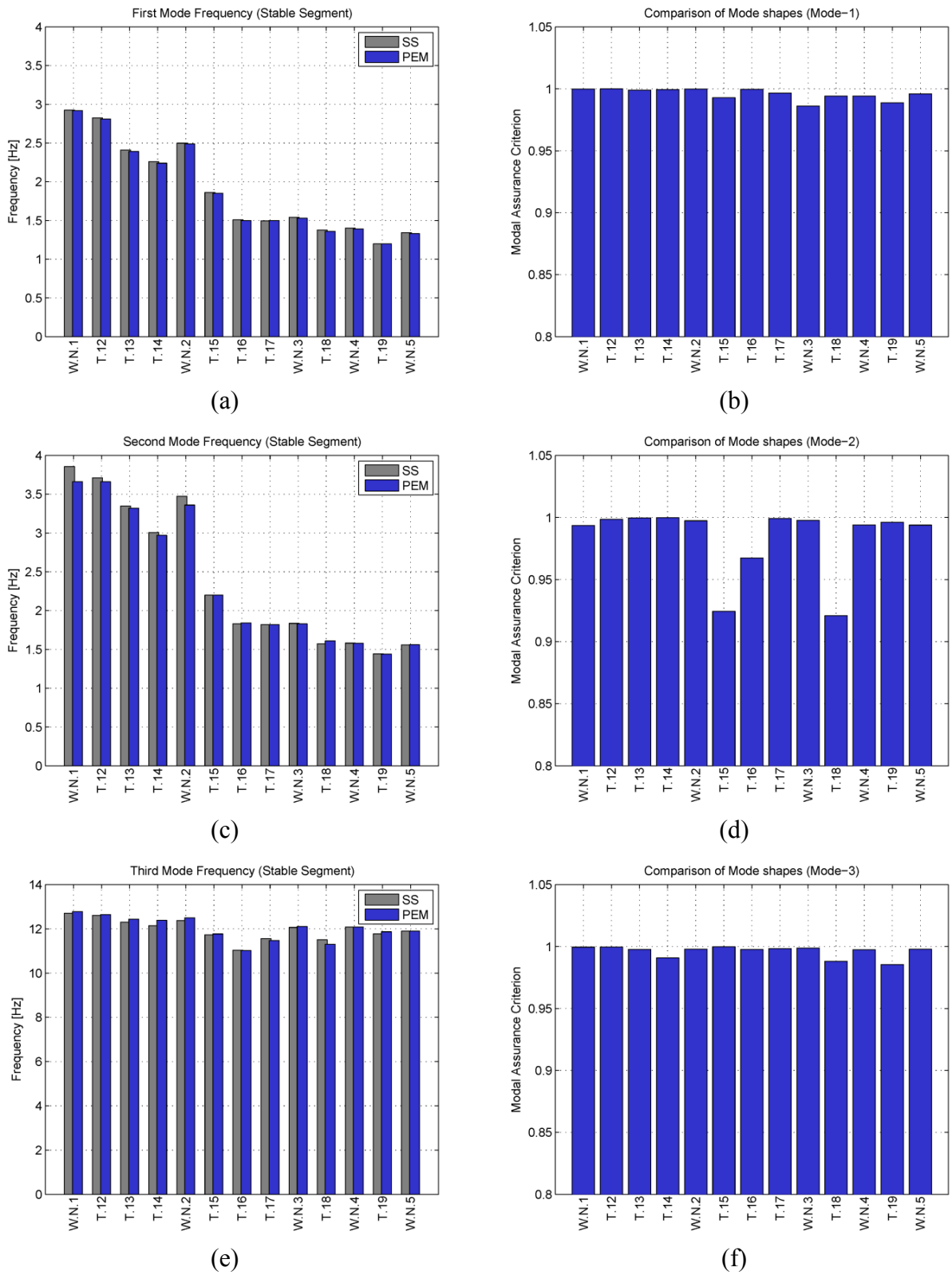

Figure 3–45(a, c, e) Comparison of natural frequencies identified from stable segments of the response (b, d, f) MAC values between mode shapes identified from two approaches

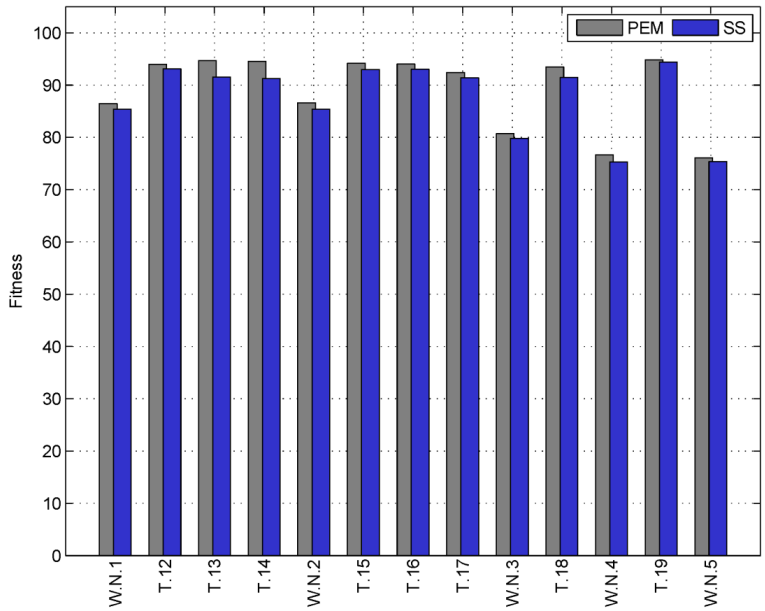

Figure 3–46 Fitness of state-space models identified from stable segments of the response

As presented in figure 3–46, the fitness values of the state space models identified by prediction-error method are generally higher than the fitness of the models identified using subspace methods. As a result, modal data identified from the prediction error system identification technique are used in the following chapters of this report. Although, higher computational efficiency of the stochastic subspace method, make that more suitable for time-frequency analysis which involves significant number system identification runs.

CHAPTER 4

DAMAGE ASSESSMENT THROUGH FINITE ELEMENT MODEL UPDATING

4.1 Background

The problem of FE model updating can be formulated as an optimization problem with the objective of minimizing the error between measured and analytical responses of the structure. In this study, two objective functions are defined using time and modal domains. In time domain, the objective function is defined as the summation of normalized errors between measured and analytical acceleration responses at different sensor locations. In modal domain, weighted errors between experimental and analytical modal frequencies and shapes are utilized for formulation of the objective function. For accurate identification of FE model parameters, a hybrid optimization strategy is proposed and implemented. The optimization strategy takes advantage of global and local search techniques to guarantee the convergence to the global minimum of the objective function. First, the GA is applied for global search of the parameter space using its robust global search capabilities. A local search algorithm, named as quasi-Newton optimization technique, is subsequently utilized for fine tuning of the final population of individuals obtained by the GA. At the final stage of the optimization procedure, the fittest individual with the least

objective value is selected as the best solution. Figure 4–1 presents the details of the proposed optimization strategy. Details of the GA optimization technique, utilized objective functions and damage assessment results are presented in the following subsections.

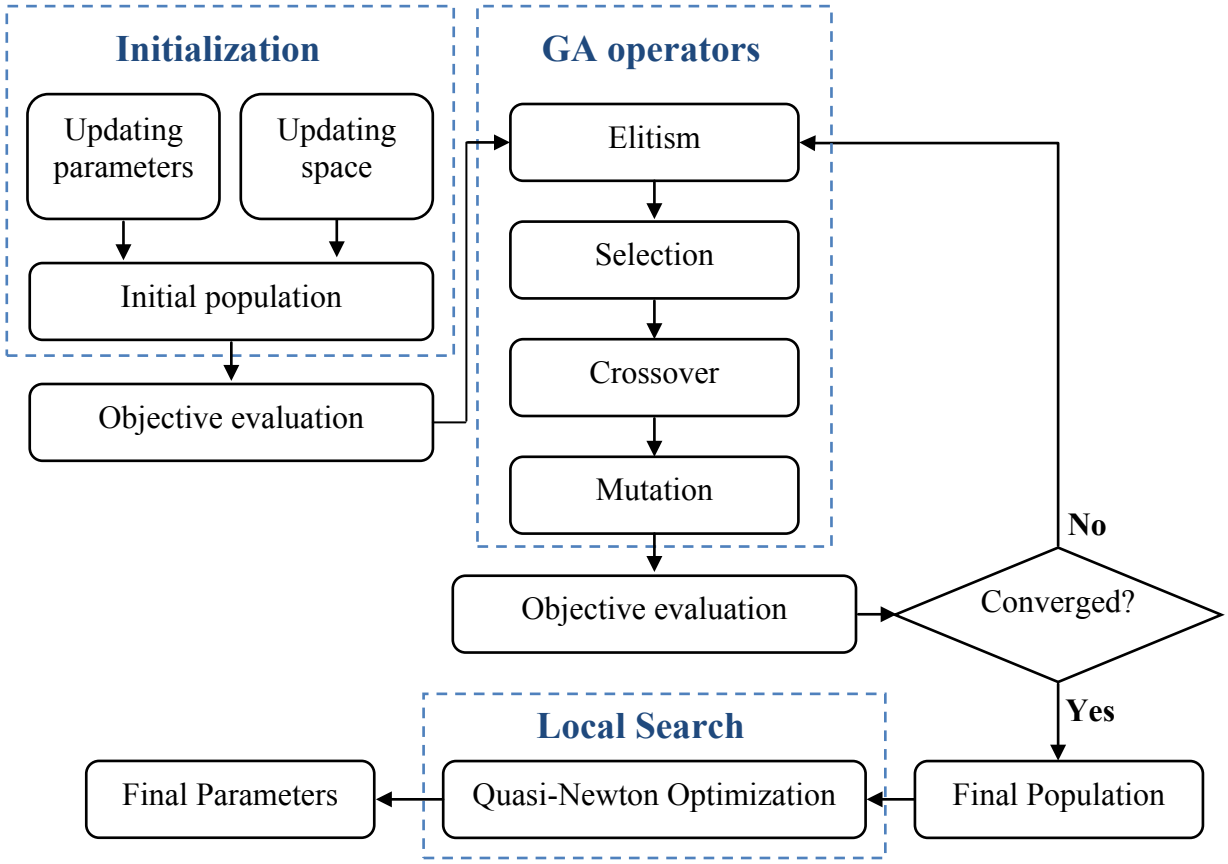

Figure 4–1 Flow chart of implemented optimization strategy

4.2 Genetic Algorithm (GA)

The GA optimization technique is a stochastic search algorithm based on heuristic concepts of natural evolution. The motivation behind the application of GA as an optimization technique is the great success of natural evolution in solving complex optimization problems such as development of new species and their adaptation to drastically changing environmental conditions. Unlike conventional optimization techniques that require a good initial guess of the

solution, GA relies on a population of randomly generated individuals. By conducting a population-to-population search, GA is significantly more likely to converge to the global optimum of the objective function; Moreover, it does not require any information about the derivatives of the objective function, which makes it suitable for discontinuous, non-differentiable, stochastic or highly non-linear problems involving many parameters. The algorithm takes advantage of bio-inspired genetic operators such as crossover and mutation to improve the individuals of the current population and generate a new population with higher fitness level. The steps that are involved in a common GA optimization scheme are:

1. Choose an initial population of S individuals (parameter points): $\Theta_0 = [\theta_{1,0}, \theta_{2,0}, \ldots, \theta_{S,0}]$.
2. Evaluate the fitness of all individuals of the initial population: $Fit(\Theta_0)$.
3. Iterate for $k = 1, 2, \ldots$.
4. Perform selection $\Theta_{new} = Select(\Theta_{k-1})$.
5. Apply genetic operators $\Theta_k = GenOps(\Theta_{new})$.
6. Test for the termination criteria and either go to step 3 or stop[57].

Brief reviews of common GA operators are presented in the following subsections:

4.2.1 Selection

With this operation, individuals are selected for reproduction of future populations based upon their fitness values (inverse of error, loss or objective function values). Selection is a very important step within GA. Although the quality of an individual is measured by its fitness value, but if selection involves only the most highly fit individuals the solution space may be very limited due to the lack of diversity. On the other hand, random selection without considering the

fitness of the individuals does not guarantee that future generations will improve in fitness. Therefore, selection operator performs the delicate task of adjustment of probability of selection of each individual based on its relative fitness to the whole population and selecting the parents of the next generation through a consistent procedure. Numerous selection functions have been proposed and implemented by different researchers. In this study, Tournament selection operator is utilized which selects each parent by successively choosing a preset number of individuals from the population at random and then choosing the best individual out of that set to be a parent of the next generation.

4.2.2 Crossover

The crossover is the most important operator within GA. This operator switches randomly selected chromosomes (parameters values) of two previously selected parent individuals, to produce two new individuals for the new generation. Therefore, the crossover does not create new material (parameter value) within the population; it simply inter-mixes the existing population. The usual schemes to generate new individuals are single-point, multi-point, scattered crossover. In this study, scattered crossover function is utilized. The function creates a random binary vector with the same length as the individuals. It then selects each gene from the either first or second parent based on the value of the corresponding element in the randomly generated vector.

4.2.3 Mutation

The mutation operator introduces a change in one or more of the genes (parameters) of each individual. Therefore, with this operator new material is introduced to the population. As a result, it provides genetic diversity within the population and enables the genetic algorithm to search a broader space. Gaussian mutation operator, developed under Matlab's optimization toolbox, is

utilized to introduce perturbations within the genes of individuals. The operator adds a random number taken from a zero-mean Gaussian distribution to the individual's parameter value. As the generations pass by, the algorithm gradually shrinks the standard deviation of the distribution in order to improve the local search and fine tuning capabilities of the GA.

4.2.4 Elitism

The elitism is an operator which ensures that the most highly fit individuals of the population are directly passed on to the next generation without being altered by other genetic operators. Using elitism ensures that the minimum fitness of the population can never reduce from one generation to the next. Elitism usually brings about a more rapid convergence of the population and in many applications elitism improves the chances of locating an optimal individual.

4.3 Formulation of Objective Functions

As stated earlier, the FE model updating problem can be formulated as a constrained optimization problem to find the optimal set of model parameters ($\hat{\mathrm{B}}$) which minimizes the objective function (J), defined as a function of the error between measured responses of the physical structure with the responses predicted by the FE model of the structure:

$$\begin{aligned} &J\left(\hat{\mathrm{B}}\right) \le J\left(\mathrm{B}\right) \qquad \forall \mathrm{B} \\ &\mathrm{B} = \{\beta_1, \beta_2, \cdots, \beta_N\} \qquad \beta_{li} \le \beta_i \le \beta_{ui} \end{aligned} \tag{4-1}$$

Here, β_i's are the FE model parameters, N is the total number of model parameters to be updated, and β_{li} and β_{ui} are the lower and upper bounds for the ith model parameter, respectively. In this study, depending on the data type used for the model updating, the FE model parameter set (B) is defined as a combination of correction factors for the stiffness of structural components and Rayleigh damping coefficients. Two objective functions are defined using

modal and time domain data. In modal domain, the objective function is defined as the summation of weighted errors in frequencies and mode shapes of the dominant modes of vibration of the structure.

$$J_1 = \sum_{i=1}^{n_d} \left(W_{fi} \Delta f_i + W_{\varphi i} \left(1 - MAC_i \right) \right) \tag{4-2}$$

Here, n_d is the number of dominant modes of vibration of the structure; W_{fi} and $W_{\phi i}$ are the relative weights assigned to error in natural frequency and mode shape of the ith mode of vibration of the structure. Details of the weight adjustment procedure are presented in the following subsection. Relative error in frequency (Δf_i) and modal assurance criterion (MAC_i) are defined as:

$$\Delta f_i = \left| \frac{f_i^e - f_i^a}{f_i^e} \right| \tag{4-3}$$

$$MAC_i = \frac{\left(\left(\phi_i^e \right)^T . \left(\phi_i^a \right) \right)^2}{\left(\left(\phi_i^e \right)^T . \left(\phi_i^e \right) \right) . \left(\left(\phi_i^a \right)^T . \left(\phi_i^a \right) \right)} \tag{4-4}$$

where f_i and ϕ_i represent i^{th} natural frequency and mode shape of the structure; superscripts e and a correspond to experimental and analytical dynamic properties respectively.

The second objective function is defined as the summation of normalized errors between measured and simulated acceleration responses at different sensor locations on the structure:

$$J_2 = \sum_{k=1}^{n_m} \frac{\left(y_k^e - y_k^a \right)^T . \left(y_k^e - y_k^a \right)}{\left(y_k^e \right)^T . \left(y_k^e \right)} \tag{4-5}$$

Here, n_m is the number of measurement channels intended to be used for model updating and y_k represents the response at the kth measurement location. In the definition of J_2, errors between

FE model simulated and measured responses at each sensor location are normalized by the total power of the measured signal at the same location. Such normalization scheme will prevent the FE model updating process to over-fit the response at the locations with higher amplitude levels (higher absolute error values) and produce poor fits for the low-amplitude channels.

The first objective function (J_1) could be applied for damage assessment of the bridge specimen from modal data identified from either white noise or stable segment of the earthquake excitation; but the application of second objective function (J_2) is limited to the linear responses of the bridge during white noise excitations or low-amplitude earthquakes.

Adjustment of Weights

The weighting factors ($W_{fi}, W_{\phi i}$) in equation (4-2) are calculated based on two main parameters: (1) relative importance of each mode of vibration in the total response of the structure and (2) reliability of the measured dynamic parameters. There are two factors that control the relative importance of any mode in the total dynamic response of the structure: (1) the modal participation factor (MPF) which depends on the interaction of the mode shape with spatial distribution of the external load and (2) the dynamic magnification factor that depends on the ratios of the applied loading harmonic frequencies to the modal frequency [58]. Therefore, the weighting factors ($W_{fi}, W_{\phi i}$) are calculated as the product of two factors representing the relative importance of each mode of vibration in the total response (W_i) and the reliability of the measured dynamic parameters (W_d). The relative importance of each mode is estimated using the transfer function of identified natural modes. The decoupled transfer function corresponding to each mode is defined as:

$$G_i(z) = \frac{c_i b_i}{z - \lambda_i} \tag{4-6}$$

Where λ_i is the ith eigenvalues of the identified state matrix , $\mathbf{A}$, b_i is the ith row of the input matrix, $\mathbf{B}$,and c_i is the ith column of output matrix, $\mathbf{C}$. The relative importance of each mode is calculated as the ratio between the H_2 norm of the decoupled transfer function corresponding to that mode and sum of the H_2 norms of significant modes of vibration:

$$W_i = \frac{\|G_i\|}{\sum_{i=1}^{n_d} \|G_i\|} \tag{4-7}$$

$$\|G_i\| = \left(\frac{1}{2\pi} \int_0^{2\pi} tr\left(G_i^*\left(e^{j\theta}\right) G_i\left(e^{j\theta}\right)\right) d\theta \right)^{1/2} \tag{4-8}$$

here $tr(.)$ denotes the sum of diagonal elements of the matrix and * represents the conjugate transpose. As stated earlier, relative importance of the each modal parameter is used for adjustment of the weight assigned to error in the respective parameter. However, these values are subject to change during the experiment, because of structural damage and change in dynamic properties of the bridge. For consistency of FE model updating results, average values of (0.55), (0.35) and (0.10) are used as relative importance index (W_i) for the first three transverse modes of vibration of the bridge, respectively. The higher reliability and damage sensitivity of natural frequencies in comparison to mode shapes is incorporated into the objective function by assigning higher relative weight (W_d) to the relative error in frequencies (0.67) in comparison to the weight assigned to error in mode shapes (0.33). The final set of weighting factors are presented in table 4-1.

Table 4-1 Weighting factors for J_1

	Mode - 1		Mode - 2		Mode - 3	
Parameter	W_{f1}	$W_{\varphi 1}$	W_{f2}	$W_{\varphi 2}$	W_{f3}	$W_{\varphi 3}$
Value	0.368	0.182	0.234	0.116	0.067	0.033

4.4 Finite Element Model Updating Results

The presented FE model updating procedure is applied for damage assessment of the bridge specimen at different stages of the experiment. As the first step a FE model of the bridge specimen is generated. The baseline values for the stiffness of the critical elements of the bridge and Rayleigh damping ratios are calibrated using the recorded responses from the intact bridge.

4.4.1 FE Model and Calibration

A relatively low-order three dimensional FE model of the bridge is developed using the Open System for Earthquake Engineering Simulation (OpenSees) software framework. The FE model of the bridge is generated using linear elastic beam column elements incorporating the second order P-Delta effects. Geometric data and material properties of the bridge are provided by Nees@Reno research group that conducted the experiment [50]. For FE model updating using the first objective function (J_1) correction factors for the stiffness of the plastic hinge areas of the columns and in-plane bending stiffness of the deck of the bridge are selected as the FE model parameters. For the case of model updating using second objective function (J_2) which involves response history analysis, correction factors for modal damping ratios of the first two transverse modes of vibration of the bridge are added to model parameter set used in the previous case. As the first step for damage assessment, FE model parameters are calibrated using the modal properties extracted from the response of the intact bridge to (W.N.1). These values are used as the baselines for assessment of damage within the bents and the deck of the bridge at various

stages of the experiment. Figure 4–2 compares the experimental modal shapes corresponding to the first three transverse modes of vibration with the modal shapes calculated by the calibrated FE model. The comparison of the measured acceleration response histories with the responses simulated by the calibrated FE model at five sensor locations on the superstructure of the bridge are presented in figure 4–3. The final calibration factors estimated using modal domain and time domain data are presented in table 4-2.

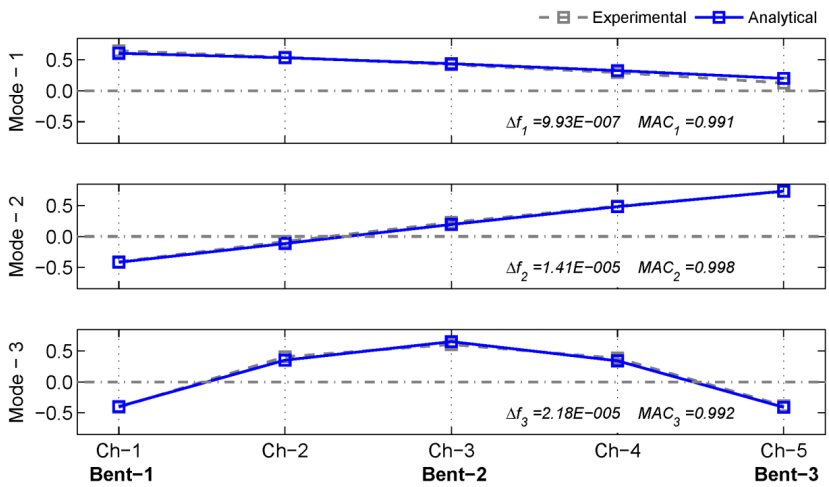

Figure 4–2 Analytical and experimental modal shapes of the bridge specimen (W.N.1)

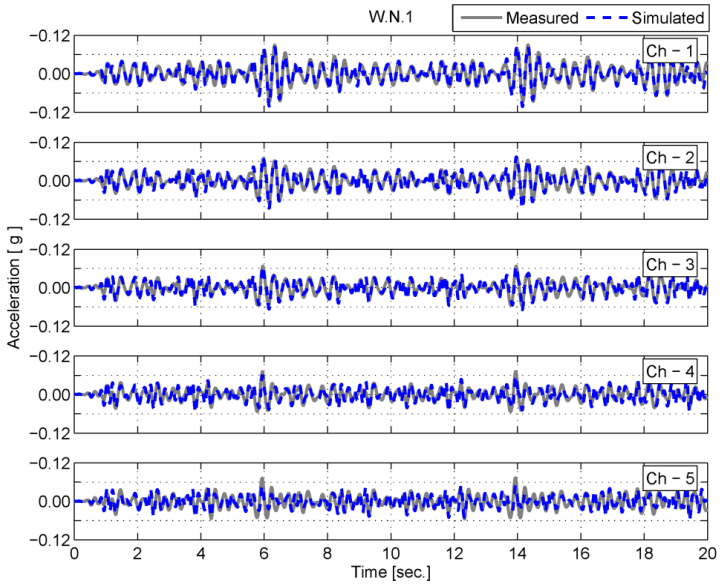

Figure 4–3 Analytical and measured response histories on the superstructure of bridge (W.N.1)

Table 4-2 Calibration factors estimated using modal and time domain data

Objective Function	$\beta_{0,bent-1}$	$\beta_{0,bent-2}$	$\beta_{0,bent-3}$	$\beta_{0,deck}$
J_1	0.761	1.019	0.780	0.983
J_2	0.760	1.048	0.776	0.976

4.4.2 Damage Assessment Results

The presented FE model updating procedure is utilized for damage assessment of the bridge specimen at various stages of the experiment. The modal domain approach (J_1) is performed by matching the analytically calculated modal properties of the bridge with experimental properties identified from the white noises and stable segments of the damaging earthquakes using prediction-error system identification technique (table 3-6, table 3-8 and table 3-10). Table 4-3 presents the identified stiffness correction factors for the bents and deck of the bridge.

Table 4-3 FE model updating results using (J_1): stiffness correction factors

Test	β_{bent-1}	β_{bent-2}	β_{bent-3}	β_{deck}
W.N.1	1.000	1.000	1.000	1.000
Test-12	0.892	1.011	1.022	0.978
Test-13	0.604	0.892	0.851	0.966
Test-14	0.546	0.710	0.669	0.976
W.N.2	0.687	0.819	0.868	0.976
Test-15	0.381	0.482	0.346	0.903
Test-16	0.243	0.331	0.246	0.801
Test-17	0.258	0.274	0.237	0.873
W.N.3	0.267	0.280	0.265	0.974
Test-18	0.243	0.130	0.197	0.855
W.N.4	0.207	0.315	0.172	0.975
Test-19	0.209	0.143	0.124	0.950
W.N.5	0.223	0.130	0.201	0.951

The final values of the relative errors between experimental and analytical frequencies and the MAC values between identified and analytical mode shapes are listed in table 4-4. Comparison of the error levels at different stages of experiment indicate that for the match between analytical and experimental properties of the first and the third modes of the bridge is consistently good over the whole experiment. However, the bias in estimation of second mode properties, especially during the latter stages of the experiment and due to the proximity of the first and second modes frequencies, led to increased error levels for these properties.

Table 4-4 FE model updating results using (J_1): error decomposition

Test	Δf_1	MAC_1	Δf_2	MAC_2	Δf_3	MAC_3
W.N.1	1.852E-07	1.000	1.273E-05	0.999	8.840E-06	0.993
Test-12	1.144E-06	0.985	3.088E-05	0.981	7.303E-06	0.994
Test-13	2.162E-06	0.995	1.044E-05	0.999	3.355E-07	0.993
Test-14	5.671E-07	0.998	7.206E-06	1.000	1.415E-06	0.994
W.N.2	7.536E-06	0.994	2.374E-06	0.990	1.522E-06	0.993
Test-15	1.109E-05	0.988	1.030E-01	0.973	1.803E-04	0.991
Test-16	2.599E-06	0.998	1.306E-05	0.979	3.605E-05	0.977
Test-17	2.499E-06	1.000	1.281E-05	0.988	4.875E-07	0.988
W.N.3	6.767E-05	0.981	2.838E-03	0.968	5.943E-04	0.992
Test-18	4.649E-05	0.986	6.793E-03	0.952	1.785E-06	0.980
W.N.4	7.285E-06	1.000	3.021E-02	0.988	2.053E-05	0.994
Test-19	4.457E-05	0.964	6.952E-03	0.930	1.853E-06	0.954
W.N.5	7.491E-06	0.970	2.933E-02	0.959	2.033E-05	0.977

As stated earlier, due to linearity assumption of the implemented procedure, the FE model updating procedure using time domain data is only applied to response measurements during white noise excitations. Identified stiffness correction factors of the bents and superstructure of the bridge along with modal damping ratios of the first two transverse modes of vibration and the fitness values of the fittest individual of the last GA population are presented in table 4-5. The

comparisons of the measured and simulated acceleration response histories on the superstructure of the bridge specimen are presented in figure 4–4 through figure 4–7.

Table 4-5 FE model updating results using (J_2)

Test	β_{bent-1}	β_{bent-2}	β_{bent-3}	β_{deck}	ζ_1	ζ_2	*fit*
W.N.1	1.000	1.000	1.000	1.000	3.9%	5.3%	0.963
W.N.2	0.735	0.800	0.773	0.955	5.3%	5.5%	0.951
W.N.3	0.231	0.352	0.211	0.961	4.9%	5.0%	0.906
W.N.4	0.225	0.249	0.171	0.944	4.7%	4.8%	0.845
W.N.5	0.193	0.201	0.163	0.939	4.7%	4.8%	0.822

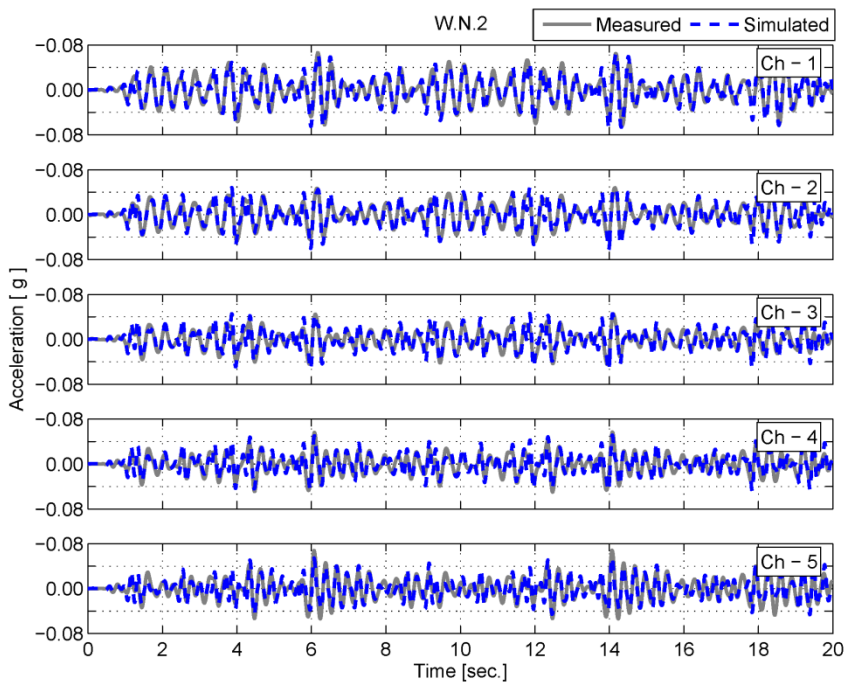

Figure 4–4 Analytical and measured response histories on the superstructure of bridge (W.N.2)

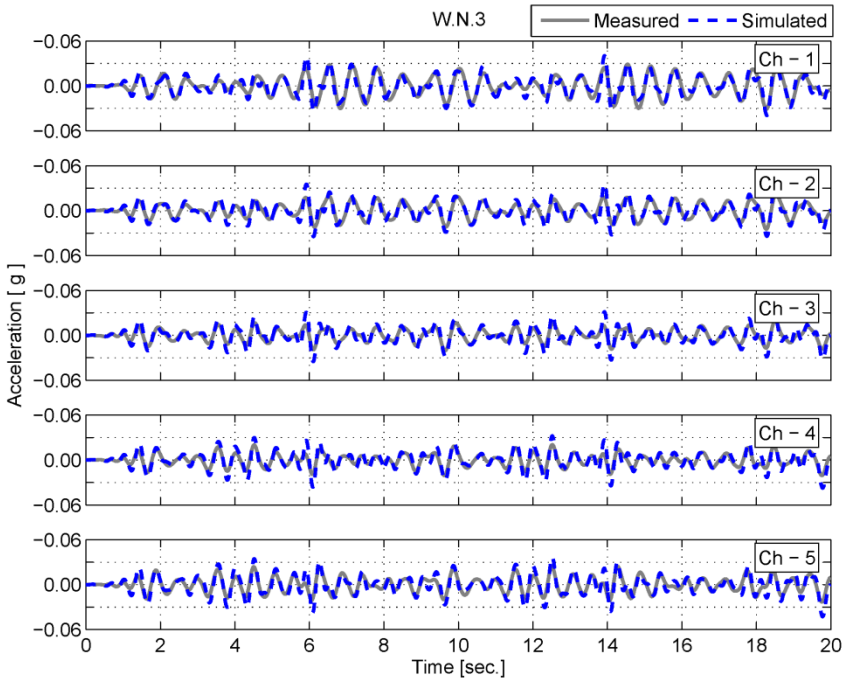

Figure 4–5 Analytical and measured response histories on the superstructure of bridge (W.N.3)

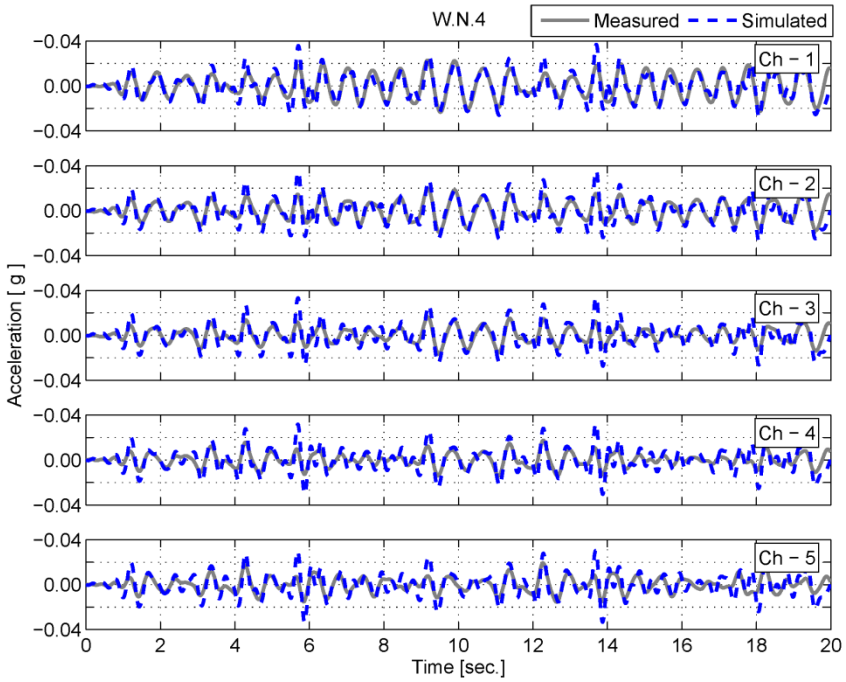

Figure 4–6 Analytical and measured response histories on the superstructure of bridge (W.N.4)

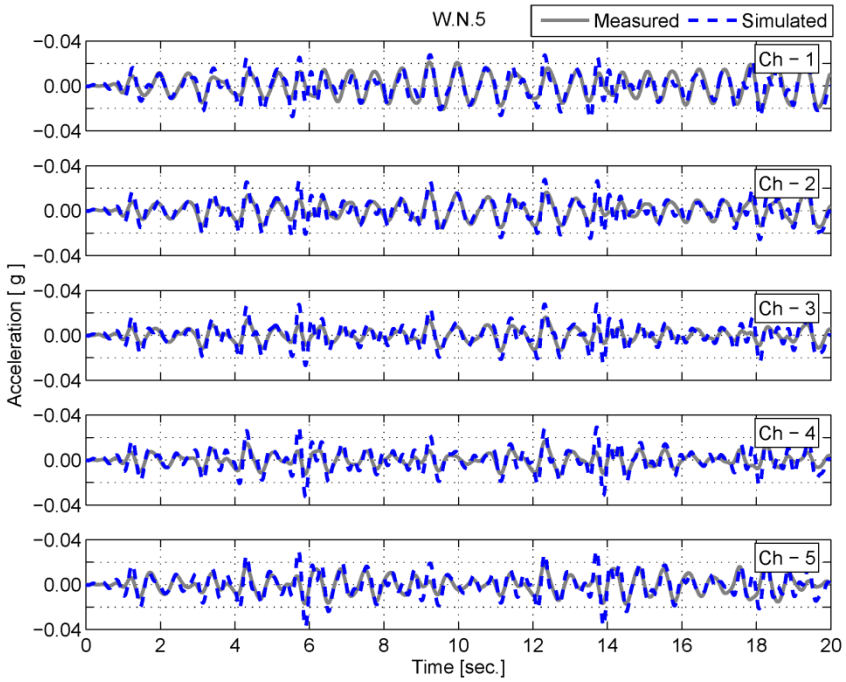

Figure 4–7 Analytical and measured response histories on the superstructure of bridge (W.N.5)

As it presented in table 4-5 and even apparent from response history comparison figures, the quality of match between the analytical and measured acceleration response histories decreases drastically after second white noise input. This could happen as a result of lower structural response level hence lower signal-to-noise ratios (SNRs) of the measurements during the latter tests of the experiment. In order to check the validity of this claim, SNR values of the response measurements to white noise excitations are estimated. The SNR is estimated by calculating the noise power over a frequency range that neither input excitation nor bridge specimen can contribute to measurements in that frequency range. Considering the frequency content of the input white noise excitation and dynamic properties of the bridge specimen, the total power of the measurements over [30~50 Hz] range is considered as measurement noise. The noise power is then generalized to the whole frequency range assuming uniform noise power over the whole frequency range (white noise). Figure 4–8 compares the average SNR values for measured

signals on the superstructure of the bridge at different stages of experiment. The figure has two ordinate axes representing the SNR and second objective function J_2 values.

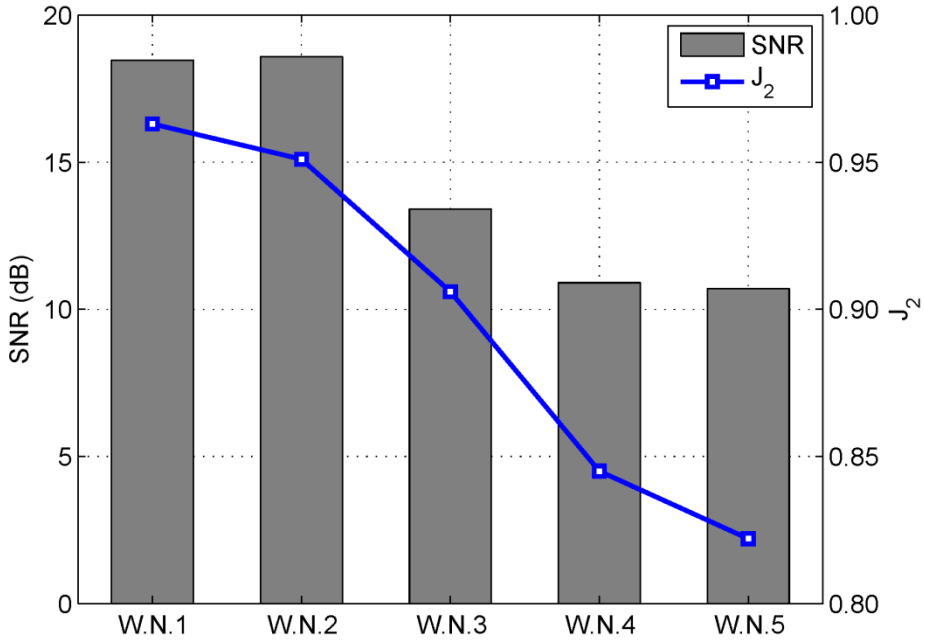

Figure 4–8 Estimated average SNRs for measured signals during white noise excitations

The results of analysis show the close correlation between the SNR values and time domain based FE model updating procedure performance (J_2). Identified stiffness correction factors for the bents and the deck of the bridge are compared and validated in the following section.

4.4.3 Validation of the Results

In general, experimental force-displacement relationships are used for the estimation of the stiffness and damping properties of the laboratory tested columns. The relative displacement is typically measured using displacement transducers installed at the top and the bottom of the column and the force is measured using load cells. Since there is no practical solution for including a load cell into the columns of the tested bridge system, acceleration responses

recorded at the top of the bents are used as indicators of the shear force acting on the bents of the bridge. Implicit in this approach is the assumption that the inertial forces applied to each bent are proportional to the tributary mass and the acceleration recorded at the top of the bent.

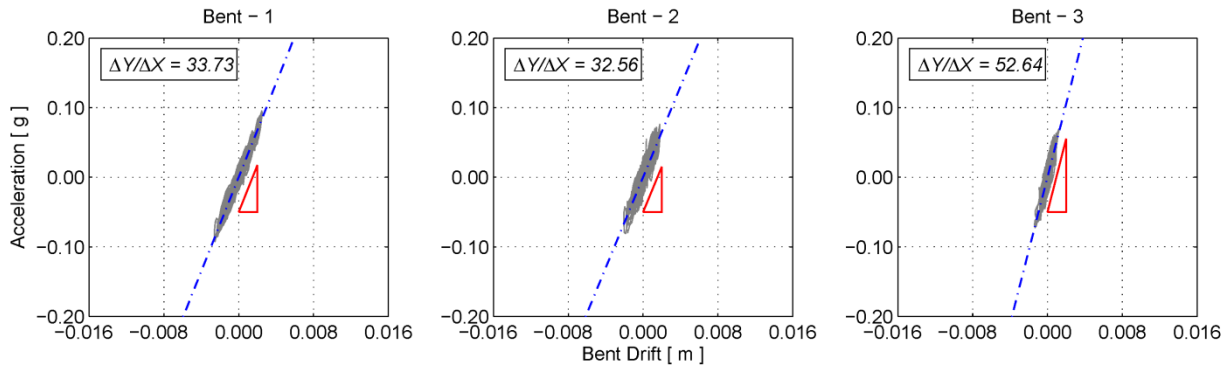

Figure 4–9 Acceleration-drift relationships of the bents of the intact bridge specimen (W.N.1)

Figure 4–9 shows the lateral acceleration-drift relationships of for the bents of the bridge specimen during (W.N.1) when the bridge is in intact condition. Lateral drifts of the bents are calculated using displacement measurements at the top and bottom of the bridge. A linear regression technique is applied to estimate the average slope of the curves. Ignoring the effects of damping forces and the interaction between the bents in dynamic equilibrium equation of each bent, the average slopes of the curves are proportional to the stiffness of the bents. As a result, changes in lateral stiffness of the bents could be tracked by calculation of these values at different stages of experiment. For white noise excitations, the slopes are calculated for the full length of the recorded signals but in the case of damaging earthquakes, the stable segments of the response identified during modal identification procedure (explained in previous chapter) are used for calculation of the average slopes. For comparison purposes, the average slopes calculated at each stage of the experiment are normalized by the values found during (W.N.1). The average slopes of the curves and corresponding normalized values (β_e) for are presented in figure 4–10 through figure 4–12 and table 4-6 through table 4-8.

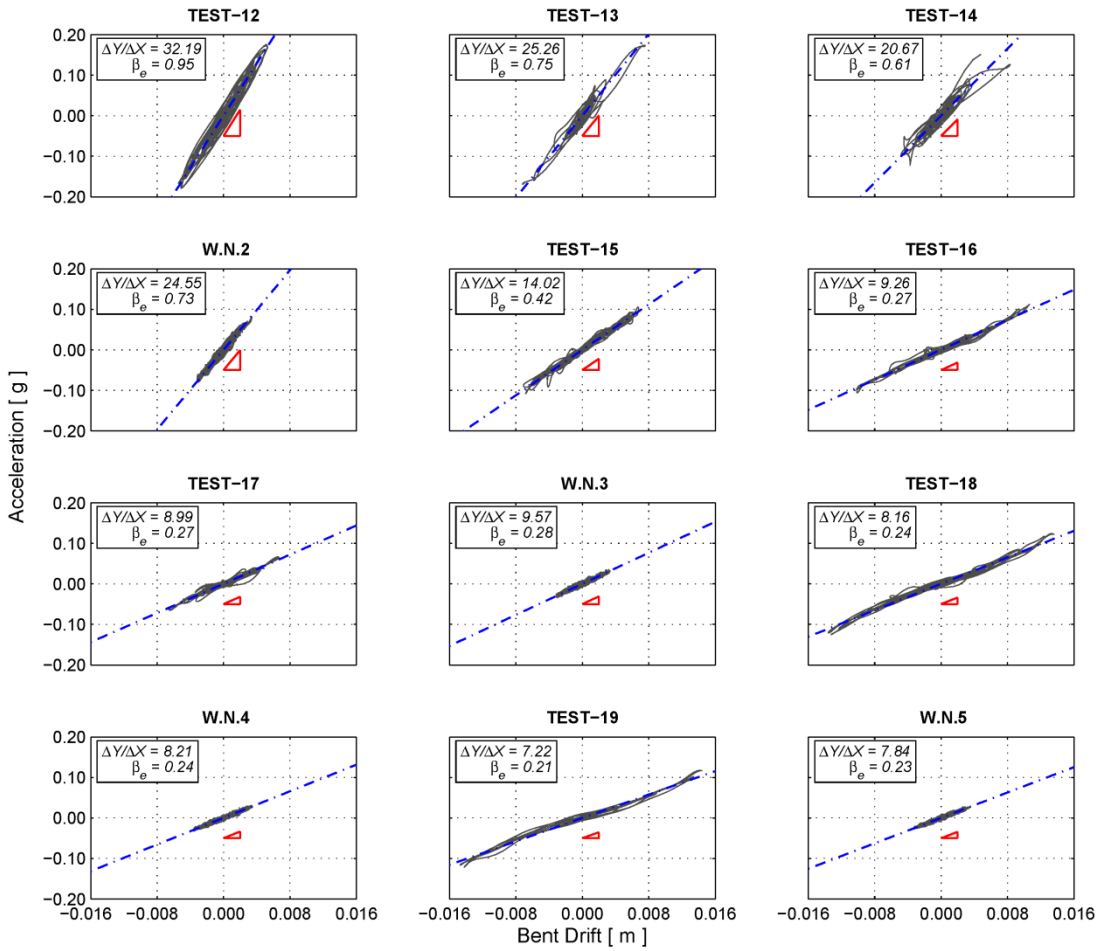

Figure 4–10 Acceleration-drift relationships for Bent-1

Table 4-6 Average slopes and experimental stiffness indices (Bent-1)

Test	$\Delta Y / \Delta X$	β_e	Test	$\Delta Y / \Delta X$	β_e
W.N.1	33.73	1.00	Test-17	8.99	0.27
Test-12	32.19	0.95	W.N.3	9.57	0.28
Test-13	25.26	0.75	Test-18	8.16	0.24
Test-14	20.67	0.61	W.N.4	8.21	0.24
W.N.2	24.55	0.73	Test-19	7.22	0.21
Test-15	14.02	0.42	W.N.5	7.84	0.23
Test-16	9.26	0.27			

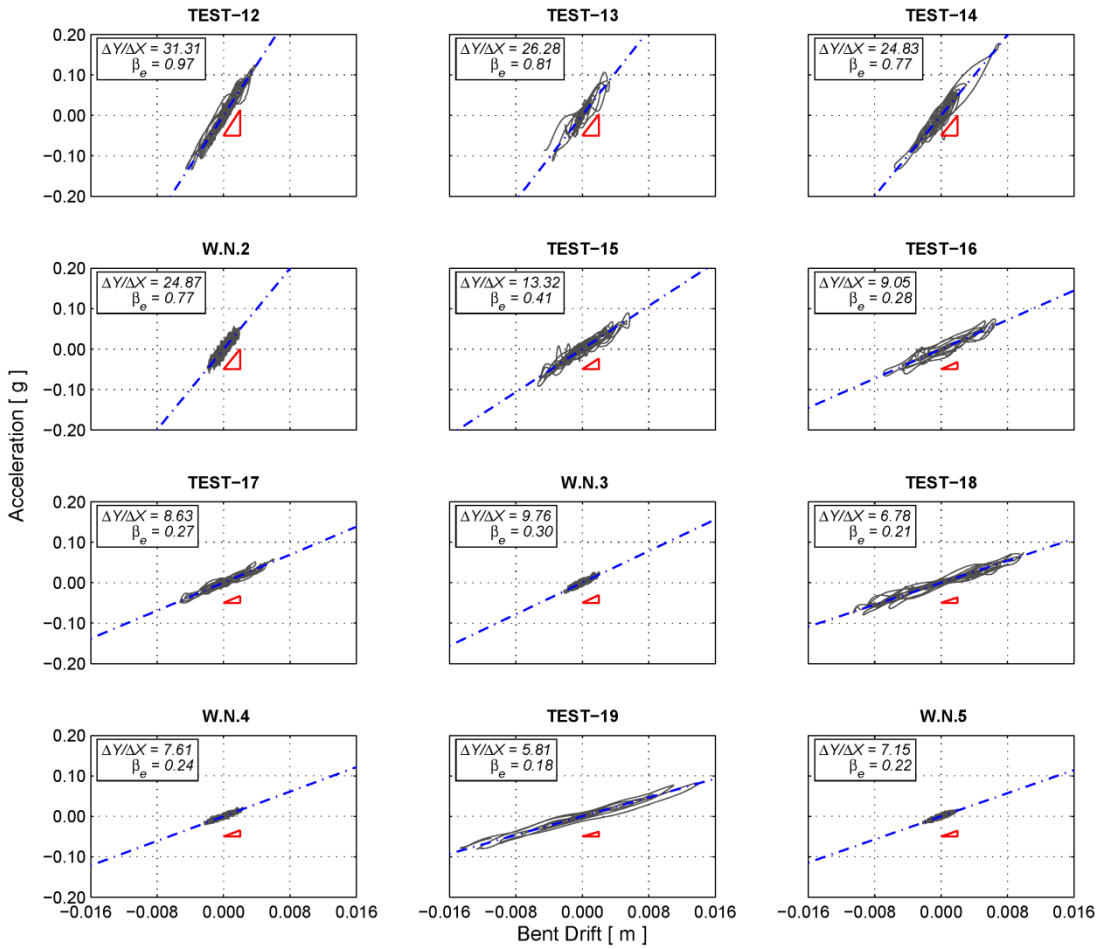

Figure 4–11 Acceleration-drift relationships for Bent-2

Table 4-7 Average slopes and experimental stiffness indices (Bent-2)

Test	$\Delta Y/\Delta X$	β_e	Test	$\Delta Y/\Delta X$	β_e
W.N.1	32.56	1.00	Test-17	8.63	0.27
Test-12	31.31	0.97	W.N.3	9.76	0.30
Test-13	26.28	0.81	Test-18	6.78	0.21
Test-14	24.83	0.77	W.N.4	7.61	0.24
W.N.2	24.87	0.77	Test-19	5.81	0.18
Test-15	13.32	0.41	W.N.5	7.15	0.22
Test-16	9.05	0.28			

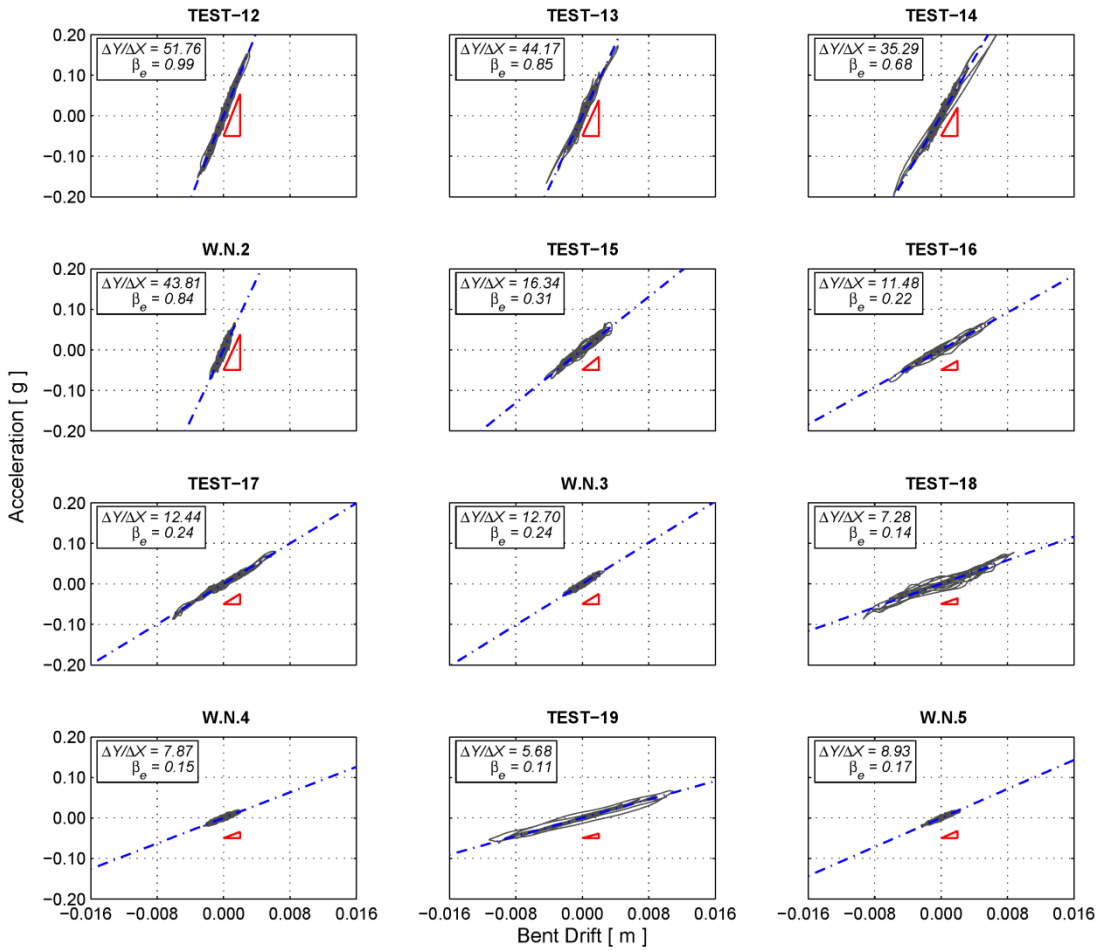

Figure 4–12 Acceleration-drift relationships for Bent-3

Table 4-8 Average slopes and experimental stiffness indices (Bent-3)

Test	$\Delta Y/\Delta X$	β_e	Test	$\Delta Y/\Delta X$	β_e
W.N.1	52.64	1.00	Test-17	12.44	0.24
Test-12	51.76	0.99	W.N.3	12.70	0.24
Test-13	44.17	0.85	Test-18	7.28	0.14
Test-14	35.29	0.68	W.N.4	7.87	0.15
W.N.2	43.81	0.84	Test-19	5.68	0.11
Test-15	16.34	0.31	W.N.5	8.93	0.17
Test-16	11.48	0.22			

The stiffness correction factors of the bents identified using modal (J_1) and time (J_2) data are compared with experimental stiffness indices in figure 4–13 through figure 4–15. The experimental indices are generally in good agreement with the FE model updating results except for correction factors for Bent-1 during Test-13 and Test-14 where the modal frequencies and experimental stiffness indices were found highly sensitive to the choice of start point of stable segment of the response. This highlights the fact that, despite the enormous amount of effort that is being made to bundle the vibration-based health monitoring and damage assessment techniques into fully automated black-box modules, engineering judgment practiced by professionals is an integral part of these techniques that still plays a key role in condition assessment of the structures.

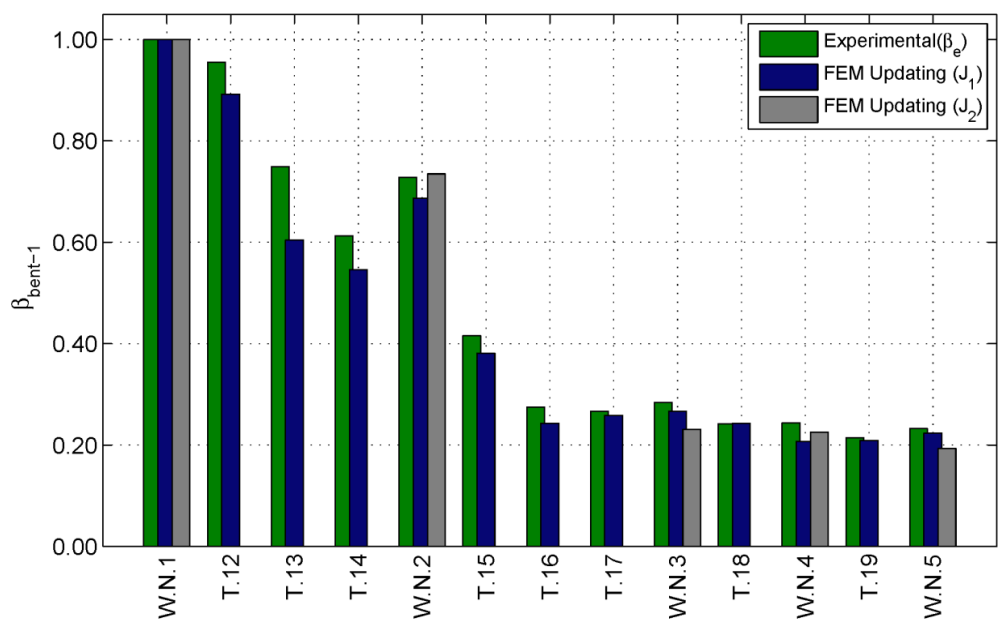

Figure 4–13 Stiffness correction factors (Bent-1)

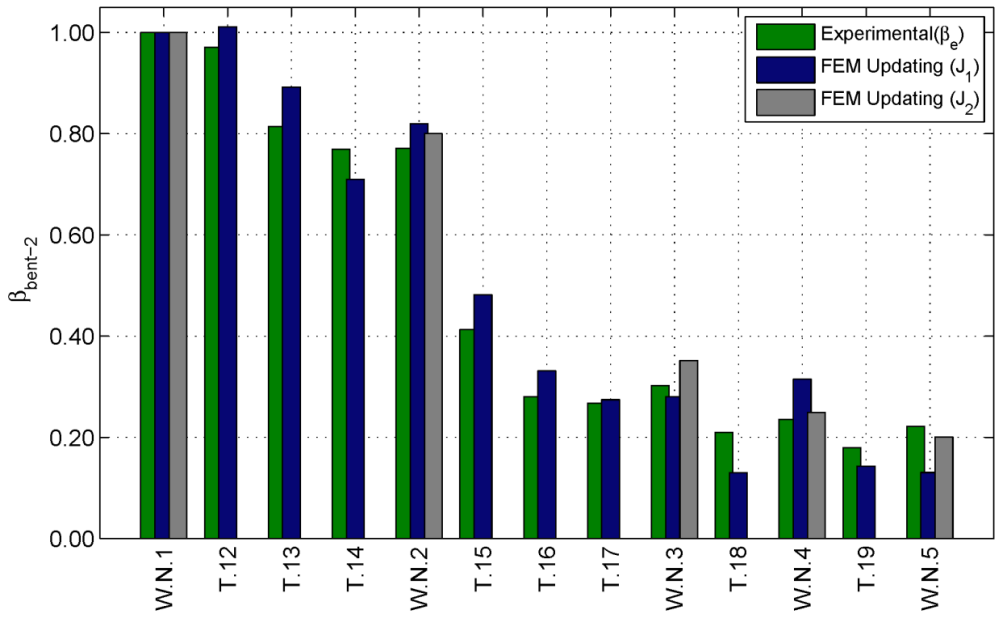

Figure 4–14 Stiffness correction factors (Bent-2)

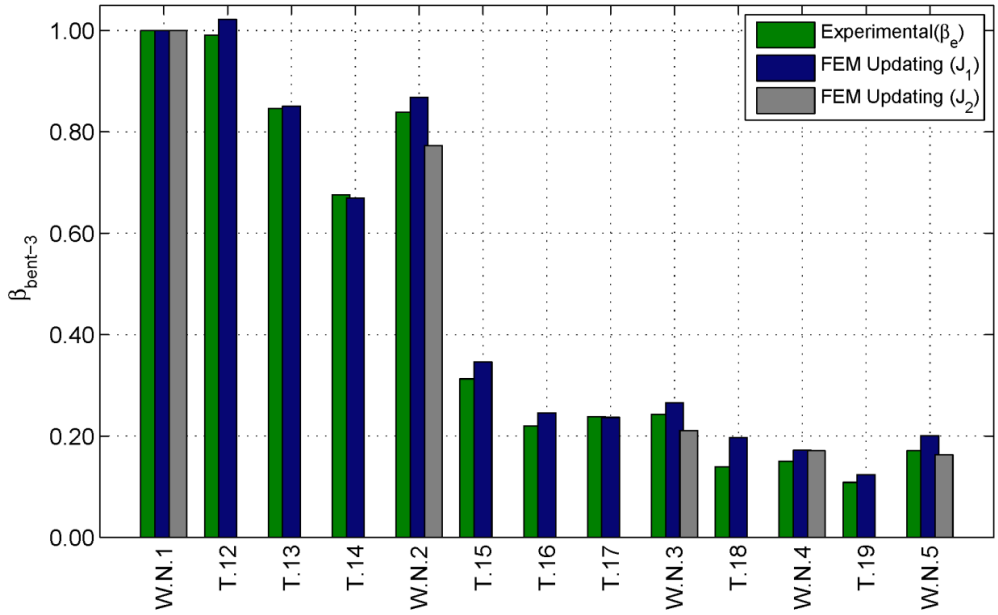

Figure 4–15 Stiffness correction factors (Bent-3)

The stiffness correction factors of the deck of the bridge specimen identified using modal (J_1) and time (J_2) domains data are compared in figure 4–16. The identification results show small variations in the stiffness of the deck of the bridge during the whole experiment which is quite

consistent with the visual inspection results that indicated almost no damage within the deck of the bridge at the end of the experiment.

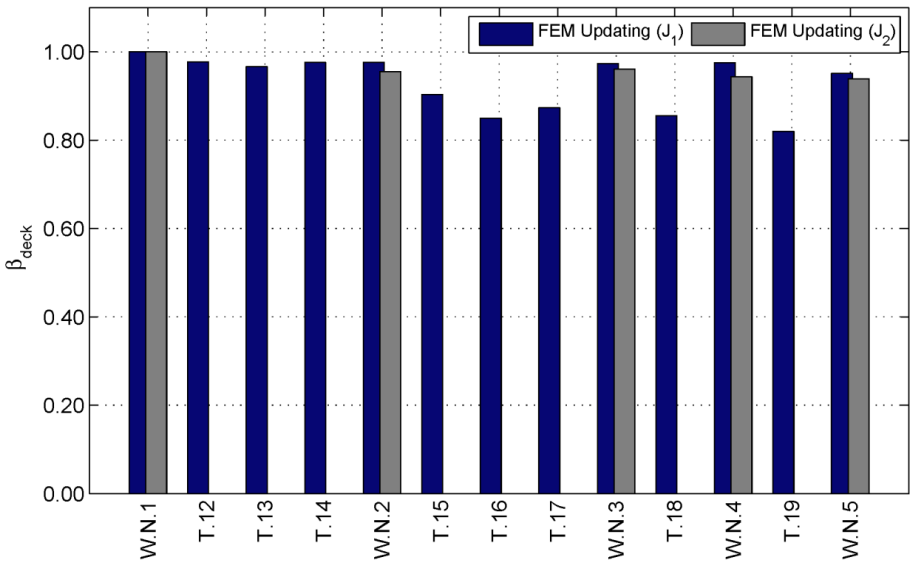

Figure 4–16 Stiffness correction factors (Deck)

The comparison of the experimental analytical results show that, FE model updating using either modal domain or time domain data can produce accurate and reliable damage assessment results even in the presence of measurements noise and for complex structures with close vibration modes. The next chapter of this report addresses the fourth level of damage assessment hierarchy by investigating the consequences of damage in the current and future operation of the bridge.

CHAPTER 5

RESIDUAL COLLAPSE CAPACITY ESTIMATION

5.1 Background

In this study, an effort has been made to bridge the gap between the vibration-based damage assessments techniques with the residual capacity estimation methods developed within performance based earthquake engineering framework. Two vibration-based procedures have been proposed and applied to incorporate acceleration measurements as the most common and easiest-to-achieve vibration data for estimation of residual collapse capacity and determination of functionality status of the bridge after a major earthquake event. The procedures are tailored to provide bridge officials with information that could improve and expedite the decision making process on whether to permit, restrict or deny access to the bridge after a major damaging event.

The first procedure relies on pushover curves and double-integration technique to estimate the experimental ductility ratios of lateral force resisting elements of the bridge. The ductility-based residual capacity of structural elements could be used to assess the safety of the whole bridge system for public use. The second procedure takes advantage of incremental dynamic analysis (IDA) curves to estimate the collapse capacities of the intact and damaged bridges. Estimated residual capacity of the bridge together with bridge-site-specific hazard curves are used to update

the functionality status of the bridge. Details of the proposed procedures are discussed in the following sections as they are applied to vibration measurements during the shake table experiment on the bridge specimen.

5.2 Ductility-based Residual Capacity Estimation Using Acceleration Data

The outline of the ductility-based residual capacity estimation method is presented in figure 5–1.

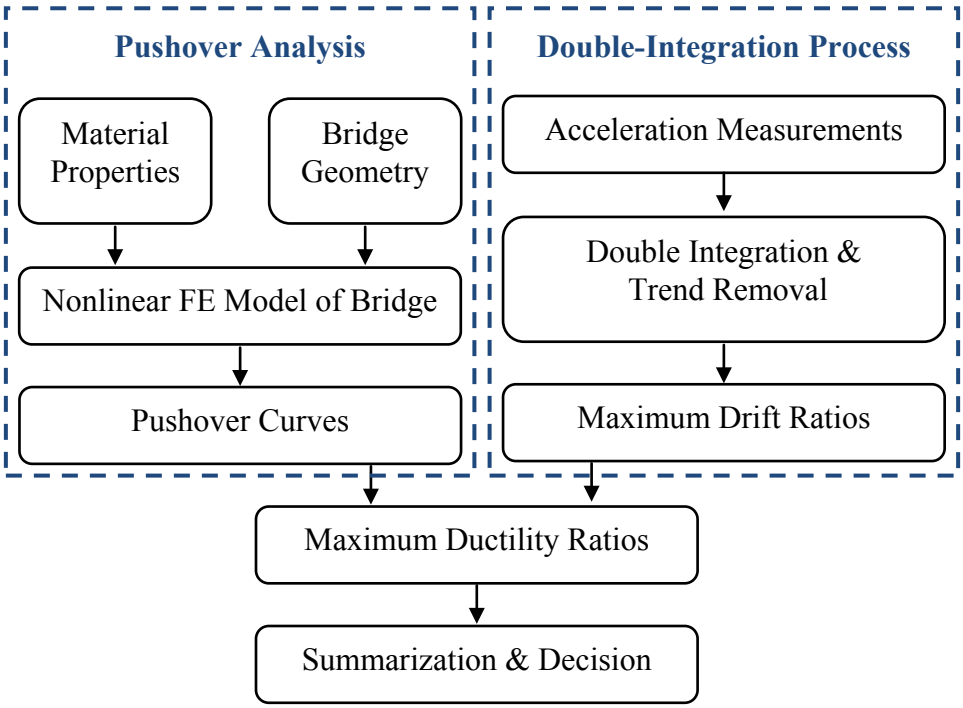

Figure 5–1 Flowchart of ductility-based residual capacity estimation method

5.2.1 Pushover Analysis of Bents of the Bridge Specimen

As the first step of the analysis, nonlinear FE models of the bents as the only lateral force resisting subsystems of the bridge are generated. The Opensees software framework is utilized for FE model generation and static pushover analysis of the bents. The section properties of the columns of the bents are modeled using fiber sections with concrete02 and reinforcing steel material models (figure 5–2). The results of material testing procedures, reported in CCEER06-02 [50], are utilized to accurately capture the nonlinear behavior of the bents.

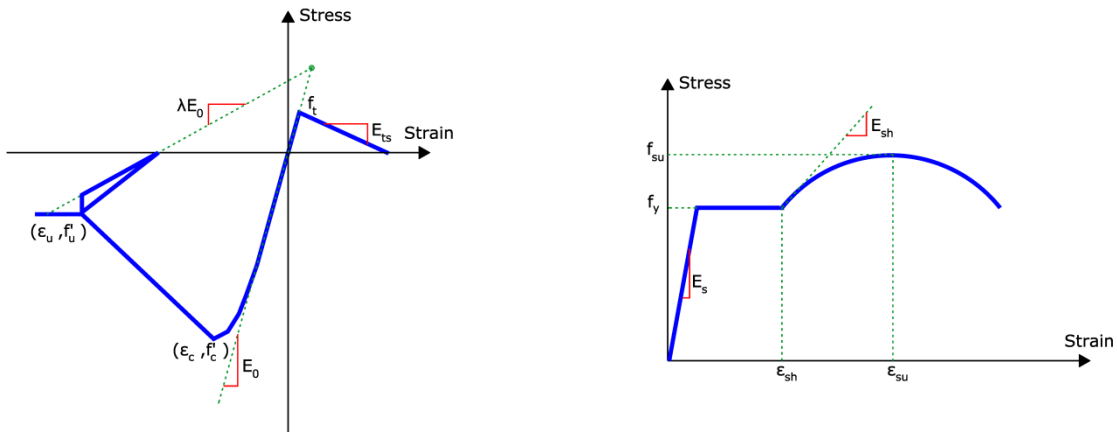

(a) (b)

Figure 5–2 Stress-strain relationship models for (a) concrete02 (b) reinforcing steel

Column elements of the bents are modeled using BeamWithHinges elements with concentrated plasticity at both ends of the columns. P-Delta Coordinate Transformation object is utilized to take the second order P-Δ effects into consideration. A displacement-based pushover analysis is performed by applying incremental displacements to mid-points of the link beams of the bents. The failure of the bents is assumed to occur when the confined concrete at the extreme compression fiber of the core concrete reaches the ultimate concrete compressive strain. Pushover curves of the bents of the bridge specimen are presented in figure 5–3.

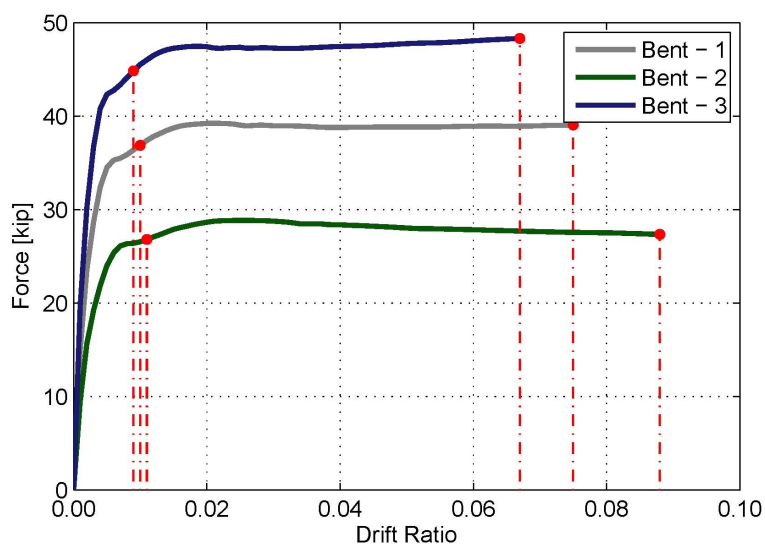

Figure 5–3 Pushover curves of the bents

5.2.2 From Measured Accelerations to Structural Drifts

With careful signal post-processing; double integration of acceleration time histories can yield meaningful displacement data; although slight errors will occur, particularly if shocks are present in the original acceleration time histories [59]. In general, integration of acceleration data introduces baseline drifts and numerical errors due to convolution of noise in measurements. Several methods and procedures have been proposed to minimize the errors due to the baseline drifts [60-64]. In this study, high-order band-pass digital filters are used to eliminate the low-frequency drifts after each integration step. Designing a proper digital filter is a critical aspect of structural deformation analysis. A 100th-order finite impulse response (FIR) filter with passband of $0.5\,Hz \le f \le 30.0\,Hz$ is designed and applied to signals in both forward and reverse directions to produce precisely zero-phase filtering distortion(figure 5–4). In order to validate the double-integration procedure results, estimated analytical column drifts are compared with the drift ratios calculated using measured displacements at the top and bottom of the bents of the bridge in figure 5–5 through figure 5–12.

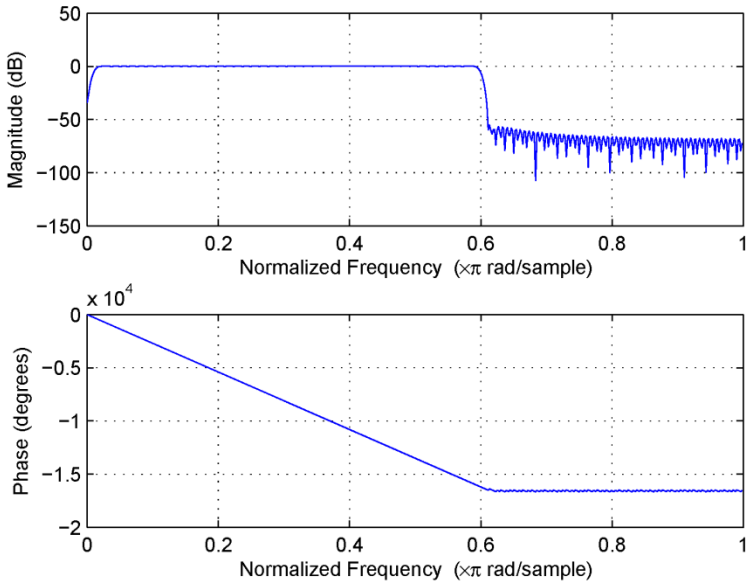

Figure 5–4 Frequency response of designed digital filter

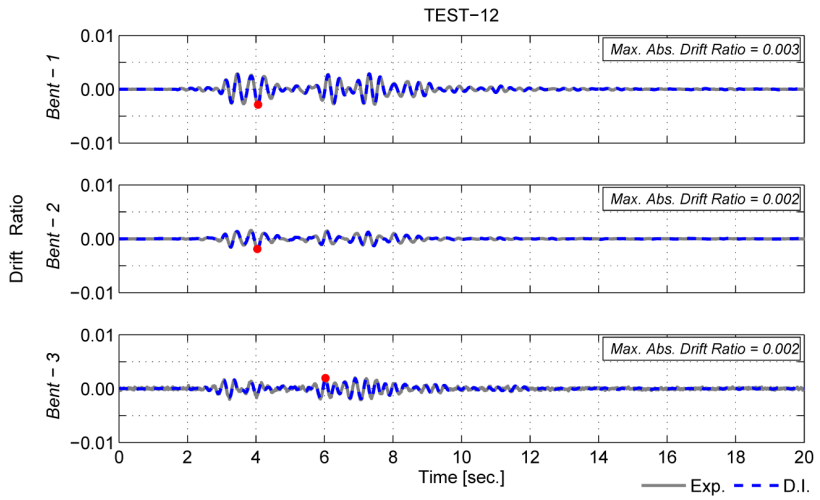

Figure 5–5 Comparison of double integration results with displacement measurements (Test-12)

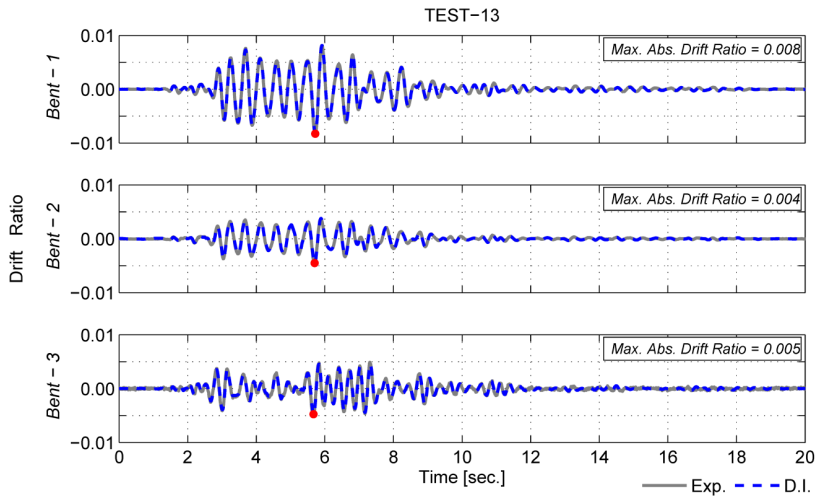

Figure 5–6 Comparison of double integration results with displacement measurements (Test-13)

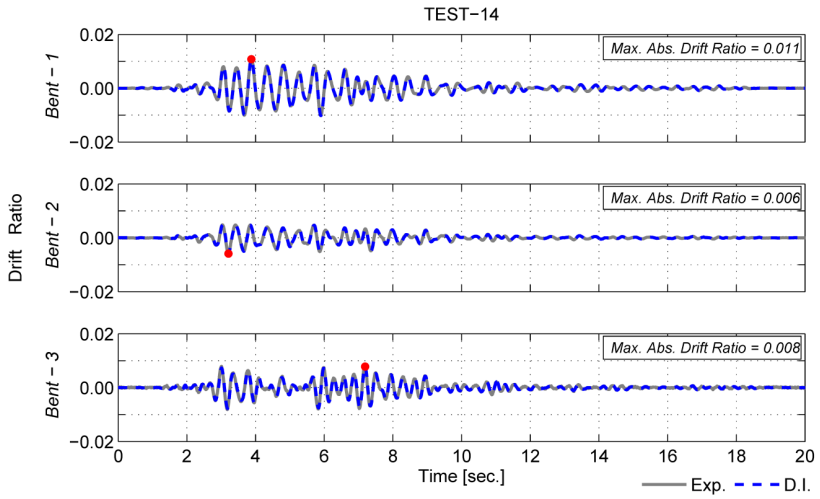

Figure 5–7 Comparison of double integration results with displacement measurements (Test-14)

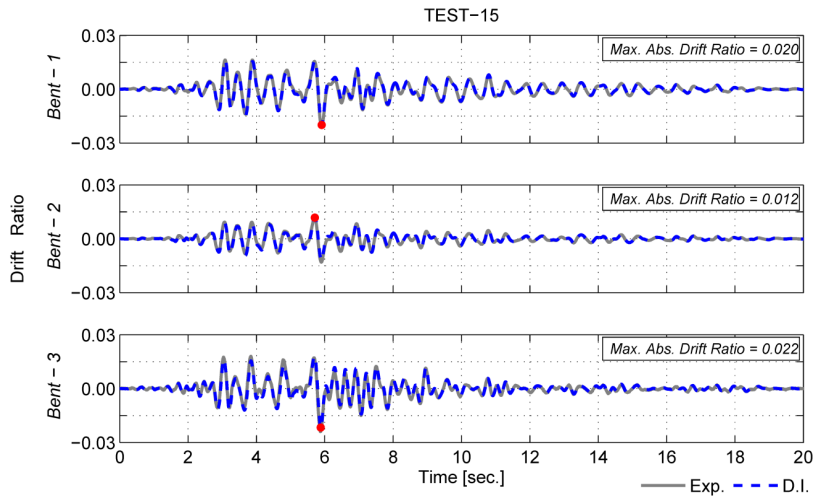

Figure 5–8 Comparison of double integration results with displacement measurements (Test-15)

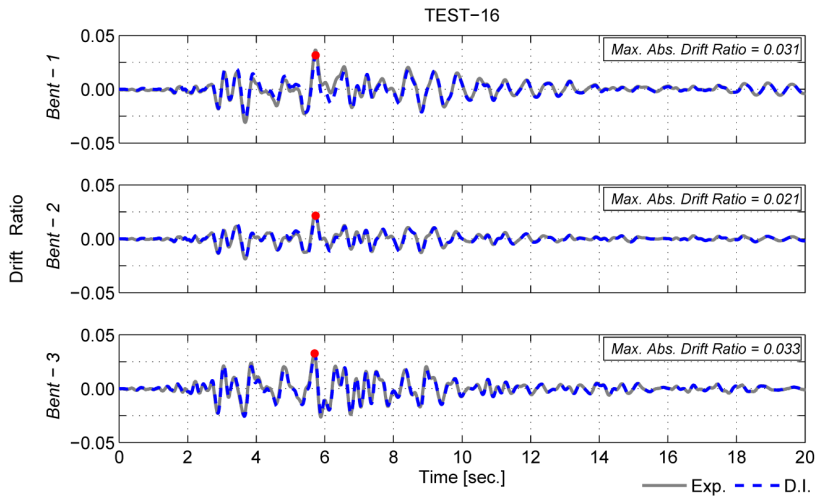

Figure 5–9 Comparison of double integration results with displacement measurements (Test-16)

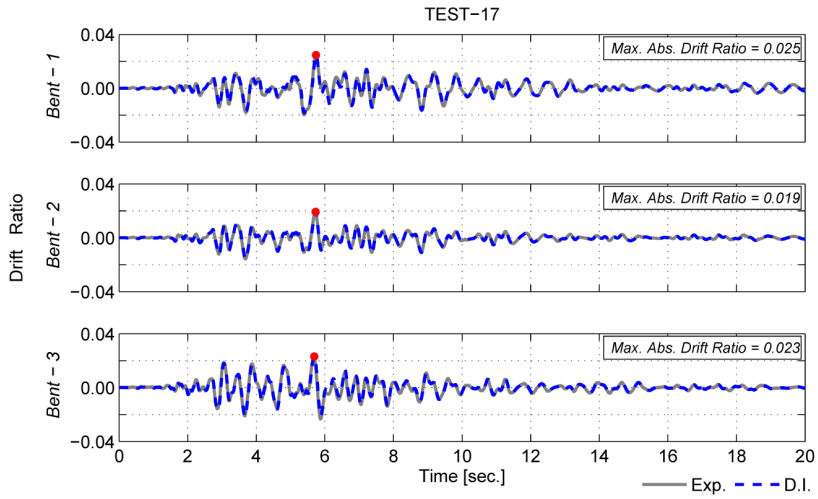

Figure 5–10 Comparison of double integration results with displacement measurements (Test-17)

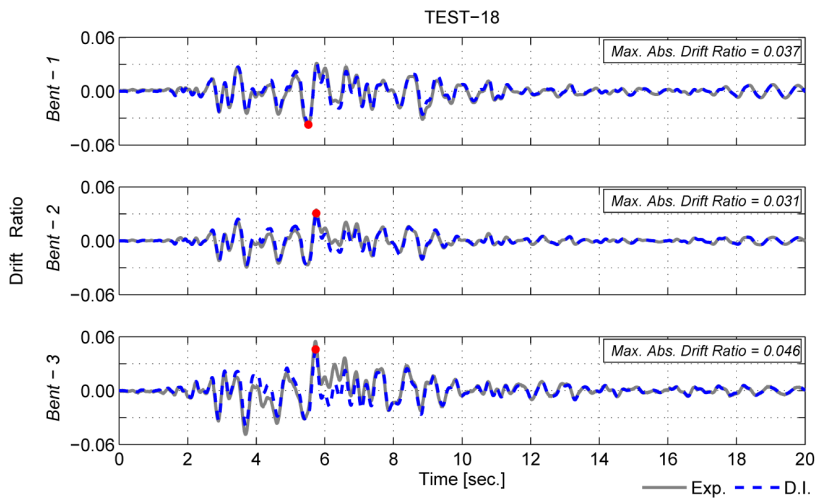

Figure 5–11 Comparison of double integration results with displacement measurements (Test-18)

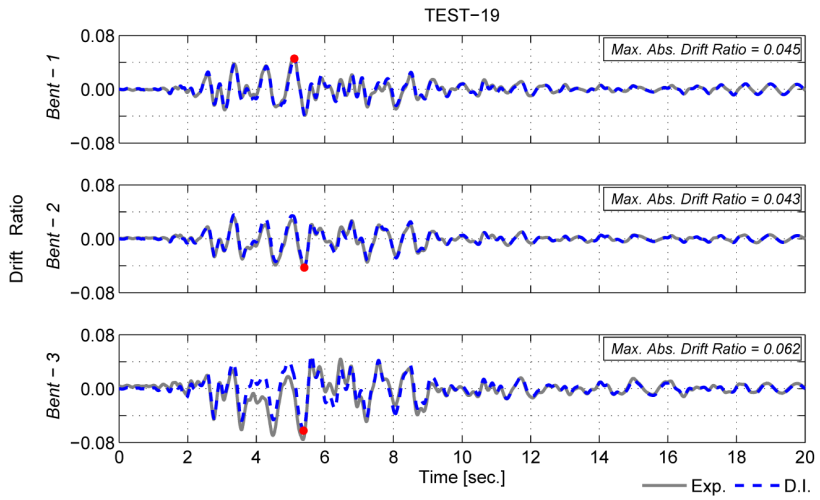

Figure 5–12 Comparison of double integration results with displacement measurements (Test-19)

5.2.3 Ductility-based Residual Capacity of the Specimen

Using the displacement time histories calculated by double-integration of the measured acceleration signals at the top and bottom of each bent of the bridge, maximum drift ratios reached by the bents of the bridge during each earthquake excitation are obtained. These values are used to estimate the ductility ratios of the bents at different stages of the experiment. Maximum drift ratios during each earthquake excitation and pushover curves of the bents are shown in figure 5–13 through figure 5–15. The double-integration procedure results with experimental drift measurements and relative errors between these parameters are listed in table

5-1 through table 5-3. The average relative error value of (5.51%) between analytical and experimental drift rations indicates that the implemented procedure could effectively be used for estimation of the maximum drift ratios from acceleration measurements.

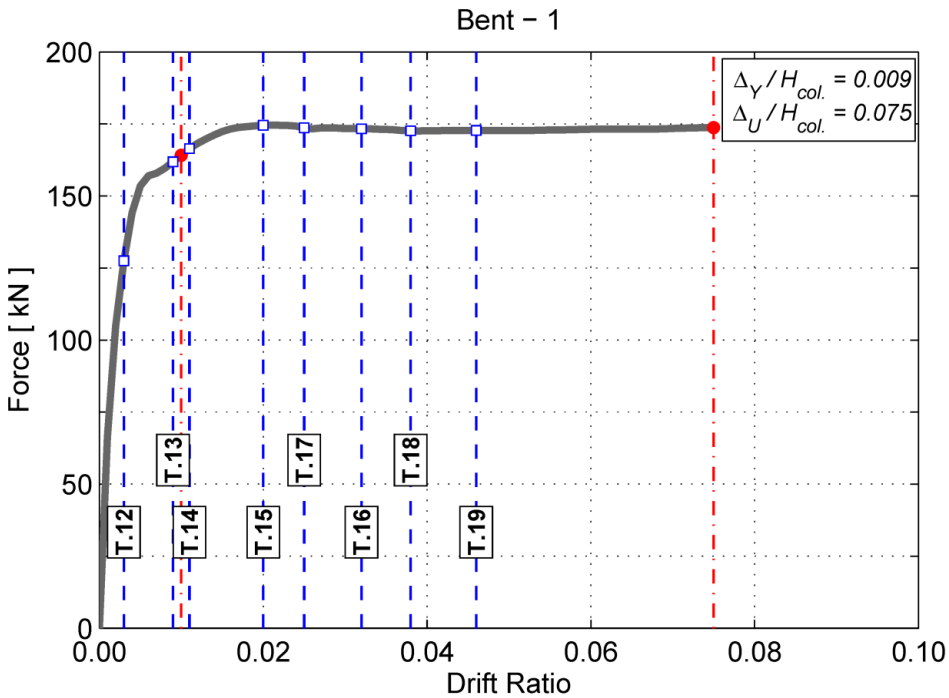

Figure 5–13 Pushover curve and drift ratios estimated using double-integration (Bent-1)

Table 5-1 Maximum Drift Ratios (Bent-1)

	Bent-1 (Δ_Y = 9.30E-3 Δ_U = 7.50E-2)			
	Max. Drift Ratio (Double Integration)	Max. Drift Ratio (Measurement)	Relative Error (%)	Ductility (μ_{DI-1})
Test-12	2.90E-03	3.00E-03	3.33%	0.322
Test -13	8.30E-03	8.50E-03	2.35%	0.922
Test -14	1.08E-02	1.08E-02	0.00%	1.200
Test -15	1.99E-02	2.11E-02	5.69%	2.211
Test -16	3.15E-02	3.64E-02	13.46%	3.500
Test -17	2.46E-02	2.57E-02	4.28%	2.733
Test -18	3.73E-02	3.90E-02	4.36%	4.144
Test -19	4.54E-02	4.88E-02	6.97%	5.044

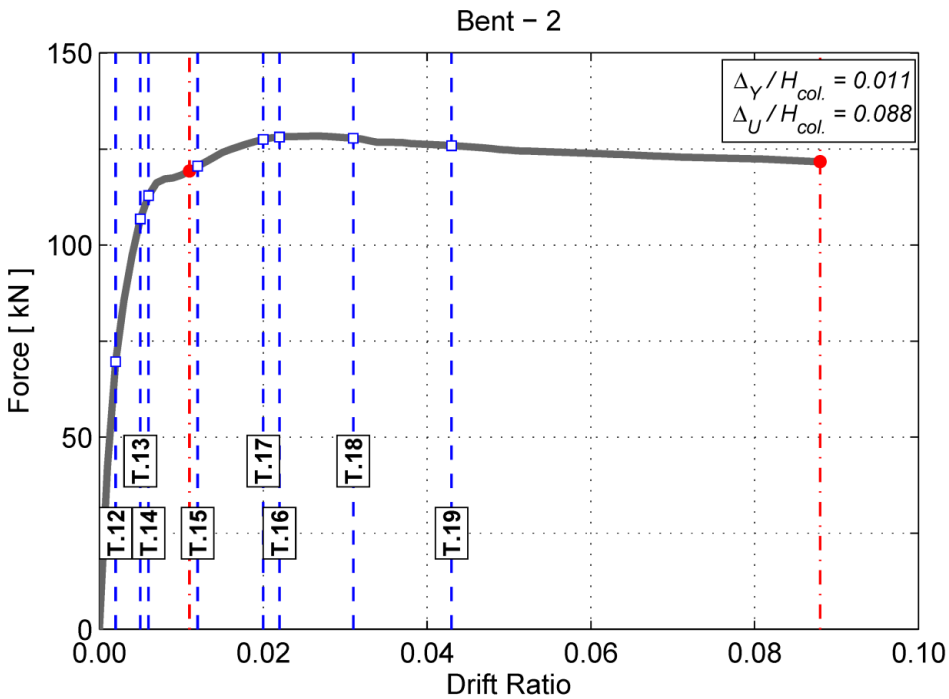

Figure 5–14 Pushover curve and drift ratios estimated using double-integration (Bent-2)

Table 5-2 Maximum Drift Ratios (Bent-2)

	Bent-2 (Δ_Y = 1.08E-2 Δ_U = 8.82E-2)			
	Max. Drift Ratio (Double Integration)	Max. Drift Ratio (Measurement)	Relative Error (%)	Ductility (μ_{DI-2})
Test-12	1.90E-03	1.80E-03	5.56%	0.173
Test -13	4.50E-03	4.50E-03	0.00%	0.409
Test -14	5.90E-03	5.90E-03	0.00%	0.536
Test -15	1.18E-02	1.16E-02	1.72%	1.073
Test -16	2.15E-02	2.34E-02	8.12%	1.955
Test -17	1.93E-02	1.90E-02	1.58%	1.755
Test -18	3.07E-02	3.44E-02	10.76%	2.791
Test -19	4.27E-02	4.36E-02	2.06%	3.882

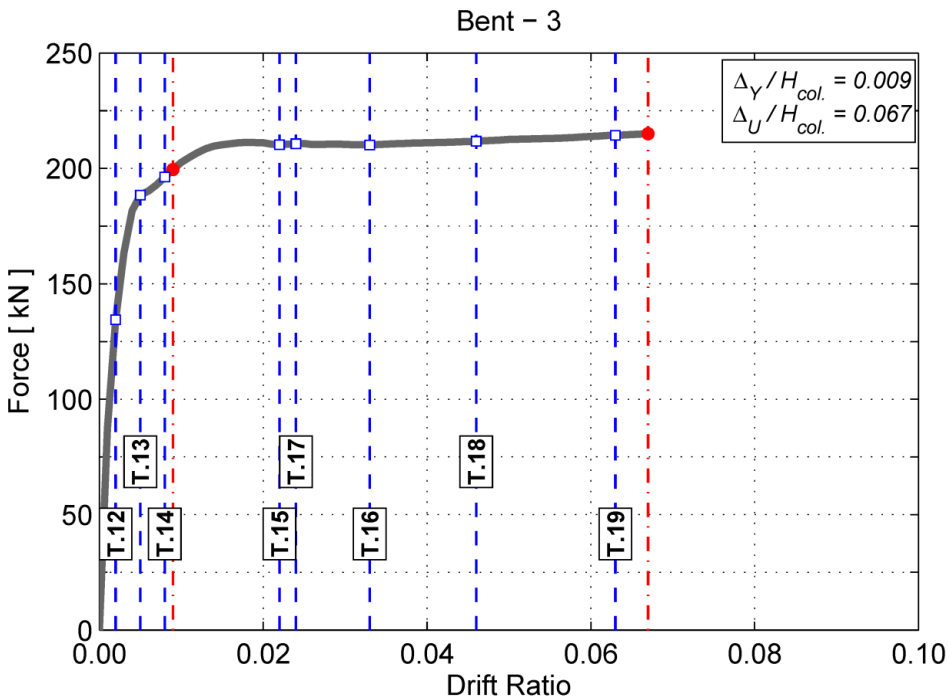

Figure 5–15 Pushover curve and drift ratios estimated using double-integration (Bent-3)

Table 5-3 Maximum Drift Ratios (Bent-3)

	Bent-3 (Δ_Y = 8.51E-3 Δ_U = 6.74E-2)			
	Max. Drift Ratio (Double Integration)	Max. Drift Ratio (Measurement)	Relative Error (%)	Ductility (μ_{DI-3})
Test-12	2.00E-03	1.90E-03	5.26%	0.222
Test -13	4.80E-03	5.10E-03	5.88%	0.533
Test -14	7.80E-03	8.00E-03	2.50%	0.867
Test -15	2.16E-02	2.39E-02	9.62%	2.400
Test -16	3.27E-02	3.15E-02	3.81%	3.633
Test -17	2.31E-02	2.25E-02	2.67%	2.567
Test -18	4.60E-02	5.46E-02	15.75%	5.111
Test -19	6.23E-02	7.46E-02	16.49%	6.922

5.2.4 Summarization of the Results

In order to summarize the results of the first residual capacity estimation method, estimated ductility ratios (μ_{DI}) along with the maximum ductility capacity (μ_c) of bents (calculated during pushover analysis) are used to define the residual capacities (RC) for the bents and for the bridge specimen. The residual capacity of each bent of the bridge is defined as:

$$RC_i = 1 - \left(\frac{\mu_{DI}}{\mu_c} \right) \tag{5-1}$$

Because of the low redundancy level of the bridge specimen the residual capacity of the whole bridge system is defined as the minimum of the residual capacities of the bents. Residual capacity values for the bents and bridge are listed in table 5-4.

Table 5-4 Residual capacity of the bridge

Test	Bent-1 ($\mu_c = 8.333$)		Bent-2 ($\mu_c = 8.000$)		Bent-3 ($\mu_c = 7.441$)		RC_{Bridge} $min(\mu_{DI-1:3})$
	μ_{DI-1}	RC_1	μ_{DI-2}	RC_2	μ_{DI-3}	RC_3	
Test-12	0.322	96.13%	0.173	97.84%	0.222	97.02%	96.13%
Test -13	0.922	88.93%	0.409	94.89%	0.533	92.84%	88.93%
Test -14	1.200	85.59%	0.536	93.30%	0.867	88.35%	85.59%
Test -15	2.211	73.46%	1.073	86.59%	2.400	67.74%	67.74%
Test -16	3.500	57.98%	1.955	75.56%	3.633	51.17%	51.17%
Test -17	2.733	67.19%	1.755	78.06%	2.567	65.50%	51.17%
Test -18	4.144	50.25%	2.791	65.11%	5.111	31.30%	31.30%
Test -19	5.044	39.45%	3.882	51.48%	6.922	6.96%	6.96%

5.2.5 Application to a Toll Bridge Road

The ductility-based residual capacity estimation method has been tested on the San Diego – Coronado bridge, better known just as Coronado bridge. Constructed in 1969, the 11,179 feet-long-bridge is composed by 29 spans and is characterized by a 90° curve in plan. The superstructure is formed by steel plate girders, except for the 3 spans over the navigation

channels, which are orthotropic box girders. The substructure is composed by 2-column concrete bents of different heights, with the tallest one reaching 200 feet on the navigation channel.

The bridge had been originally instrumented in 1994 with 9 accelerometers within the California Strong Motion Instrumentation Program (CSMIP), then it was more extensively instrumented in 2002 during the retrofit work, reaching a total of 72 acceleration sensors. Figure 5–16 shows the elevation and the plan view of the bridge, together with the sensors location.

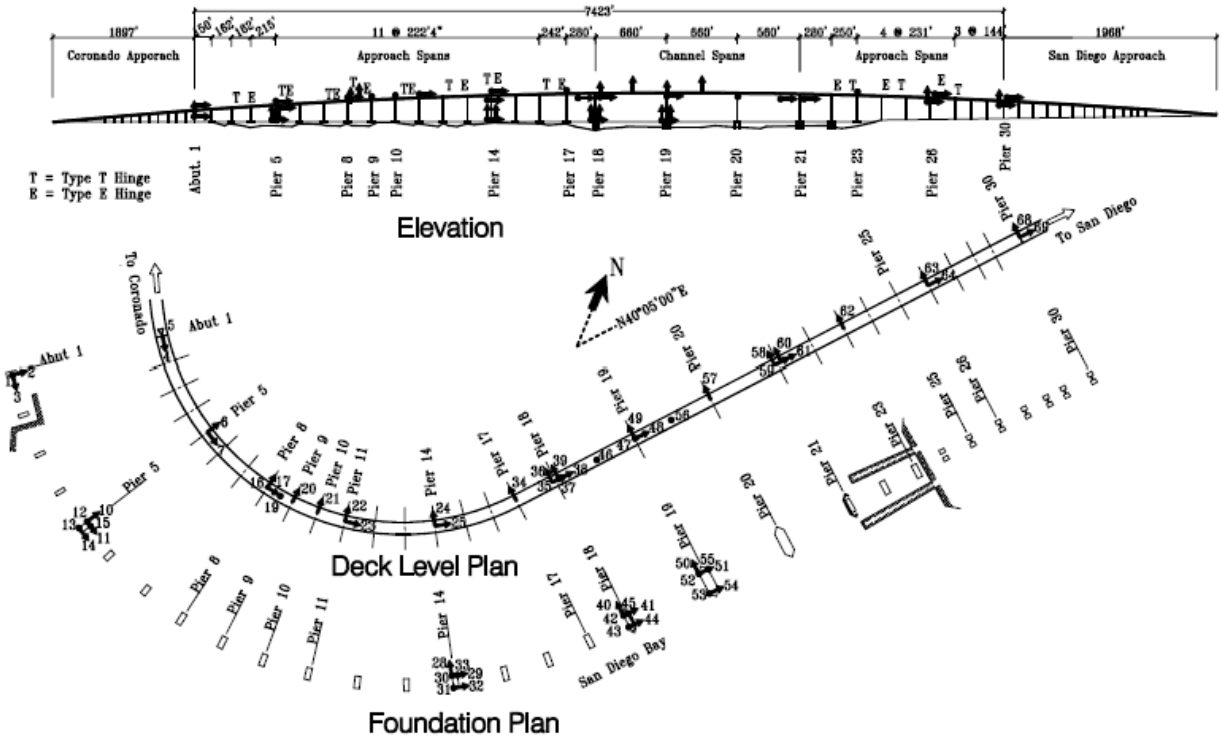

Figure 5–16 Elevation and plan view of Coronado bridge and sensors layout

Up to now, the sensor network has recorded just one earthquake, the 2004 San Clemente earthquake, and such acceleration data will be used to investigate the post-event residual capacity of the structure within the frame of the ductility-based residual capacity estimation technique. Although 72 channels are installed on the bridge, only 12 of them actually recorded the structural vibration during the 2004 San Clemente earthquake; moreover, only at bent 19 the sensors on both the top and the bottom of the pier in both the longitudinal and transverse direction were

recording the seismic response of the structure. For these reasons the residual capacity estimation method will be applied to pier 19. Figure 5–17 shows pier 19 and the location of the sensors on the bent. The sensors installed on pier 19 that actually collected acceleration data during the 2004 San Clemente earthquake, and so will be used in the analysis, are:

- sensor 48: at the top of the bent, in longitudinal direction;
- sensor 49: at the top of the bent, in transverse direction;
- sensor 50: on the pile cap, in transverse direction;
- sensor 51: on the pile cap, in longitudinal direction.

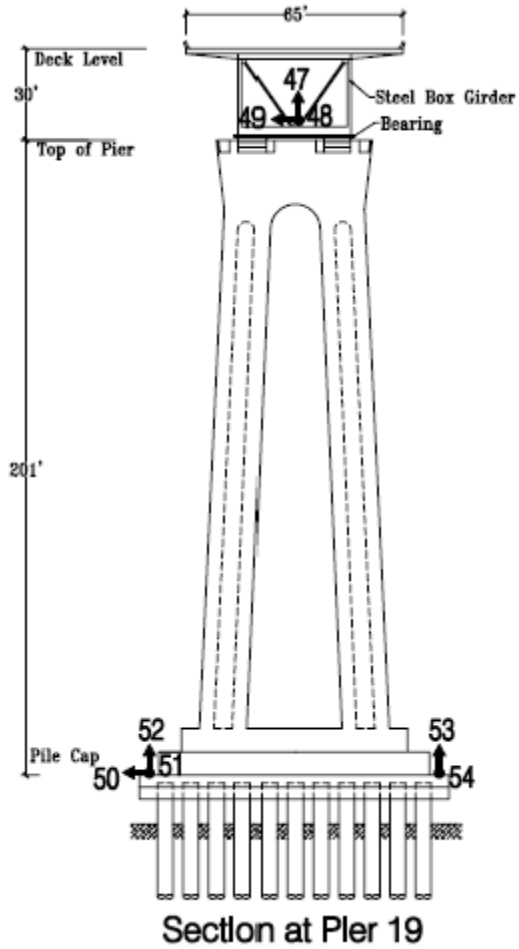

Figure 5–17 Elevation and plan view of Coronado bridge and sensors layout

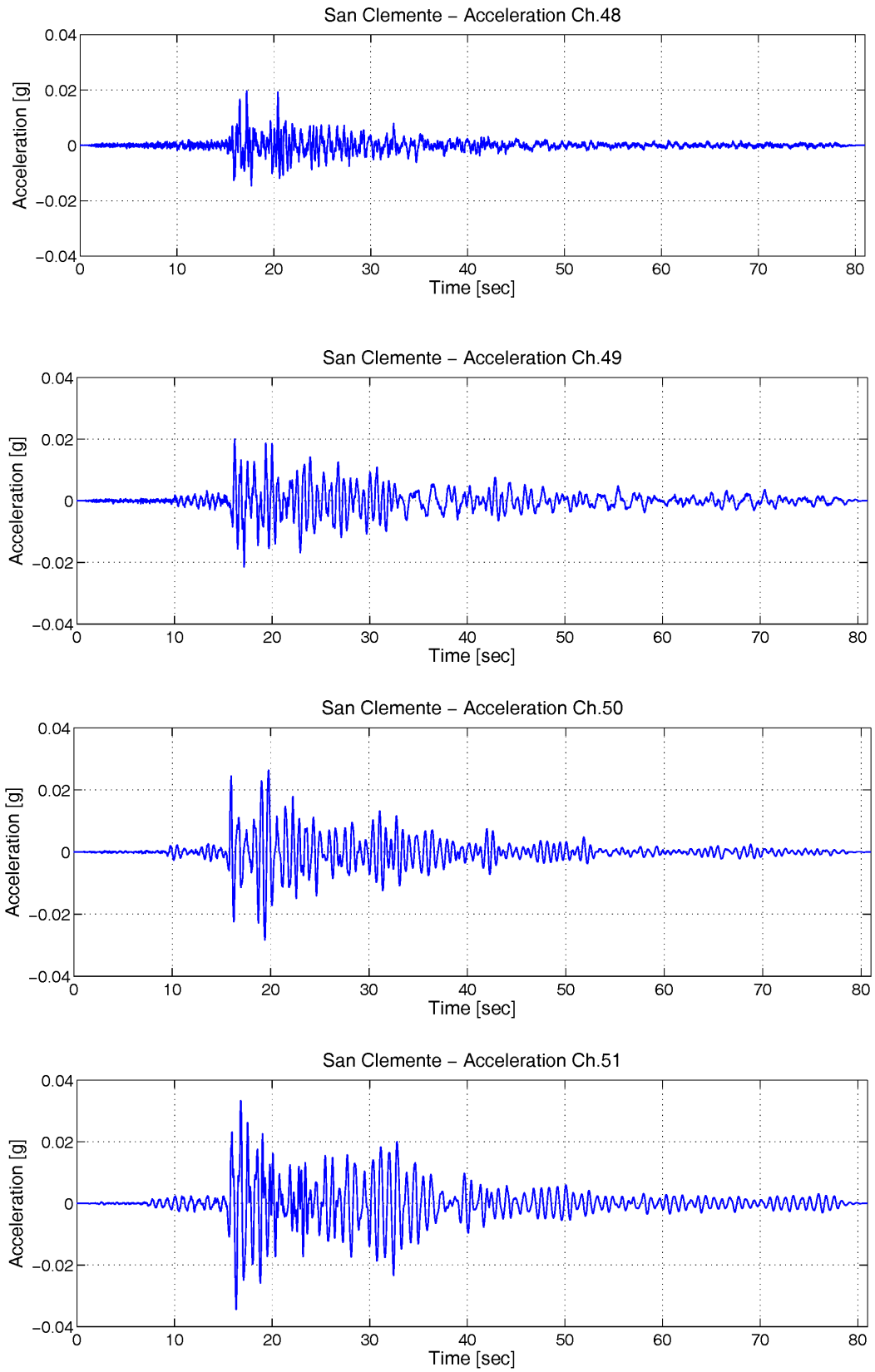

Figure 5–18 Response histories measured by channels 48, 49, 50, and 51 at pier 19

Figure 5–18 provides the acceleration time histories measured by the 4 sensors mentioned above. Double integration of the acceleration histories will yield the maximum drift ratio experienced by the pier in both transverse and longitudinal directions; then the pushover curves (in transverse and longitudinal direction) of the pier will be entered with the respective drift values and the residual capacity of the bent will be assessed. The procedure adopted and the results obtained will be detailed in the following.

In order to avoid numerical errors in the double integration procedure due to convolution of noise in the measurements, an accurate signal post-processing has been adopted. A 160th-order finite impulse response (FIR) filter with passband of $0.5\,Hz \le f \le 30.0\,Hz$ was designed and applied to signals in both forward and reverse directions to produce precisely zero-phase filtering distortion. The accuracy of the results obtained by the double integration procedure has been proved by the analysis conducted on the bridge specimen described in the previous paragraphs. Figure 5–19 provides the results of the double integration process in terms of relative drift ratio histories in transverse (difference between the drift ratios of channels 49 and 50) and longitudinal (difference between the drift ratios of channels 48 and 51) directions. From the figure it is possible to read the maximum absolute relative drift ratio in the transverse direction, which is 0.0001045, and in the longitudinal direction, which is 0.0001383.

The two pushover curves of the structure were generated by using the Opensees FE software. A nonlinear FE model of the pier was constructed by using the nonlinear beam column elements in Opensees; the elemental section properties were modeled using fiber sections with concrete01 and reinforcing steel material models (figure 5–20). The geometry and the material properties of the FE model were carefully reproduced on the base of the structural drawings of the bridge in

order to accurately capture the nonlinear behavior of the structure. Figure 5–21 provides a schematic view of the FE model built.

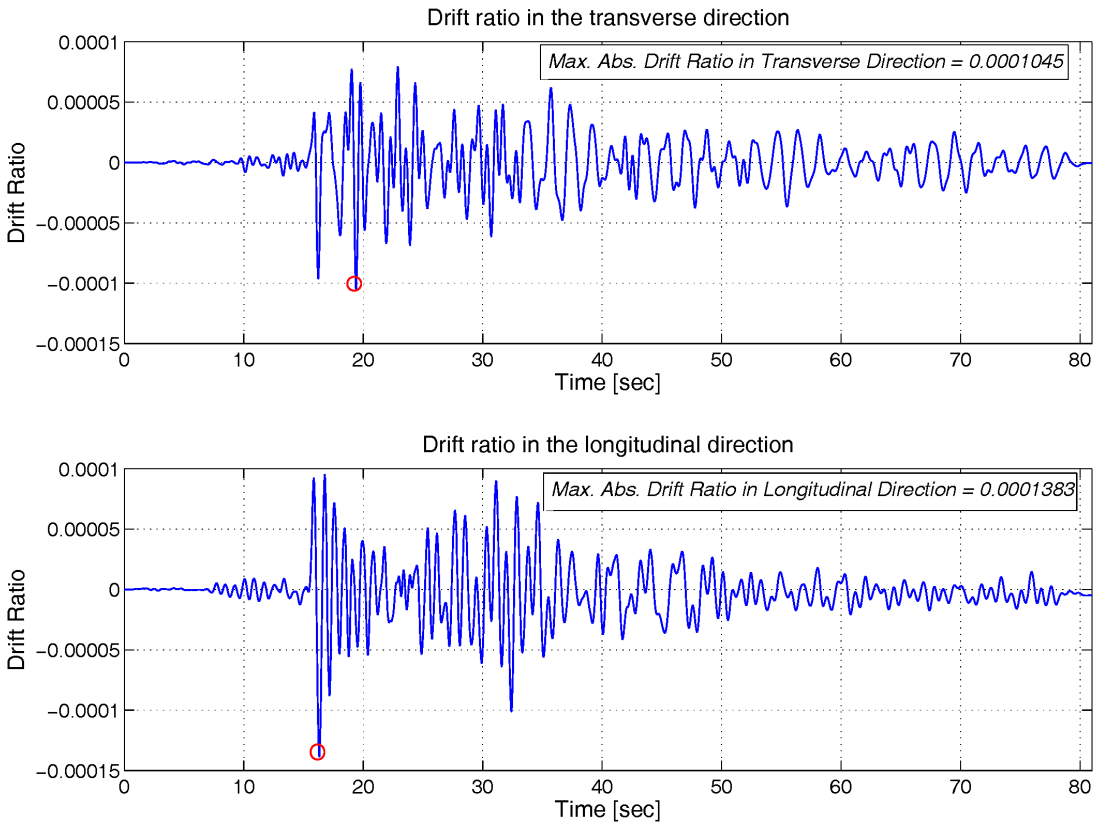

Figure 5–19 Relative drift ratios from double integration procedure

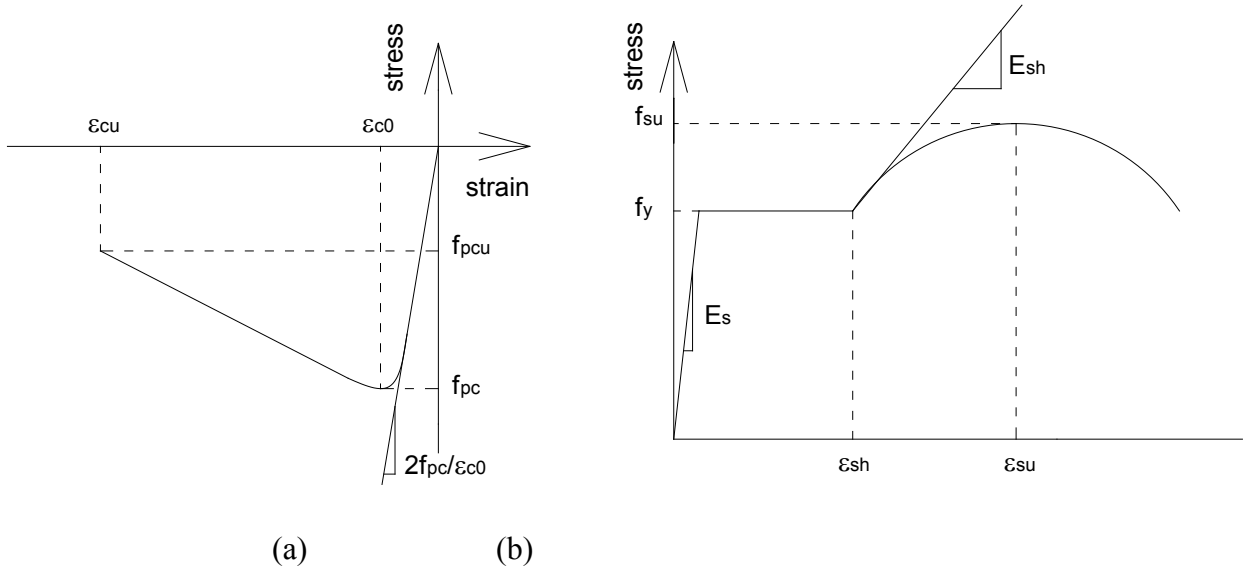

Figure 5–20 Stress-strain relationship models for (a) concrete01 (b) reinforcing steel

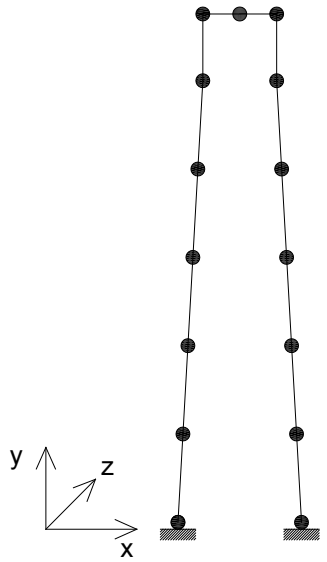

Figure 5–21 FE model of pier 19

A displacement-based pushover analysis was performed in both transverse and longitudinal direction (*x* and *z* directions with reference to figure 5–21, respectively) by applying incremental displacements to the mid-point of the link beam of the two columns composing the bent. The failure of the bent is assumed to occur when the confined concrete at the extreme compression fiber of the core concrete reaches the ultimate concrete compressive strain. The two pushover curves obtained, in transverse and longitudinal direction, are presented in figure 5–22. In order to assess the residual capacity of the bent, the curves have to be entered with the maximum absolute drift ratio experienced by the pier during the 2004 San Clemente earthquake (Figure 5–19). Such values, calculated by double integration of the acceleration measurements, are indicated in figure 5–22 with a red dot. From the plots, it emerges that the maximum absolute drift ratio due to the seismic event in both of the two directions is so small that it does not cause any excursion of the structure in the nonlinear range of the materials. Consequently, the 2004 San Clemente earthquake induced no loss of capacity of the structure, whose post-event residual capacity will be equal to 100%.

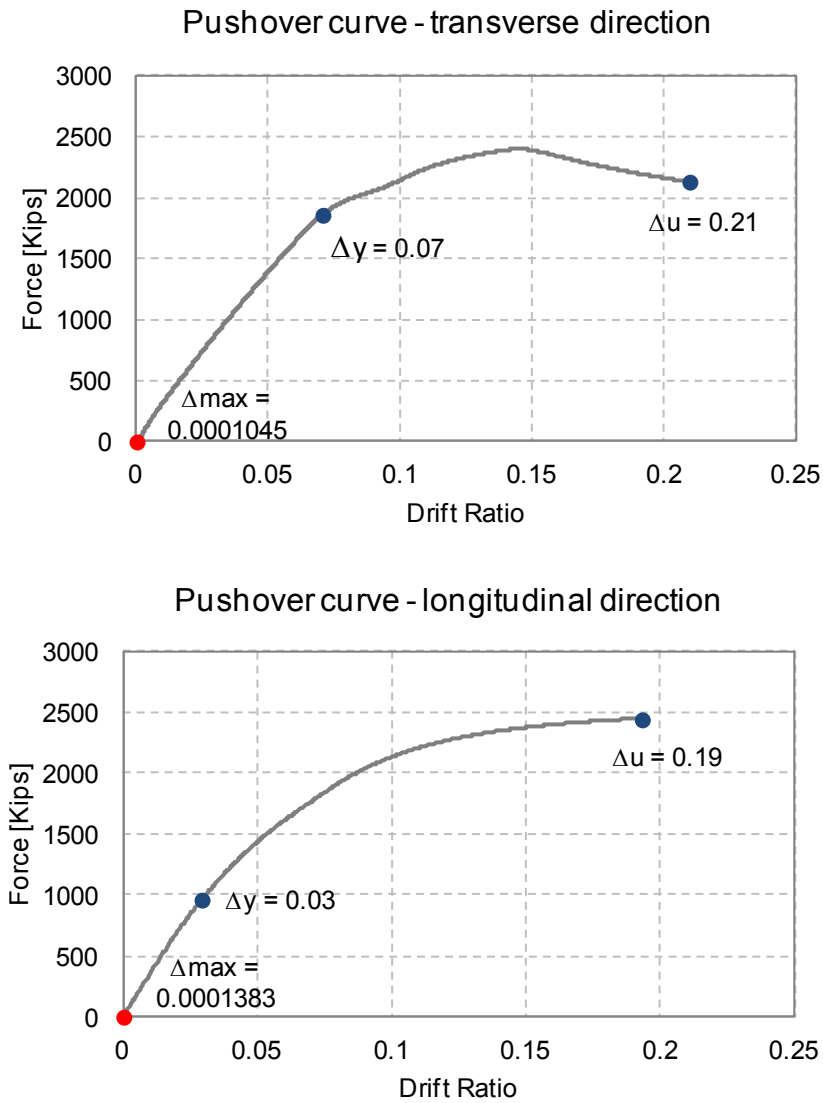

Figure 5–22 Pushover curves in transverse and longitudinal directions, and drift ratios estimated by double integration

5.3 Residual Capacity Estimation Using Incremental Dynamic Analysis

In this section of the study, incremental dynamic analysis (IDA) curves are utilized for estimation of the residual collapse capacity of the intact and damaged structures. A five step procedure is proposed to incorporate experimental modal identification data for residual collapse

capacity estimation and functionality status update of the bridge specimen at different phases of the experiment. Figure 5–23 presents the flowchart of the proposed procedure.

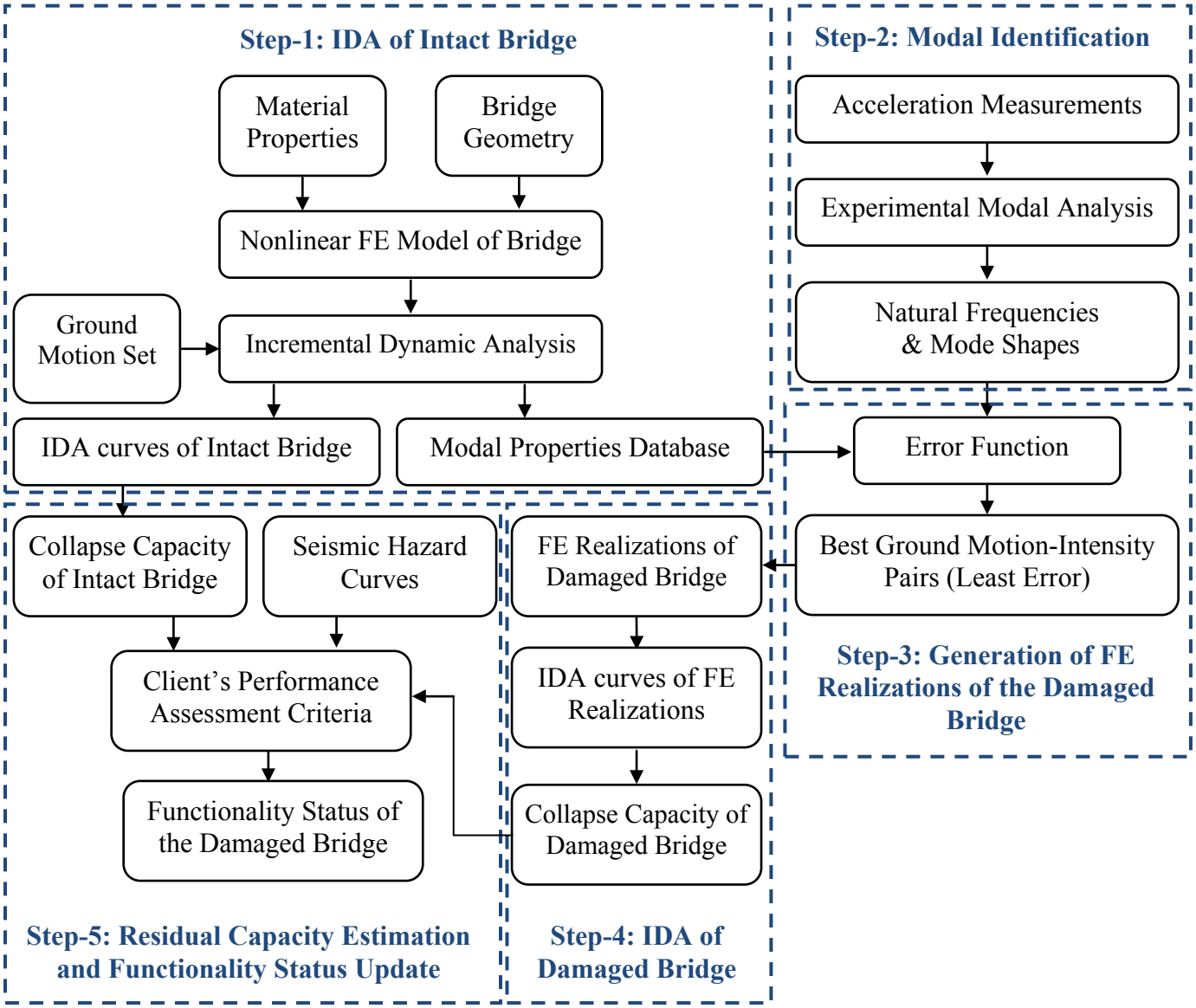

Figure 5–23 Flowchart of IDA-based residual capacity estimation method

An IDA involves performing a series of nonlinear response history analyses in which the intensity of input ground motions are incrementally increased until the global collapse capacity of the structure is reached. It also involves plotting a measure of the ground motion intensity (e.g. spectral acceleration at the fundamental natural frequency of the structure) against a

response parameter (demand measure) such as peak drift ratio. In order to incorporate the large variation in intensity and frequency content of the ground motions, statistical properties of IDA curves corresponding to a large number of ground motions are generally used for more accurate prediction of seismic demand at the structure site. For this study, 40 ground motions (denoted as LMSR-N ground motion set) that represent the characteristics of ordinary California earthquakes are utilized (table 5-5). Only California earthquakes of moment magnitude (M_w) between (6.5) and (6.9) with the closest distance to the fault rupture between (13 km) and (40 km) are considered. All ground motions were recorded on NEHRP site Class D[65]. Spectral accelerations of the ground motions in LMSR-N set and corresponding sectional median and 16 and 84 percentiles are presented in figure 5–24(a).

The collapse capacity of the structure is defined in terms of median ground motion intensity level necessary to induce either global lateral instability or local collapse anywhere within the structure. A double-clause composite rule based on the slope of the IDA curves and the maximum demand measure is used for identification of the collapse capacity point on each IDA curve. The slope-based criterion identifies the last point on the IDA curve with tangent slope equal or less than 20% of the elastic slope as the collapse capacity point. The second rule restricts the maximum drift ratio within the bents of bridge to 10%[66].In the following subsections, details of the five-step vibration-based residual collapse capacity estimation procedure are discussed as they are applied to shake table experiment results.

Table 5-5 LMSR-N ground motion set

GM #	Event	Year	Mw	Station	Distance (Km)	Site	Mechanism	PGA (g)	PGV (cm/s)	PGD (cm)
1	Imperial Valley	1979	6.5	Calipatria Fire Station	23.8	D	strike-slip	0.078	13.3	6.2
2	Imperial Valley	1979	6.5	Chihuahua	28.7	D	strike-slip	0.27	24.9	9.1
3	Imperial Valley	1979	6.5	Compuertas	32.6	D	strike-slip	0.186	13.9	2.9
4	Imperial Valley	1979	6.5	El Centro Array #1	15.5	D	strike-slip	0.139	16	10
5	Imperial Valley	1979	6.5	El Centro Array #12	18.2	D	strike-slip	0.116	21.8	12.1
6	Imperial Valley	1979	6.5	El Centro Array #13	21.9	D	strike-slip	0.139	13	5.8
7	Imperial Valley	1979	6.5	Niland Fire Station	35.9	D	strike-slip	0.109	11.9	6.9
8	Imperial Valley	1979	6.5	Plaster City	31.7	D	strike-slip	0.057	5.4	1.9
9	Imperial Valley	1979	6.5	Cucapah	23.6	D	strike-slip	0.309	36.3	10.4
10	Imperial Valley	1979	6.5	Westmorland Fire	15.1	D	strike-slip	0.11	21.9	10
11	Loma Prieta	1989	6.9	Agnews State Hospital	28.2	D	reverse-oblique	0.172	26	12.6
12	Loma Prieta	1989	6.9	Capitola	14.5	D	reverse-oblique	0.443	29.3	5.5
13	Loma Prieta	1989	6.9	Gilroy Array #3	14.4	D	reverse-oblique	0.367	44.7	19.3
14	Loma Prieta	1989	6.9	Gilroy Array #4	16.1	D	reverse-oblique	0.212	37.9	10.1
15	Loma Prieta	1989	6.9	Gilroy Array #7	24.2	D	reverse-oblique	0.226	16.4	2.5
16	Loma Prieta	1989	6.9	Hollister City Hall	28.2	D	reverse-oblique	0.247	38.5	17.8
17	Loma Prieta	1989	6.9	Hollister Differential	25.8	D	reverse-oblique	0.279	35.6	13.1
18	Loma Prieta	1989	6.9	Halls Valley	31.6	D	reverse-oblique	0.134	15.4	3.3
19	Loma Prieta	1989	6.9	Salinas-John & Work	32.6	D	reverse-oblique	0.112	15.7	7.9
20	Loma Prieta	1989	6.9	Palo Alto-SLAC Lab.	36.3	D	reverse-oblique	0.194	37.5	10
21	Loma Prieta	1989	6.9	Sunnyvale-Colton Ave.	28.8	D	reverse-oblique	0.207	37.3	19.1
22	Northridge	1994	6.7	LA-Centinela St.	30.9	D	reverse-slip	0.322	22.9	5.5
23	Northridge	1994	6.7	Canoga Park - Topanga	15.8	D	reverse-slip	0.42	60.8	20.2
24	Northridge	1994	6.7	LA-N Faring Rd.	23.9	D	reverse-slip	0.273	15.8	3.3
25	Northridge	1994	6.7	LA-Fletcher Dr.	29.5	D	reverse-slip	0.24	26.2	3.6
26	Northridge	1994	6.7	Glendale-Las Palmas	25.4	D	reverse-slip	0.206	7.4	1.8
27	Northridge	1994	6.7	LA-Holywood Stor FF	25.5	D	reverse-slip	0.231	18.3	4.8
28	Northridge	1994	6.7	Lake Hughes #1 #	36.3	D	reverse-slip	0.087	9.4	3.7
29	Northridge	1994	6.7	Leona Valley #2 #	37.7	D	reverse-slip	0.063	7.2	1.6
30	Northridge	1994	6.7	Leona Valley #6	38.5	D	reverse-slip	0.178	14.4	2.1
31	Northridge	1994	6.7	La Crescenta-New York	22.3	D	reverse-slip	0.159	11.3	3
32	Northridge	1994	6.7	LA - Pico & Sentous	32.7	D	reverse-slip	0.186	14.3	2.4
33	Northridge	1994	6.7	Northridge - 17645	13.3	D	reverse-slip	0.368	28.9	8.4
34	Northridge	1994	6.7	LA - Saturn St	30	D	reverse-slip	0.474	34.6	6.6
35	Northridge	1994	6.7	LA - E Vernon Ave	39.3	D	reverse-slip	0.153	10.1	1.8
36	San Fernando	1971	6.6	LA - Hollywood Stor	21.2	D	reverse-slip	0.174	14.9	6.3
37	Superstition Hills	1987	6.7	Brawley	18.2	D	strike-slip	0.156	13.9	5.4
38	Superstition Hills	1987	6.7	El Centro Imp. Co.	13.9	D	strike-slip	0.358	46.4	17.5
39	Superstition Hills	1987	6.7	Plaster City	21	D	strike-slip	0.186	20.6	5.4
40	Superstition Hills	1987	6.7	Westmorland Fire	13.3	D	strike-slip	0.172	23.5	13

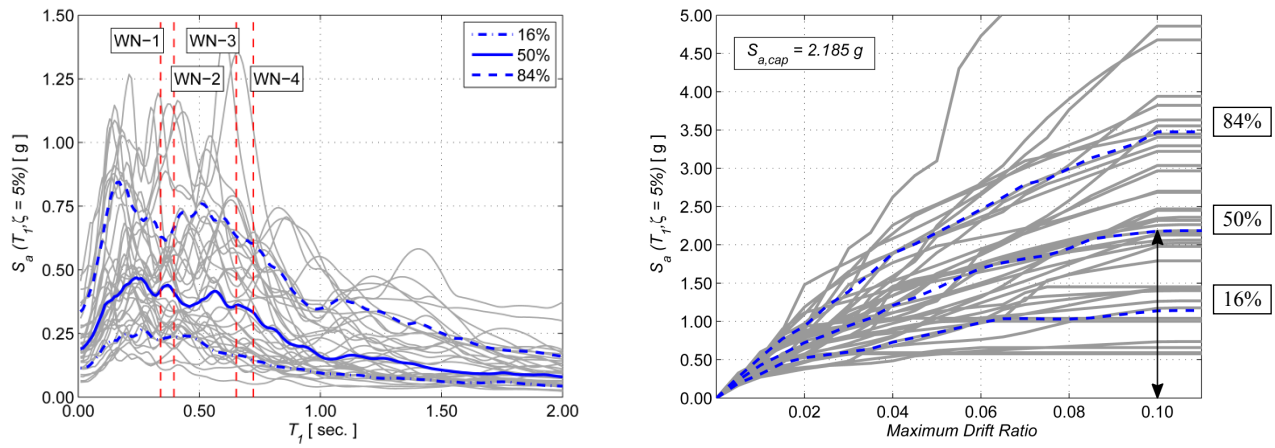

(a) (b)

Figure 5–24 (a) Spectral acceleration of LMSR-N ground motion set (b) IDA curves for the intact bridge.

5.3.1 Step-1: Incremental Dynamic Analysis of the Intact Structure

As the first step for the estimation of the residual collapse capacity of the bridge specimen, a nonlinear FE model of the bridge that incorporates P-delta effects and strength degradation of the structural elements is generated using Open System for Earthquake Engineering Simulation (OpenSees) software framework. The IDA curves corresponding to the 40 ground motions in LMSR-N ground motions set are generated by relatively large number of nonlinear response history analyses. Figure 5–24(b), shows the IDA curves and corresponding cross-sectional median and 16 and 84 percentiles for the intact bridge. Since damage within the structural elements affects the modal properties of the structure, these properties are frequently used to detect, locate and quantify damage within the structures [35, 67]. In order to characterize the damage caused by each ground motion-intensity pair, modal properties of the bridge including natural frequencies and mode shapes of significant modes of vibration of the bridge are calculated after each nonlinear response history analysis. These properties along with the input ground motion characteristics are stored in a database to be used on the third step of the

procedure. Figure 5–25 shows the variation of post-earthquake natural frequencies of the first three transverse modes of the bridge with the intensity level of the earthquake ground motion. The median frequency curves (dashed lines) can readily be used by bridge owners after a damaging earthquake for a primary assessment about damage status of the bridge.

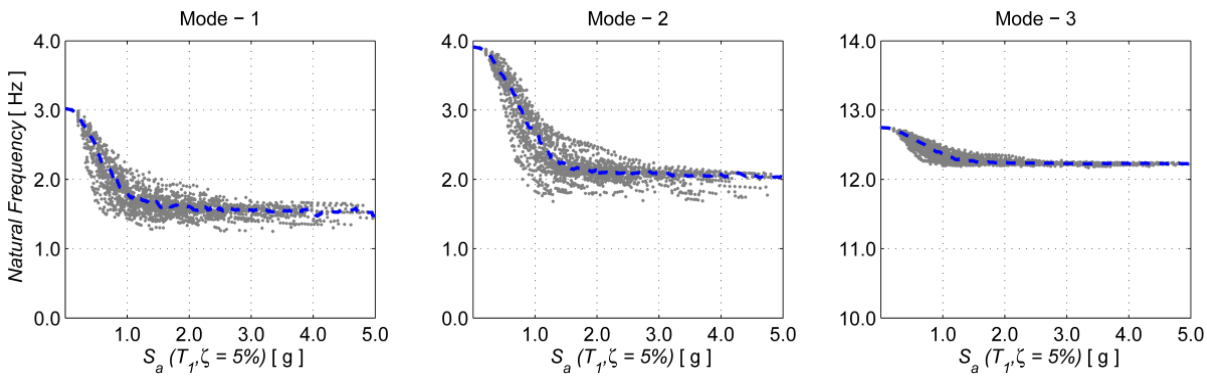

Figure 5–25 Post-earthquake modal frequencies of the bridge

5.3.2 Step-2: Experimental Modal Analysis of Damaged Structure

Natural frequencies and mode shapes are the most common features used in vibration-based damage assessment and characterization of the structures. These features are identified from response histories measured during either ambient or forced vibrations of the structure. The modal properties identified from white noise excitations using prediction-error state space system identification technique are utilized. Identified natural frequencies, modal damping ratios and the mode shapes of the bridge identified from white noise excitations are listed in table 5-6. As it was shown earlier, the first and second transverse modes of vibration of the bridge consist of translation and torsion of the deck of the bridge, respectively, which are mainly controlled by the lateral stiffness of the bents. The third mode of vibration of the bridge imposes significant in-plan bending to the deck of the bridge which makes it more sensitive to the in-plane bending stiffness properties of the deck in comparison to the lateral stiffness of the bents. As a result, small reduction in the third mode frequency over the whole experiment (less than 7% in

comparison to 55% and 60% for the first two modes frequencies) can be described as a result of minimal damage to the superstructure of the bridge which is consistent with the visual inspections results that indicated no damage within the superstructure of the bridge.

Table 5-6 Experimental modal analysis results

Test	Mode #	f (Hz)	ζ(%)	ϕ_{1i}	ϕ_{2i}	ϕ_{3i}	ϕ_{4i}	ϕ_{5i}
W.N. 1	1	2.937	3.5%	0.664	0.549	0.412	0.278	0.107
	2	3.860	3.9%	-0.404	-0.066	0.219	0.494	0.735
	3	12.683	1.9%	-0.416	0.418	0.612	0.367	-0.378
W.N. 2	1	2.528	5.5%	0.694	0.548	0.394	0.243	0.064
	2	3.443	5.1%	-0.440	-0.097	0.200	0.475	0.729
	3	12.274	1.9%	-0.402	0.421	0.616	0.371	-0.380
W.N. 3	1	1.532	5.1%	0.687	0.542	0.399	0.259	0.092
	2	1.817	5.7%	-0.287	0.012	0.247	0.511	0.772
	3	11.982	2.5%	-0.397	0.437	0.601	0.381	-0.381
W.N. 4	1	1.383	5.3%	0.544	0.498	0.437	0.395	0.332
	2	1.569	7.3%	-0.497	-0.171	0.114	0.419	0.732
	3	11.960	1.7%	-0.425	0.425	0.603	0.380	-0.360

5.3.3 Step-3: Generation of FE Realizations of Damaged Bridge

In this step, the modal properties database created during the IDA of the intact bridge is utilized to identify the ground motion-intensity pairs that can drive nonlinear FE model of the bridge into the current damage state of the bridge and produce FE realizations of the damaged structure. In an ideal case, we are interested in ground motion-intensity pairs that after their application to the FE model of the bridge, analytical post-earthquake modal properties of the bridge exactly match the experimental values identified from vibration measurements of the damaged bridge. In order to quantitatively compare the matches between the analytical and experimental post-earthquake modal properties, an error function, E, defined in terms of discrepancy between the analytical

and experimental post-earthquake modal properties is utilized to rank all the ground-motion intensity pairs available in the database:

$$E\left(GM, \hat{S}_a\right) = \sum_{i=1}^{n_d} \left(W_{fi}\Delta f_i + W_{\varphi i}\left(1 - MAC_i\right)\right) \tag{5-2}$$

Here n_d is the number of dominant modes of vibration of the bridge (estimated during experimental modal analysis procedure); W_{fi} and $W_{\phi i}$ are the weights assigned to error in natural frequency and mode shape of the ith mode of vibration of the structure. These weights are assigned based on importance of each mode of vibration in total response of the bridge and reliability of measurement of each modal parameter. Relative error in frequency, Δf_i, and modal assurance criterion, MAC_i, are defined as follows:

$$\Delta f_i = \left|\frac{f_i^e - f_i^a}{f_i^e}\right| \tag{5-3}$$

$$MAC_i = \frac{\left((\varphi_i^e)^T.(\varphi_i^a)\right)^2}{\left((\varphi_i^e)^T.(\varphi_i^e)\right).\left((\varphi_i^a)^T.(\varphi_i^a)\right)} \tag{5-4}$$

Here f_i and ϕ_i represent the natural frequency and mode shape corresponding to the ith mode of vibration of the structure; superscripts e and a denote experimental and analytical modal properties respectively. For the case of the bridge specimen under investigation, the relative importance of each mode is quantified based on the average ratio between the H_2 norm of the isolated transfer function corresponding to that mode and the sum of H_2 norms of the transfer functions of all significant modes of vibration of the bridge. As a result, the relative weights of the error in the first three natural transverse modes of vibration of the bridge are adjusted at (0.55), (0.35) and (0.10) values respectively. The higher reliability in the measurement of the natural frequencies relative to mode shapes is incorporated by assigning higher relative weights

to the errors in natural frequencies (0.67) in comparison to the mode shapes (0.33). The final values of the weighting factors are presented in table 5-7.

Table 5-7 Weighting factors

	Mode - 1		Mode - 2		Mode - 3	
Parameter	W_{f1}	$W_{\varphi 1}$	W_{f2}	$W_{\varphi 2}$	W_{f3}	$W_{\varphi 3}$
Value	0.368	0.182	0.234	0.116	0.067	0.033

In figure 5–26, the errors between analytical and experimental modal properties are plotted against the spectral accelerations of the input ground motions at the first period of the intact bridge. The minimum errors between post-earthquake analytical and experimental modal properties obtained using each ground motion history and the corresponding intensity levels are listed in table 5-8. In the ideal case, FE realizations produced by all of the best ground motion-intensity pairs shall be used for residual capacity estimation; but in this study and due to computational considerations only 5 ground motion-intensity pairs with least error values are selected for generation of FE realizations. The selected pairs are highlighted in table 5-8.

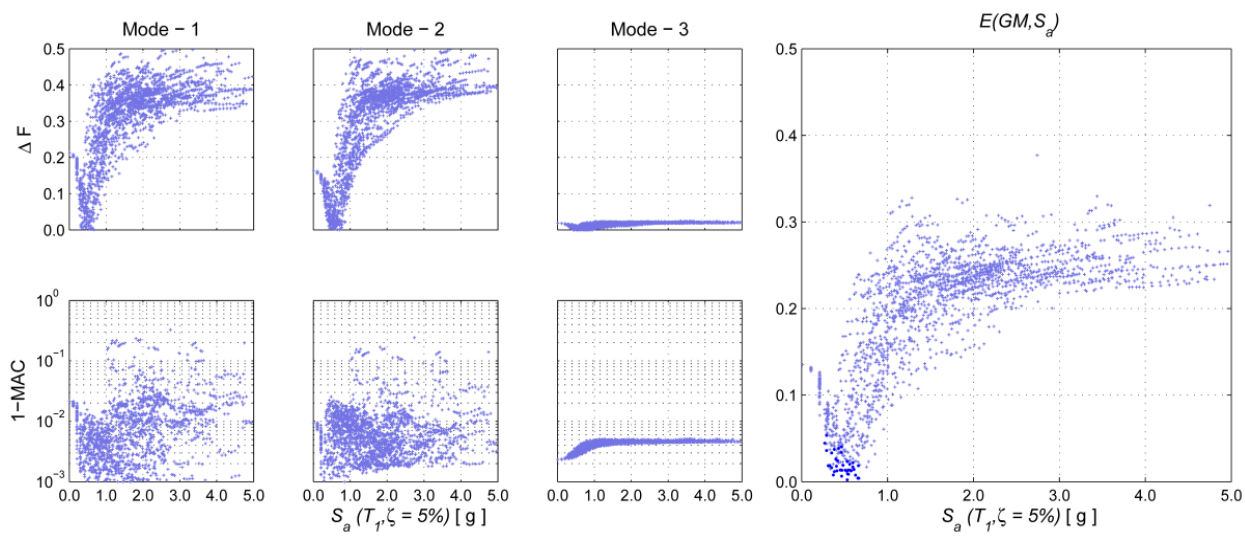

Figure 5–26 Error between analytical and modal properties

Table 5-8 Best ground motion-intensity pairs

W.N.2			W.N.3			W.N.4		
G.M. #	$S_a(T_1,\zeta_1)$	$E(GM,S_a)$	G.M. #	$S_a(T_1,\zeta_1)$	$E(GM,S_a)$	G.M. #	$S_a(T_1,\zeta_1)$	$E(GM,S_a)$
1	0.450	0.020	1	2.195	0.029	1	2.069	0.097
2	0.369	0.014	2	2.607	0.021	2	2.741	0.051
3	0.471	0.010	3	2.035	0.025	3	3.344	0.091
4	0.666	0.010	4	3.777	0.022	4	3.469	0.035
5	0.466	0.013	5	2.351	0.027	5	1.995	0.071
6	0.521	0.007	6	3.149	0.019	6	3.918	0.056
7	0.565	0.019	7	4.807	0.022	7	4.407	0.092
8	0.496	0.026	8	2.954	0.022	8	3.439	0.030
9	0.535	0.017	9	2.118	0.027	9	2.218	0.101
10	0.368	0.011	10	0.951	0.031	10	1.250	0.063
11	0.655	0.011	11	3.348	0.018	11	3.261	0.066
12	0.530	0.029	12	4.791	0.020	12	3.308	0.054
13	0.510	0.026	13	1.537	0.028	13	2.145	0.094
14	0.291	0.026	14	0.883	0.013	14	1.491	0.053
15	0.318	0.016	15	1.577	0.022	15	1.707	0.099
16	0.327	0.025	16	0.688	0.042	16	0.813	0.155
17	0.452	0.020	17	2.133	0.024	17	1.375	0.088
18	0.269	0.035	18	1.645	0.022	18	1.034	0.061
19	0.430	0.029	19	2.213	0.021	19	2.363	0.081
20	0.482	0.010	20	0.964	0.042	20	1.289	0.021
21	0.379	0.028	21	1.250	0.028	21	1.150	0.067
22	0.477	0.014	22	1.787	0.032	22	1.986	0.051
23	0.403	0.027	23	2.525	0.022	23	2.119	0.089
24	0.478	0.010	24	1.747	0.023	24	2.265	0.029
25	0.336	0.012	25	2.340	0.021	25	2.272	0.082
26	0.560	0.022	26	5.413	0.028	26	5.213	0.094
27	0.545	0.012	27	2.528	0.025	27	3.500	0.096
28	0.310	0.024	28	1.301	0.020	28	1.586	0.057
29	0.421	0.030	29	1.463	0.026	29	1.700	0.075
30	0.431	0.013	30	3.873	0.022	30	3.707	0.104
31	0.467	0.031	31	2.407	0.025	31	2.272	0.113
32	0.405	0.009	32	2.052	0.028	32	2.151	0.070
33	0.505	0.025	33	3.383	0.020	33	3.643	0.056
34	0.291	0.044	34	1.546	0.024	34	2.396	0.111
35	0.628	0.009	35	1.868	0.019	35	1.868	0.120
36	0.560	0.011	36	2.086	0.015	36	2.529	0.088
37	0.573	0.019	37	2.049	0.021	37	2.456	0.113
38	0.510	0.020	38	1.127	0.038	38	1.352	0.114
39	0.350	0.024	39	1.643	0.014	39	2.052	0.056
40	0.398	0.032	40	2.046	0.011	40	2.097	0.088
Median	0.466		Median	2.069		Median	2.185	

5.3.4 Step-4: Incremental Dynamic Analysis of the Damaged Bridge

In this step, collapse capacity of the damaged structure is estimated by performing IDA on the previously obtained FE realizations of the damaged bridge. First, a nonlinear response history analysis is performed on the intact model of the bridge using one of the five ground motion-intensity pairs selected in the previous step. The IDA is subsequently applied to the FE realization of the damaged bridge to estimate the collapse capacity of the damaged structure. Due to asymmetric distribution of damage throughout the structure, each ground motion is applied in positive and negative transverse directions of the bridge and the maximum absolute drift ratio of both analyses is taken as a point on the IDA curve corresponding to the ground motion under investigation. This procedure is repeated for each of ground motion-intensity pairs selected in step 3 of the procedure (figure 5–27 through figure 5–29 parts (a)-(e)). The collapse capacity of the bridge in the current damage state is subsequently calculated as the mean of the capacities estimated from different realizations of the damaged bridge (figure 5–27 through figure 5–29 part (f)). Estimated mean collapse capacities of the bridge ($\hat{S}_{a,cap.}$) at different stages of experiment and corresponding dispersion factors ($\beta_{cap.}$) are presented in table 5-9.

Table 5-9 Mean collapse capacity of the bridge

Test	W.N. 1	W.N. 2	W.N. 3	W.N. 4
$\hat{S}_{a,cap.}$ (g)	2.185	2.276	1.836	1.152
$\beta_{cap.}$	0.551	0.578	0.634	0.763
Loss of $\hat{S}_{a,cap.}$ (%)	0.00%	0.00%	15.97%	42.27%

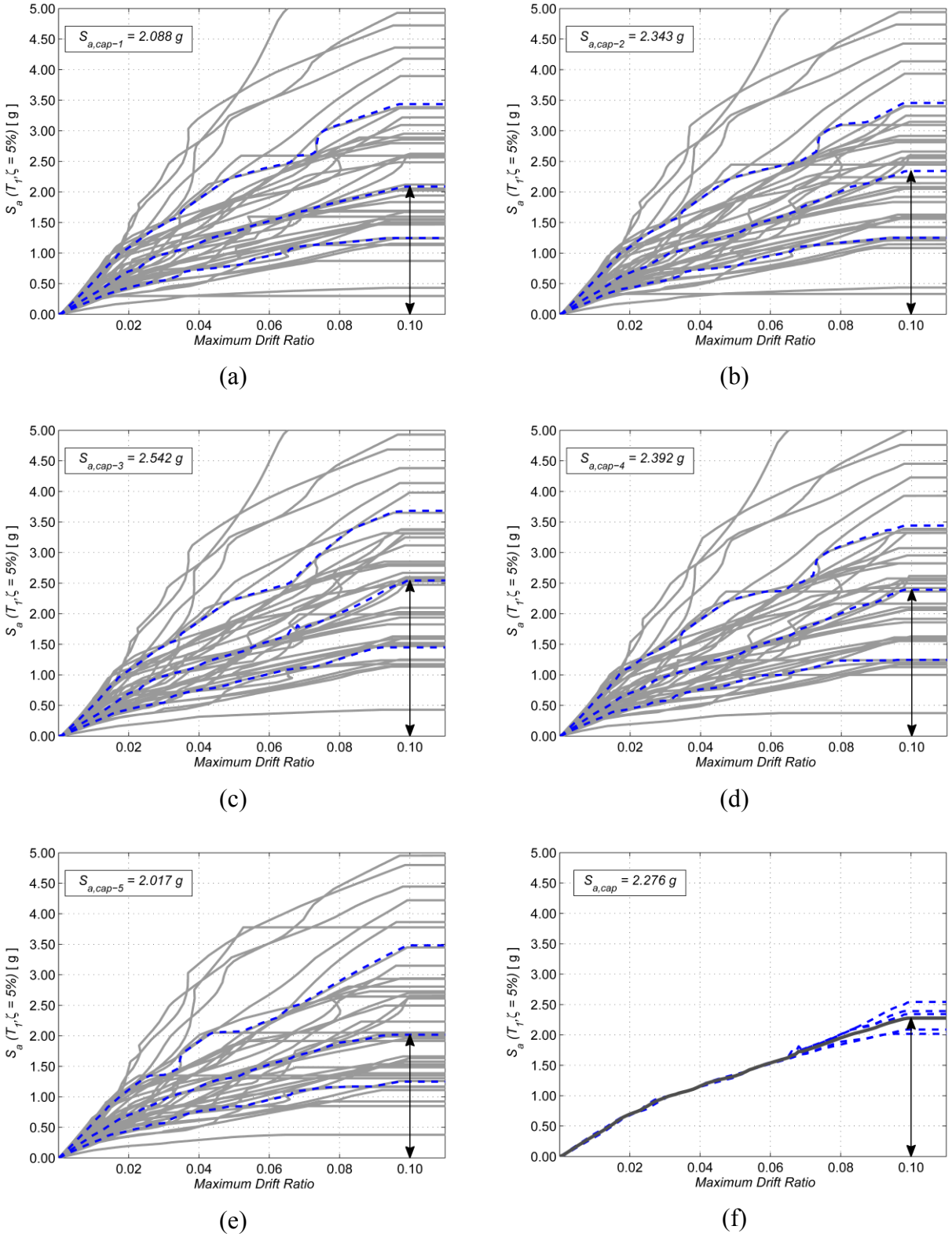

Figure 5–27 (a)-(e) IDA curves of damaged structure (f) Median IDA curves for all realizations of damaged structure (W.N.2)

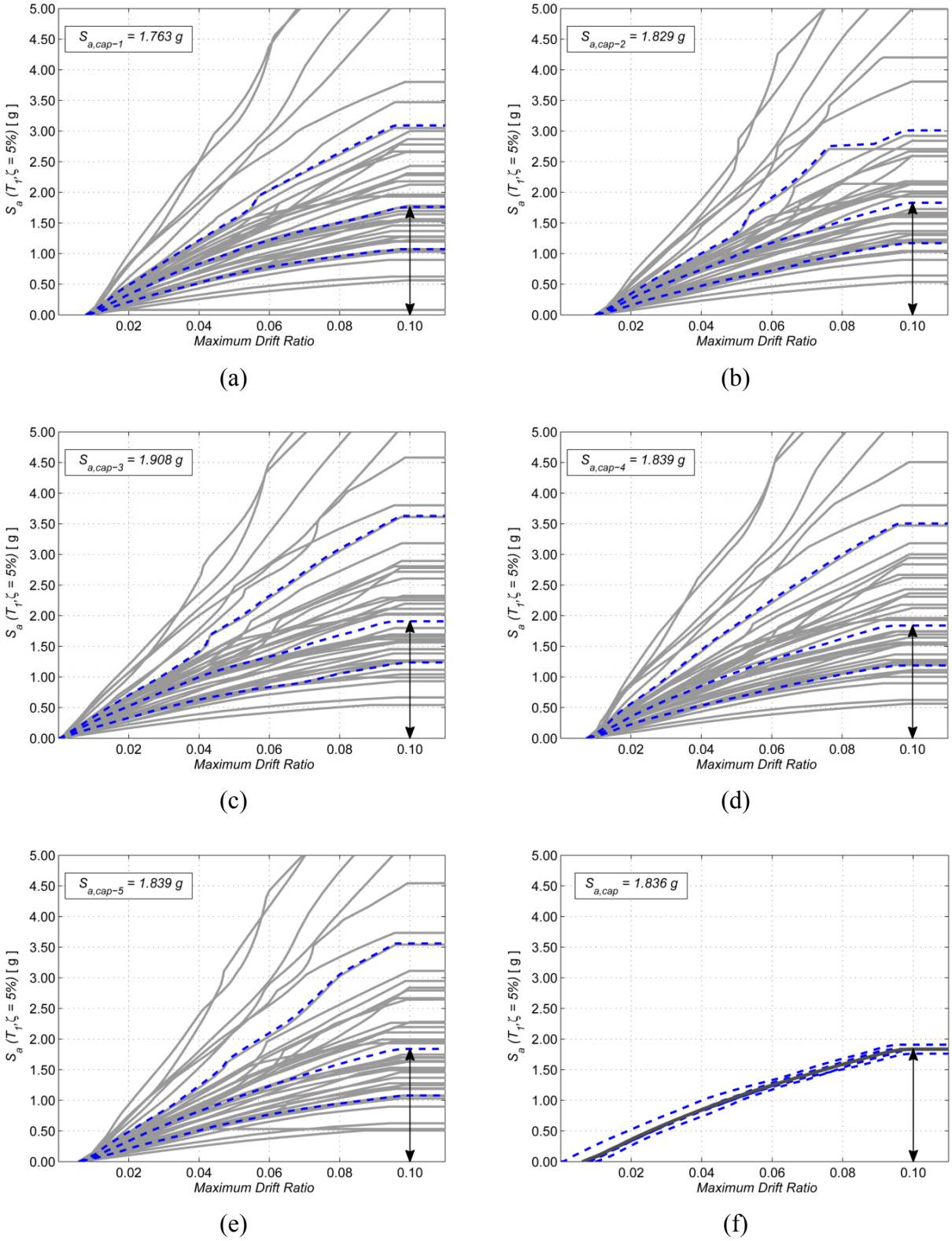

Figure 5–28 (a)-(e) IDA curves of damaged structure (f) Median IDA curves for all realizations of damaged structure (W.N.3)

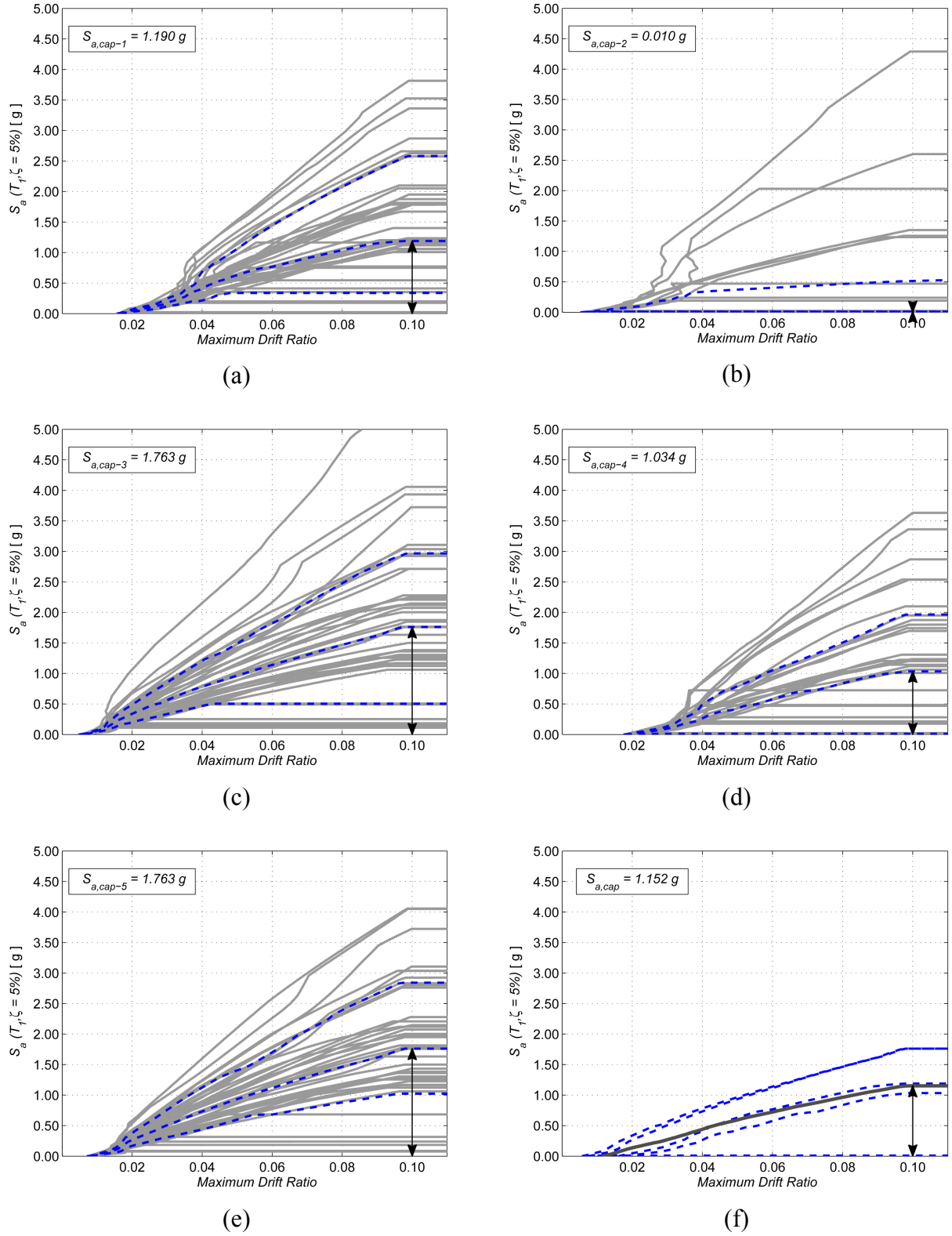

Figure 5–29 (a)-(e) IDA curves of damaged structure (f) Median IDA curves for all realizations of damaged structure (W.N.4)

With the progression of damage throughout the bridge, a generally decreasing trend is observable within the estimated collapse capacities. Slight increase in the estimated mean collapse capacity of the bridge from second white noise excitation (W.N. 2) can be correlated with the slight reduction in the median spectral acceleration at the first natural frequency of the damaged bridge in comparison to the intact bridge (figure 5–24 (a)) and the increased hysteretic damping properties of the bridge from early stages of the earthquake excitation due to minimal damages induced during tests 12~14. The same phenomena is also reported as the cause for hardening of IDA curves and structural resurrection[45].

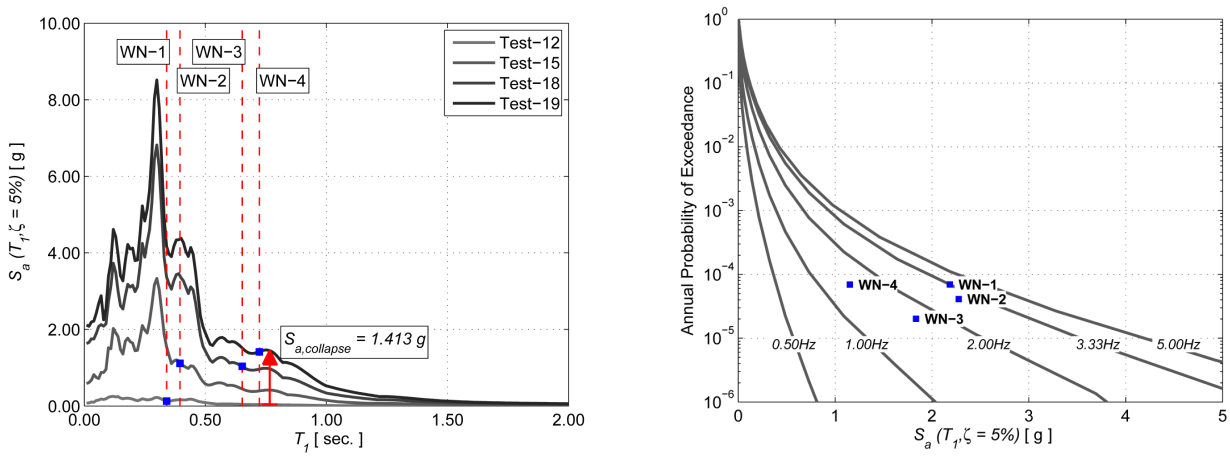

(a) (b)

Figure 5–30 (a) Spectral accelerations of the tests (b) Seismic Hazard Curves for the southern California Region

Figure 5–30(a) shows the response spectra of the input ground motions to the bridge during tests 12, 15, 17 and 18. The first natural periods of the bridge identified from the white noise excitations right before these tests are shown with vertical dashed lines. The intersections of the spectral curves with vertical lines represent the seismic demand on the bridge imposed by each earthquake excitation (shown by square markers). Based on estimated residual collapse capacity of the bridge from W.N. 4, at that stage of experiment high probability of collapse would have been predicted for the earthquakes with $S_a(T_1 = 1.383s, \zeta = 5\%) > 1.152g$. Obviously it is not

possible to verify the prediction procedure of such probabilistic phenomena with a single sample but at least the failure of the bridge during test-19 with $S_a(T_1 = 1.383s, \zeta = 5\%) = 1.413g$ could be interpreted as a sign of the efficacy of the proposed procedure.

5.3.5 Step-5: Functionality Status of the Damaged Bridge

A tagging criteria similar to the main shock-damaged building tagging criteria proposed by Yeo and Cornell[68] and applied by Bazzuro et al.[69] is utilized to classify or tag the bridge in into one of the functionality categories. The tagging criteria are defined based on the mean probability of exceedance of the collapse capacity ($\hat{S}_{a,cap.}$) of the bridge estimated in the fourth step of the procedure. Three functionality categories are defined as green, yellow and red-tagged categories. The placement of a bridge in a green-tagged category indicates that the bridge could safely be used by public without any necessary interruption in traffic flow. Yellow-tagged bridges are the one accessible for emergency personnel and for repair or retrofit purposes only. Finally, red-tagged bridges are the ones not deemed safe for any kind of access either by public or emergency personnel.

The functionality tag of bridge in each damage state is identified based on two parameters: (1) estimated values for the collapse capacities ($\hat{S}_{a,cap.}$) of the intact and damaged bridges (table 5-9) (2) bridge-site-specific mean annual frequency (MAF) of exceedance of the ground motion intensity level corresponding to the to collapse capacity ($\hat{S}_{a,cap.}$) of the bridge in intact (P_0) and damaged (P) states. Figure 5–30 (b) presents the seismic hazard curves for the southern California region where the bridge specimen under investigation is assumed to be located. The MAF of ground motions corresponding to the median collapse capacity of the bridge at different damages estimated from (W.N. 1~4) are shown with dark markers. The ordinate of the point

corresponding to the intact state of the bridge (W.N.1) indicates the value of (P_0) for the bridge specimen. The graphical interpretation of adopted tagging criteria is presented in figure 5–31. The figure has two scales for the ordinate: (1) the percentage of loss in collapse capacity of the bridge ($\hat{S}_{a,cap.}$) and (2) the (P/P_0) ratio that measures the increase in MAF of exceedance of collapse capacity of the bridge due to damage. The relationship between the two scales has been tuned for coastal California sites[69]; in general case, the relationship should be specified by bridge owners. The bridge-site-specific (P_0) is shown with a dashed vertical line. Using the amount of loss in collapse capacity of the bridge, listed in table 5-9, the functionality tags of the bridge at different stages of the experiment are specified.

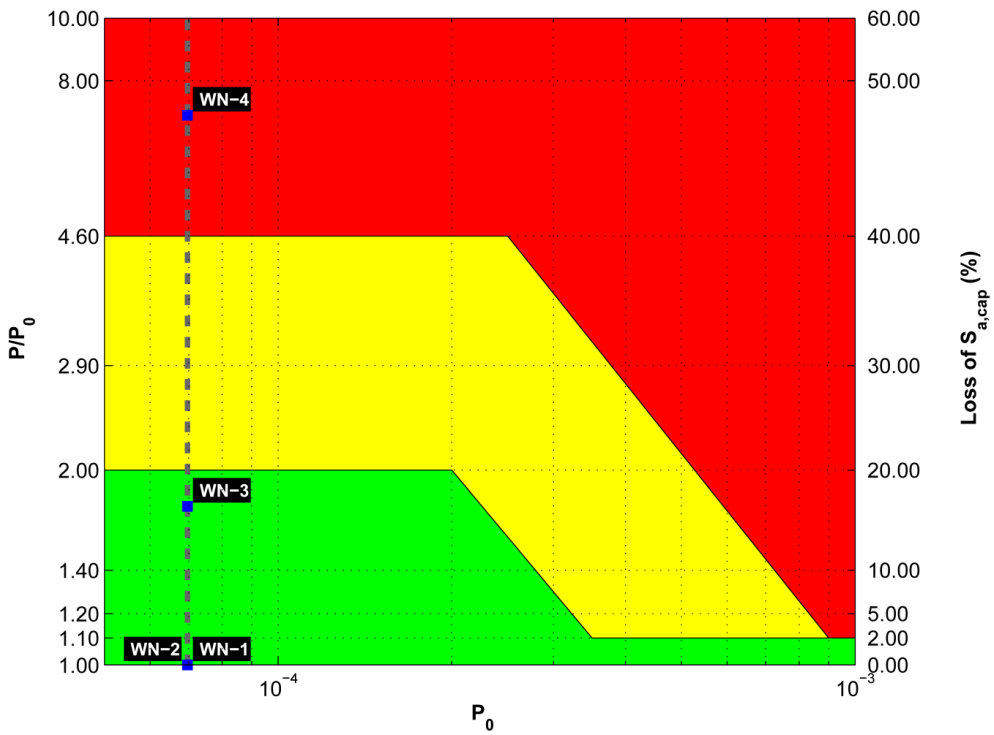

Figure 5–31 Tagging criteria and bridge status in different phases of experiment

5.3.6 Summary of the Methodology

The primary objective of the last part of this study was to develop a procedure based on vibration-based structural health monitoring data for estimation of residual collapse capacity of

damaged bridge to resist upcoming damaging events. A five-step procedure is proposed and applied for residual capacity estimation and functionality status update of bridge: (1) estimation of collapse capacity of the intact bridge. Incremental dynamic analysis (IDA) curves are used to estimate the median collapse capacity of the intact bridge. During IDA and after each nonlinear response history analysis post-earthquake analytical modal properties of the bridge are calculated and stored in a database to be used on the third step of the procedure. (2) Experimental modal analysis of the damaged bridge. Modal properties of the damaged bridge are extracted from either ending segment of the response to damaging earthquake or ambient vibrations of the bridge after the damaging event. (3) Generation of FE realizations of damaged bridge. Using the database generated during the first step of the procedure, earthquake ground motions and respective intensity levels that can drive the nonlinear FE model of the bridge to current damage status of the bridge are selected. These ground motion-intensity pairs are used to generate FE model realizations of the damaged bridge. (4) IDA of damaged bridge. Residual capacity of the damaged bridge is estimated by applying IDA to FE realizations of damaged bridge. Amount of loss in collapse capacity of the bridge is calculated using the mean value of collapse capacities estimated from different realizations. (5) Functionality status of the damaged bridge is specified using seismic hazard properties at the bridge site and amount of loss in collapse capacity of the bridge.

CHAPTER 6

CONCLUSIONS

This project explores the usage of the strong motion data for automated, remote, real-time damage assessment of bridges immediatly after a destructive event. It focuses on the vibration-based damage assessment of bridges and prediction of the damage consequencies.

Eexperimental modal analysis techniques are utilized for identifying dynamic characteristics, including natural frequencies, damping ratios and mode shapes, of the structure from acceleration measurements during ambient or forced vibrations of the structure. The output-only frequency domain decomposition technique is applied for modal identification from response measurements during ambient vibrations of the bridge. For modal identification from nonlinear responses of the bridge to high amplitude earthquakes, a three-step procedure is proposed and applied. Time-frequency representations of the nonlinear responses of the bridge are used for identification of linear segments of these responses with stable structural modal characteristics. Identified stable segments are subsequently used for state space model order selection and modal identification of the bridge. Although changes in dynamic characteristics of the bridge (e.g. reduction in natural frequencies or increase in modal damping ratios) can be correlated with the

existence of damage within the bridge, they can merely provide direct information about the locations and extents of damage within the structure.

Furthermore, efforts are made to locate and quantify the damage through a FE model updating approach. The FE model updating problem is formulated as an optimization problem with the objective of minimizing the error between measured and FE model simulated dynamic properties of the bridge by adjusting the FE model parameters. Two objective functions are defined using time and modal domains data. A hybrid optimization technique based on Genetic Algorithm is utilized for the global and local search of the FE model parameter space for the best set of FE model parameters. The comparison of the updated model parameters with their baseline values are used for identification of damage locations and extents within the structure.

Finally, this project investigates the consequences of the structural damage in the future performance of the bridge. Two methods are proposed based on static pushover and incremental dynamic analyses for residual capacity estimation in element and system levels respectively. The pushover-based approach takes advantage of double-integration and baseline-shift-filtering procedure to estimate the maximum drift ratios experienced by lateral force resisting elements during the earthquake excitation from acceleration measurements. The estimated ratios along with the pushover curves of the lateral force resisting elements are utilized to find the ductility and residual capacity of the elements. In the second approach, collapse capacities of the intact and damaged bridges are estimated using incremental dynamic analyses curves. A novel approach is proposed for generation of FE realizations of the damaged bridge using post-earthquake modal properties database created during the IDA of the intact bridge. Tagging

criteria are utilized to update the functionality status of the damaged bridge based on amount of loss in bridge collapse capacity and characteristics of the seismic hazard at the bridge site. Presented structural health monitoring and damage assessment methods and procedures have been applied to experimental data from a large-scale shake table experiment. Conclusions from each part of this study are presented in the following subsections:

6.1 Experimental Modal Analysis

- The comparison of modal data identified from the responses to white noise and earthquake excitations indicates that higher natural frequencies and lower modal damping ratios are identified from the responses to white noise excitations especially in lower damage levels where higher discrepancy was observed. This could be correlated with the level of response amplitude during each type of motion. Closure of the cracks during low amplitude white noise excitations contributes to the higher stiffness of reinforced concrete elements and increased modal frequencies. It also causes reduction in structural damping properties because of lower amount of energy dissipated through friction and slippage within the closed cracks. The high MAC values between the mode shapes identified from two types of motions indicate that these properties are less sensitive to the level of structural response amplitude and unless the proximity of the vibration mode frequencies make modal estimations biased, reliable and consistent mode shapes could be identified from both types of motions.
- It is a well known fact that modal properties of a structure are affected by damage throughout the structure but it is also important to consider the fact that not all modes are affected the same. As an example, for the case of bridge specimen under investigation, according to visual inspections, strain monitoring and analytical damage assessment

results, seismic damage was concentrated within the bents of the bridge and almost no damage was reported on the superstructure. Considering the variation of frequencies of different modes of vibration during the whole experiment, substantial reduction (more than 50%) was observed for the natural frequencies of the first two modes of vibration of the bridge while the variation in the third mode frequency was comparatively insignificant (less than 10%). Being lateral translational and torsional modes, characteristics of first two modes of vibration of the bridge are highly affected by the lateral force resisting elements (bents) properties. As a result, damage within these elements is expected to have significant impact on the properties of these two modes. On the other side, the third mode of vibration is the in-plane bending of the superstructure of the bridge the properties of which did not change significantly due to minimal damage to superstructure of the bridge. The same reasoning could be used to explain the increasing trend in identified damping ratios of the first two modes of vibration and almost invariant values for the third mode of vibration of the bridge.

- Comparison of the performances of state-space model identification techniques for time-frequency analysis indicates that prediction-error method generally produced slightly better fit between simulated and measured responses; however time-dependent modal properties identified using these two methods are shown to be in good agreement with each other. Considering relatively high number identification runs needed for time-frequency analysis of the response and significantly higher computational efficiency of subspace-based methods in comparison to iterative prediction error method, subspace method is recommended for time-frequency analysis of nonlinear responses of the structures to high amplitude earthquake excitations. Meanwhile, prediction-error method

is proposed for modal identification from stable ending segments of the nonlinear response due to better fit produced by the method.

6.2 FE Model Updating

- As stated earlier, two objective functions defined using time and modal domains data are utilized for damage assessment through FE model updating. Identified FE model parameters using either of the objective functions are compared with visual inspection results and experimental damage indices. The damage assessment results for the superstructure of the bridge show slight variations in the stiffness of the superstructure of the bridge (Less than 20% over the whole experiment). Obtained results are in complete accordance with the visual inspections of the superstructure of the bridge which indicated almost no damage at the final stage of the experiment. For verification of the identified stiffness correction factors for the bents of the bridge, measured displacement data are used for generation of acceleration-drift relationships for each bent of the bridge specimen. It is shown that the variations in identified stiffness correction factors of the bents completely coincide with the variation of experimental stiffness indices of the bents over a wide range of seismic damage within the bridge.
- One of the key points in definition of composite objective functions is the method of summarizing different errors into a single objective value. Weight assignment strategy is pretty common in such cases. Considering the fact that weighting factors can change the geometry of the objective function, location of the minimum point(s) and values of optimal parameters, extra care should be given to the calculation of the weighting factors. In this study, an adaptive approach is proposed for calculation of the weighting factors from structural response characteristics. The relative importance of the error in properties

of each mode of vibration is assigned based the average contribution of the mode in total response of the structure. The consistency of the identified model parameters using both objective functions indicates the efficacy of the proposed approach in weight assignment.

6.3 Residual Capacity Estimation

- In the pushover-based residual capacity estimation technique, comparison of the drift ratios calculated from displacement measurements with the values estimated by implemented double-integration and base-line trend removal procedure reveals promising results. The average relative error of 5.51% between measured and calculated maximum drift ratios during earthquake excitations indicates that the implemented technique can reliably be used for accurate estimation of structural drift ratios from acceleration measurements.
- Although the pushover-based residual capacity estimation procedure can produce valuable information about the damage condition of the lateral force resisting elements through a simple and user-friendly procedure, it has few drawbacks:
    1. Element-level assessment of a structural system may fail to take several system-level aspects of the structural behavior into consideration: (e.g. interactions between resisting elements, redistribution of internal forces and moments etc.)
    2. Dynamic characteristics of the damaged structure are not incorporated into the residual capacity estimation procedure. Increased energy dissipation properties due to hysteresis loops of damaged elements, variation in seismic demand on the bridge as a result of change in natural frequency of the damaged structure.
    3. Ignoring the likelihood of occurrence of earthquakes that may induce local or global collapse within the damaged bridge.

- The IDA-based procedure for residual collapse capacity estimation procedure takes advantage of experimental modal properties of the damaged bridge to generate FE realizations of the bridge in the current damage state. The residual collapse capacity of the damaged bridge is estimated by applying IDA to generated FE realizations of damaged bridge. Amount of loss in collapse capacity of the bridge along with seismic hazard characteristics at the bridge site are utilized to update the functionality status of the bridge.
- Results of the IDA-based residual collapse capacity estimation method highlight the fact that dynamic characteristics of the damaged bridge play a major role in the residual capacity of the bridge. In application of the methodology to the bridge specimen it was observed that estimated residual capacity of the bridge somewhat increased after first three earthquake excitations which introduced slight damage to the bridge structure. Increased energy dissipation properties, lower median spectral acceleration at the first mode frequency of the damaged structure in comparison to the intact bridge contributed to the higher median collapse capacity of the bridge.

In conclusion, the project has proposed, investigated, and experimentally validated methods for post-event damage assessment of seismically instrumented bridges using its vibration measurement data. The performance of these methods for the real world bridges with challenges such as higher modeling uncertainties, unknown environmental conditions, incomplete and noisy measurements is yet to be evaluated.

CHAPTER 7

REFERENCES

1. Rytter, A., *Vibrational based inspection of civil engineering structures = (Vibrationsbaseret inspektion af bærende konstruktioner)*, 1993, Department of Building Technology and Structural Engineering, University of Aalborg ; Rambøll, Hannemann & Højlund A/S: Aalborg; Nørresundby.
2. Farrar, C.R., R. Gallegos, and L. Los Alamos National, *Dynamic characterization and damage detection in the I-40 bridge over the Rio Grande*1994, Los Alamos, N.M.: Los Alamos National Laboratory.
3. Ghanem, R. and M. Shinozuka, *Structural-System Identification .1. Theory.* Journal of Engineering Mechanics-Asce, 1995. **121**(2): p. 255-264.
4. Shinozuka, M. and R. Ghanem, *Structural System-Identification .2. Experimental-Verification.* Journal of Engineering Mechanics-Asce, 1995. **121**(2): p. 265-273.
5. Farrar, C.R. and G.H. James, *System identification from ambient vibration measurements on a bridge.* Journal of Sound and Vibration, 1997. **205**(1): p. 1-18.
6. Loh, C.H. and Z.K. Lee, *Seismic monitoring of a bridge: Assessing dynamic characteristics from both weak and strong ground excitations.* Earthquake Engineering & Structural Dynamics, 1997. **26**(2): p. 269-288.
7. Feng, M.Q., J.M. Kim, and H. Xue, *Identification of a dynamic system using ambient vibration measurements.* Journal of Applied Mechanics-Transactions of the Asme, 1998. **65**(4): p. 1010-1021.
8. Lus, H., R. Betti, and R.W. Longman, *Identification of linear structural systems using earthquake-induced vibration data.* Earthquake Engineering & Structural Dynamics, 1999. **28**(11): p. 1449-1467.
9. Smyth, A.W., J.S. Pei, and S.F. Masri, *System identification of the Vincent Thomas suspension bridge using earthquake records.* Earthquake Engineering & Structural Dynamics, 2003. **32**(3): p. 339-367.
10. Weng, J.H., et al., *Output-only modal identification of a cable-stayed bridge using wireless monitoring systems.* Engineering Structures, 2008. **30**(7): p. 1820-1830.
11. He, X., et al., *System Identification of Alfred Zampa Memorial Bridge Using Dynamic Field Test Data.* Journal of Structural Engineering, 2009. **135**(1): p. 54-66.

12. Ewins, D.J., *Modal testing : theory, practice, and application*. Mechanical engineering research studies, 102000, Baldock, Hertfordshire, England; Philadelphia, PA: Research Studies Press.
13. Maia, N.M.M. and J.M. Montalvão e Silva, *Theoretical and experimental modal analysis*1997, Taunton, Somerset, England; New York: Research Studies Press ; Wiley.
14. Dimitriadis, G., et al., *Identification and Model Updating of a Non-Stationary Vibrating System.* ASME Conference Proceedings, 2004. **2004**(4174X): p. 143-152.
15. Dalianis, S.A., et al., *Simulation and Identification of Nonstationary Systems Using Linear Time-Frequency Methods.* Journal of Vibration and Control, 1998. **4**(1): p. 75-91.
16. Owen, J.S., et al., *The application of auto-regressive time series modelling for the time-frequency analysis of civil engineering structures.* Engineering Structures, 2001. **23**(5): p. 521-536.
17. Neild and S., *A review of time-frequency methods for structural vibration analysis.* Engineering Structures, 2003. **25**(6): p. 713-728.
18. Neild, S.A., P.D. McFadden, and M.S. Williams, *Damage Assessment in Concrete Beams Using Non-Linear Analysis of Vibration Measurements.* Key Engineering Materials, 2003. **245-246**: p. 557-564.
19. Nagarajaiah, S. and Z.L. Li, *Time segmented least squares identification of base isolated buildings.* Soil Dynamics and Earthquake Engineering, 2004. **24**(8): p. 577-586.
20. Marchesiello, S. and L. Garibaldi, *A time domain approach for identifying nonlinear vibrating structures by subspace methods.* Mechanical Systems and Signal Processing, 2008. **22**(1): p. 81-101.
21. Marchesiello, S., et al., *Time-dependent identification of a bridge-like structure with crossing loads.* Mechanical Systems and Signal Processing, 2009. **23**(6): p. 2019-2028.
22. Poulimenos, A. and S. Fassois, *Parametric time-domain methods for non-stationary random vibration modelling and analysis — A critical survey and comparison☆.* Mechanical Systems and Signal Processing, 2006. **20**(4): p. 763-816.
23. Friswell, M.I. and J.E. Mottershead, *Finite element model updating in structural dynamics*1995, Dordrecht; Boston: Kluwer Academic Publishers.
24. Mottershead, J.E. and M.I. Friswell, *Model Updating in Structural Dynamics - a Survey.* Journal of Sound and Vibration, 1993. **167**(2): p. 347-375.
25. Holland, J.H., *Adaptation in natural and artificial systems : an introd. analysis with applications to biology, control, and artificial intelligence*1975, Ann Arbor: Univ. of Michigan Pr.
26. Friswell, M.I., J.E.T. Penny, and S.D. Garvey, *A combined genetic and eigensensitivity algorithm for the location of damage in structures.* Computers & Structures, 1998. **69**(5): p. 547-556.
27. Chou, J.H. and J. Ghaboussi, *Genetic algorithm in structural damage detection.* Computers & Structures, 2001. **79**(14): p. 1335-1353.
28. Hao, H. and Y. Xia, *Vibration-based damage detection of structures by genetic algorithm.* Journal of Computing in Civil Engineering, 2002. **16**(3): p. 222-229.
29. Koh, C.G., Y.F. Chen, and C.Y. Liaw, *A hybrid computational strategy for identification of structural parameters.* Computers & Structures, 2003. **81**(2): p. 107-117.
30. Au, F.T.K., et al., *Structural damage detection based on a micro-genetic algorithm using incomplete and noisy modal test data.* Journal of Sound and Vibration, 2003. **259**(5): p. 1081-1094.

31. Franco, G., R. Betti, and H. Lus, *Identification of structural systems using an evolutionary strategy.* Journal of Engineering Mechanics-Asce, 2004. **130**(10): p. 1125-1139.
32. Perera, R. and R. Torres, *Structural damage detection via modal data with genetic algorithms.* Journal of Structural Engineering-Asce, 2006. **132**(9): p. 1491-1501.
33. Doebling, S.W., et al., *Damage identification and health monitoring of structural and mechanical systems from changes in their vibration characteristics: A literature review*, in *Other Information: PBD: May 1996*1996. p. Medium: ED; Size: 132 p.
34. Sohn, H. and L. Los Alamos National, *A review of structural health monitoring literature : 1996-2001*2004, Los Alamos, N.M.: Los Alamos National Laboratory.
35. Carden, E.P. and P. Fanning, *Vibration based condition monitoring: A review.* Structural Health Monitoring, 2004. **3**(4): p. 355-377.
36. Building Seismic Safety, C., A. United States. Federal Emergency Management, and C. Applied Technology, *NEHRP guidelines for the seismic rehabilitation of buildings*1997, Washington, D.C.: Federal Emergency Management Agency.
37. American Society of Civil, E. and A. United States. Federal Emergency Management. *Prestandard and commentary for the seismic rehabilitation of buildings*. 2000; Available from: http://purl.access.gpo.gov/GPO/FDLP628.
38. Bracci, J.M., S.K. Kunnath, and A.M. Reinhorn, *Seismic Performance and Retrofit Evaluation of Reinforced Concrete Structures.* Journal of Structural Engineering, 1997. **123**(1): p. 3-10.
39. Krawinkler, H. and G.D.P.K. Seneviratna, *Pros and cons of a pushover analysis of seismic performance evaluation.* Engineering Structures, 1998. **20**(4-6): p. 452-464.
40. Kim, S. and E. D'Amore, *Push-over Analysis Procedure in Earthquake Engineering.* Earthquake Spectra, 1999. **15**(3): p. 417-434.
41. Bracci, J.M., S.K. Kunnath, and A.M. Reinhorn, *Seismic performance and retrofit evaluation of reinforced concrete structures.* Journal of Structural Engineering-Asce, 1997. **123**(1): p. 3-10.
42. Gupta, B. and S.K. Kunnath, *Adaptive Spectra-Based Pushover Procedure for Seismic Evaluation of Structures.* Earthquake Spectra, 2000. **16**(2): p. 367-392.
43. Chopra, A.K. and R.K. Goel, *A modal pushover analysis procedure for estimating seismic demands for buildings.* Earthquake Engineering & Structural Dynamics, 2002. **31**(3): p. 561-582.
44. Villaverde, R., *Methods to assess the seismic collapse capacity of building structures: State of the art.* Journal of Structural Engineering-Asce, 2007. **133**(1): p. 57-66.
45. Vamvatsikos, D. and C.A. Cornell, *Incremental dynamic analysis.* Earthquake Engineering & Structural Dynamics, 2002. **31**(3): p. 491-514.
46. Vamvatsikos, D. and C.A. Cornell, *Applied incremental dynamic analysis.* Earthquake Spectra, 2004. **20**(2): p. 523-553.
47. Ibarra, L.F. and H. Krawinkler. *Global Collapse of Deteriorating Mdof Systems*. in *13th World Conference on Earthquake Engineering* 2004. Vancouver, B.C., Canada.
48. Bazzurro, P., et al., *Advanced Seismic Assessment Guidelines*, 2006.
49. Luco, N., P. Bazzurro, and C.A. Cornell. *Dynamic versus static computation of residual capacity of a main-shock damaged building to withstand aftershock*. in *13th World Conference on Earthquake Engineering*. 2004. Vancouver, B.C., Canada.

50. Johnson, N.S., S. Saiidi, and D.H. Sanders, *Large-Scale Experimental and Analytical Seismic Studies of a Two-Span Reinforced Concrete Bridge System*, 2006, University of Nevada, Reno.
51. Brincker, R., L.M. Zhang, and P. Andersen, *Modal identification of output-only systems using frequency domain decomposition.* Smart Materials & Structures, 2001. **10**(3): p. 441-445.
52. Ljung, L., *Prediction error estimation methods.* Circuits Systems and Signal Processing, 2002. **21**(1): p. 11-21.
53. Ljung, L., *System identification : theory for the user / Lennart Ljung*1999, Upper Saddle River, NJ :: Prentice Hall PTR.
54. Verhaegen, M., *Identification of the Deterministic Part of Mimo State-Space Models Given in Innovations Form from Input-Output Data.* Automatica, 1994. **30**(1): p. 61-74.
55. Van der Auweraer, H. and B. Peeters, *Discriminating physical poles from mathematical poles in high order systems: use and automation of the stabilization diagram.* Proceedings of the 21st IEEE Instrumentation and Measurement Technology Conference (IEEE Cat. No.04CH37510), 2004: p. 2193-8 Vol.3|2649.
56. Shih, C.Y., et al., *Complex-Mode Indication Function and Its Applications to Spatial Domain Parameter-Estimation.* Mechanical Systems and Signal Processing, 1988. **2**(4): p. 367-377.
57. Nelles, O., *Nonlinear system identification*2001, Berlin; New York; Barcelona [etc.]: Springer.
58. Clough, R.W. and J. Penzien, *Dynamics of structures*1975, New York: McGraw-Hill.
59. Croker, M.D., *Determination of Displacement by Double Integration of Accelerometer Signals.* Journal of Sound and Vibration, 1984. **93**(4): p. 598-600.
60. Thong, Y.K., et al., *Numerical double integration of acceleration measurements in noise.* Measurement, 2004. **36**(1): p. 73-92.
61. Hjelmstad, K.D. and M.R. Banan, *Time-Domain Parameter Estimation Algorithm for Structures. I: Computational Aspects.* Journal of Engineering Mechanics, 1995. **121**(3): p. 424-434.
62. Moschas, F. and S. Stiros, *Measurement of the dynamic displacements and of the modal frequencies of a short-span pedestrian bridge using GPS and an accelerometer.* Engineering Structures, 2011. **33**(1): p. 10-17.
63. Coelho, B., P. Hölscher, and F. Barends, *Enhancement of double integration procedure through spectral subtraction.* Soil Dynamics and Earthquake Engineering, 2011. **31**(4): p. 716-722.
64. Meng, X., A.H. Dodson, and G.W. Roberts, *Detecting bridge dynamics with GPS and triaxial accelerometers.* Engineering Structures, 2007. **29**(11): p. 3178-3184.
65. Medina, R.A. and H. Krawinkler, *Evaluation of drift demands for the seismic performance assessment of frames.* Journal of Structural Engineering-Asce, 2005. **131**(7): p. 1003-1013.
66. FEMA, *Recommended seismic design criteria for new steel moment-frame buildings FEMA-350*2000, Washington, D.C.
67. Farrar, C.R., S.W. Doebling, and D.A. Nix, *Vibration-based structural damage identification.* Philosophical Transactions of the Royal Society of London Series a-Mathematical Physical and Engineering Sciences, 2001. **359**(1778): p. 131-149.

68. Yeo, G.L. and C.A. Cornell. *Building Tagging Criteria Based on AfterShock PSHA*. in *13 th World Conference on Earthquake Engineering*. 2004. Vancouver, B.C., Canada.
69. Bazzurro, P., et al. *Guildlines for Seismic Assessment of Damaged Buildings*. in *13 th World Conference on Earthquake Engineering*. 2004.